This thesis is presented for the degree of Doctor of Philosophy of The University of Western Australia

Sediment resuspension under nonlinear internal waves

William Connellan Edge
B.Sc. in Engineering; B.Sc. in Commerce
June 2022

Oceans Graduate School & Oceans Institute
Supervisors: Assoc. Prof. Nicole L. Jones (Coordinating)
Dr. Matthew D. Rayson
Prof. Gregory Ivey

Thesis Declaration

I, William Connellan Edge, certify that:

This thesis has been substantially accomplished during enrolment in the degree.

This thesis does not contain material which has been accepted for the award of any other degree or diploma in my name, in any university or other tertiary institution.

No part of this work will, in the future, be used in a submission in my name, for any other degree or diploma in any university or other tertiary institution without the prior approval of The University of Western Australia and where applicable, any partner institution responsible for the joint-award of this degree.
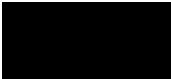
This thesis does not contain any material previously published or written by another person, except where due reference has been made in the text.

The work(s) are not in any way a violation or infringement of any copyright, trademark, patent, or other rights whatsoever of any person.

This thesis contains published work and/or work prepared for publication, some of which has been co-authored.

Signature: ████████

Date: 23/06/2022

Abstract

Nonlinear internal waves (NLIW) play a significant role in continental shelf ocean processes and, in particular, play an important role in sediment transport near the bottom boundary layer (BBL). Despite this importance, the exact mechanisms of sediment resuspension and transport under NLIW are still poorly understood, mainly due to a paucity of suitable field observations. The aims of this thesis were to: firstly, observe suspended sediment dynamics under NLIW forcing, secondly, to describe the mechanisms that drive resuspension and transport, and thirdly, to estimate the values of key and typically unobserved parameters that are essential inputs to robust models of sediment transport.

This research used oceanographic data sets collected at two different sites on the Australian Northwest Shelf. The 2017 experiment captured large-amplitude NLIW of depression shoaling along a mildly-sloped (1:1000) section of continental shelf. The 2019 experiment captured a diverse range of internal waves including: shoaling waves of depression, waves of elevation, solitary bores with trapped cores, and highly nonlinear "broken" waves on a moderately-sloped pelagic ridge (6:1000).

To overcome the challenge of observing near-bed suspended sediment concentration (SSC) at relatively deep ocean sites, we developed a formal and comprehensive calibration method. Calibration of the deployed instruments was essential to estimate the relevant contributions of different sediment fluxes and to perform quantitative comparisons with numerical modelling. The method linked different calibration models for several deployed instruments to a ground truth estimate of sediment concentration. We used Bayesian inference to estimate and propagate uncertainty generated from the calibration process. From this, we could estimate sediment concentration with precise estimates of uncertainty from all relevant instruments deployed on a bottom lander during both experiments.

We then applied this calibration methodology to NLIW events observed in the 2019 experiment data set. We estimated the key vertical sediment flux divergence terms, i.e., the key terms in the advection-diffusion equation governing sediment concentration. In addition, we were able to estimate the horizontal advection of the horizontal gradient of SSC at a single measurement location under these propagating NLIW. The sum of these fluxes agreed well with measured time-rate-of-change of sediment concentration, suggesting that the key terms were quantified. The high temporal resolution measurements allowed for a clear view of the different contributions to observed SSC even under high frequency short-lived events, such as internal bores. We applied this method to a large-amplitude NLIW of depression and a high frequency bore-like wave event with a trapped core. All terms were important under the wave of depression, while horizontal advection was the dominant term for the internal bore.

Finally, we developed a framework for the simultaneous estimation of multiple parameters using observations and a discrete advection-diffusion model. The aim of this framework was to take sparse observations of sediment concentration and use them to estimate typically unobserved parameters in a sediment model, such as the critical bed stress, settling velocity, and erosion rate. We employed a Bayesian parameter estimation technique using Markov Chain Monte Carlo sampling to quantify a probabilistic estimate for each parameter. We then applied this framework to three case studies. We demonstrated that the framework could be used to recover the posterior distribution for all sampled

parameters using sparse measurements of a tracer in an unsteady flow. Recovered posteriors were in good agreement with independent parameter estimates and prior expectations based on literature review.

Acknowledgments

Firstly, and most importantly, I would like to thank my supervisors for the opportunity to study with them over the past four years. Their tutelage and patience has ensured that the potentially painful experience of completing a PhD has instead been a welcoming and rewarding one.

I would like to thank several people at the University of Western Australia for their time, technical advice, or general counsel during my studies. Andrew Zulberti was generous with his time, skills, and technical knowledge that allowed for my research to progress much farther than it otherwise would. His knowledge of boundary-layer physics was exhibited by his succinct and uncomplicated explanations of complex processes that could be comprehended by anyone, even me. In addition I would like to thank Yankun Gong, Chris Whitwell, Connor Duffin, Edward Cripps, Madi Rosevear, and Paul Branson for their technical advice when I needed it most. Special thanks to Paul, who identified that the Masters degree I was enrolled in (at the time) was not necessary for enrolment in a PhD, thus beginning this journey.

I would also like to thank my friends and family for support during my studies. Thanks to Joanna Garcia-Webb for being an extremely flexible (and friendly) manager. Thanks in particular to my parents, who remained 4,000 km away, despite constant threats to move closer.

I would also like to extend my gratitude to Kath Lundy, Andrew Grime, Monica Mackman, and Phil Watson for supporting this research through the Oceans Graduate School (OGS) and the OFFshore Hub. Thanks also to Carlin Bowyer and Andrew Van de ven with the assistance using the University facilities. And special thanks to the Ocean Dynamics Group and all the other OGS students for providing an enlightening and entertaining research experience.

Finally, thanks to the regular 500 crew for the good times (Gong, Zulberti, usually Whitwell, but preferably Cami). In particular to my team mate Whitwell... you tried your best.

AUTHORSHIP DECLARATION: CO-AUTHORED PUBLICATIONS

This thesis contains work that has been published and prepared for publication.

Details of the work:

Edge, W. C., Jones, N. L., Rayson, M. D., & Ivey, G. N. (2021).
Calibrated suspended sediment observations beneath large amplitude non-linear internal waves. Journal of Geophysical Research: Oceans, 126, e2021JC017538.
https://doi.org/10.1029/2021JC017538

Location in thesis:

Chapter 2

Student contribution to work:

First author

Co-author signatures and dates:

23/06/2022   24/06/2022   24/06/2022

Student signature:

Date: 23/06/2022

I, Nicole Jones certify that the student statements regarding their contribution to each ▮▮▮▮▮▮d above are correct.
Coordinating supervisor signature:
Date: 23/06/2022

Contents

CONTENTS

List of Figures

List of Tables

Symbols

κ	von Kármán constant
ρ	density
$\Delta\rho$	excess density (sediment density minus water density)
Δ_z	vertical grid cell resolution
ϵ	residuals
γ_z	vertical turbulent diffusivity
θ	wave propagation direction (going towards, degrees clockwise from North) [Chapter 3]
θ	vector of model parameters including σ [Chapter 4]
θ_{mod}	vector of model parameters excluding σ [Chapter 4]
σ	standard deviation of the residuals (ϵ) for a model
τ_{bed}	bed shear stress [Pa]
τ_{cr}	critical bed stress required to initiate erosion [Pa], i.e., the bed strength to resist erosion
τ_{cr0}	the initial τ_{cr} when an erosion event first begins
τ_m	the slope of the increase of τ_{cr} as erosion proceeds
τ_b	the exponent of the increase of τ_{cr} as erosion proceeds
b	intercept [Chapter 2 and 3] or exponent [Chapter 4]
B_h	the BBL height (above the seabed)
C	suspended sediment mass concentration (also SSC)
C_{obs}	C from observations (as opposed to model outputs)
C_t	time-rate-of-change of C (equivalent to $\partial C/\partial t$)
C_v	volume concentration
C_x	horizontal gradient of C in the principal component direction of the horizontal currents
C_z	vertical gradient of C (in the direction of gravity)
C_d	drag coefficient
c_{wave}	wave speed
d_{50}	median particle diameter
D	deposition flux
E	erosion flux
$E1$	erosion model 1 [Chapter 4]

$E2$	erosion model 2 [Chapter 4]
L_{150}	Lander mooring deployed at the 150 m isobath
$\mathcal{L}$	log-likelihood
m	slope
m_c	total mass eroded per unit area
M	erosion rate parameter
$\mathcal{N}$	normal distribution
$p(a|b)$	the probability of a given b
$\widehat{R}$	potential scale reduction statistic
r^2	correlation coefficient
T_{150}	TWC deployed at 150 m isobath
t	time
t_1, t_2	analysis periods for the NLIW of depression in Chapter 3 (before and after 12:32)
U	horizontal current velocity in the principal component direction of the horizontal currents
U_{wave}	horizontal current velocity in the frame of a moving wave
u_*	friction velocity
W	vertical current velocity (aligned with gravity)
w	vertical current velocity [Chapter 4]
w_s	sediment particle settling velocity
z	vertical dimension, i.e., height above the bed

Acronyms

1Dv	one-dimensional vertical
ADCP	acoustic Doppler current profiler
ADE	advection-diffusion equation
ADV	acoustic Doppler velocimeter
ASB	above sea bed
BBL	bottom boundary layer
CTD	conductivity, temperature, and depth sensor
CI	credible interval
DE-MC	Differential Evolution MCMC
EI	echo intensity
KISSME	Kimberley internal soliton, sediments, and mixing experiment (2017 field experiment)
LISST	laser in-situ scattering and transmissometry
MCMC	Markov chain Monte Carlo
NLIW	nonlinear internal wave
NTU	nephelometric turbidity units (from an OBS instrument)
NWS	Northwest Shelf
OBS	optical backscatter
PDE	partial differential equation
PSD	particle size distribution
RANS	Reynolds-averaged Navier-Stokes
RBS	relative backscatter
RS	Rowley Shoals (2019 field experiment)
RV	research vessel
SSC	suspended sediment mass concentration (also C)
SP250	south mooring for KISSME at 250 m water depth
TC	tropical cyclone
TKE	turbulent kinetic energy
TWC	through-water-column (mooring)
T-string	thermistor string (deployed vertically)
UTC	Coordinated Universal Time

Chapter 1

Introduction

Nonlinear internal waves (herein NLIW) can induce near-bed currents strong enough to resuspend sediment particles from the bed up into the water column. Herein we define resuspension as the combined act of sediment erosion and transport vertically up into the water column. NLIW have been observed on most continental shelves most of the time [Jackson, 2007] but the mechanisms by which these waves resuspend sediment from the sea bed remain speculative [Boegman and Stastna, 2019]. Research to improve our understanding of NLIW-driven sediment resuspension is relevant to several applications, including ocean productivity, shelf geomorphology, and viability of offshore operations.

The resuspension and subsequent transport of sediment by NLIW is hypothesised to be a key component of the continental shelf biogeochemical cycle, bringing nutrient and carbon rich material into the euphotic zone [Sandstrom and Elliott, 1984]. Bogucki et al. [1997] added that NLIW may be important for pollutant redistribution in areas with contaminated sea floors. Since then, many studies have demonstrated the role of NLIW in the generation of intermediate nepheloid layers [Masunaga et al., 2017; Richards et al., 2013; Tian et al., 2019] and transportation of material offshore [Butman et al., 2006; McPhee-Shaw et al., 2004] and onshore [Cheriton et al., 2014; Moum et al., 2007]. Cacchione et al. [2002] demonstrated that over time internal wave processes may have the potential to govern the shape of continental slopes, with important considerations for long term shelf geomorphology. NLIW-induced sediment resuspension can also modify the sea floor sediment features, resulting in a range of bed formations [Ghassemi et al., 2022; Pomar et al., 2012; Reeder et al., 2011] that can modify bottom boundary layer dynamics, with implications for the dissipation of tidal and internal wave-induced currents [Egbert and Ray, 2000; Zahedi et al., 2021; Zulberti, 2021].

Resuspension is a key engineering question for industries working in shelf seas as it can halt offshore operations due to poor visibility [pers. comm Shell and Inpex]. Interaction with and development of the world's continental shelves has increased in recent decades due to the importance of submarine cables [Griffiths et al., 2019; Worzyk, 2009], expansion of the fossil fuel industry [Pinder, 2001], increasing feasibility of deep sea mining [Sharma, 2022], and development of offshore wind turbine technology [Tavner, 2021]. Unpredictable resuspension events lead to costly downtime on construction, maintenance, and inspection activities for projects in these areas [pers. comm Shell and Inpex]. NLIW resuspension can also lead to increased scour around structure footings [Xu et al., 2022], development of pipeline spans [Leckie et al., 2015], and asset burial [Leckie et al., 2016]. Improved understanding of these processes can lead to safer design, better predictions of maintenance requirements, and efficient

planning of operations. In addition, improved understanding of sediment resuspension and transport will inform environmental impact assessments for deep sea mining projects. Poor understanding of the dynamics of sediment disturbed from the sea floor is a key limitation for such projects [Fukushima et al., 2022].

Capturing detailed observations of resuspension by NLIW remains challenging. While NLIW are ubiquitous, predicting their exact amplitude, shape, and arrival time remains difficult. To assess the hydrodynamics of a NLIW in detail requires observations that span a range of temporal scales from the turbulent, to the tidal, which must be collected continuously over weeks or months in order to the increase the probability of capturing one or more large waves. To characterise the boundary layer dynamics and resolve the time-and-space-dependent resuspension dynamics, measurements of multiple parameters are required at several heights above the sea floor. Most instruments measure suspended sediment concentration (herein SSC) by proxy, so calibration is necessary for some types of analyses and for quantitative comparison to modelling results. Finally, to resolve turbulent (Reynolds) flux of suspended sediment, high frequency and co-located measurements are required of the vertical current velocity and SSC. Without all of this data research is often limited to empirical analysis.

To accommodate the challenges faced with interpreting (mostly single point) field observations, research into NLIW resuspension has also been performed using laboratory and numerical techniques [e.g., Aghsaee and Boegman, 2015; Aghsaee et al., 2012; Boegman and Ivey, 2009; Diamessis and Redekopp, 2006; Rayson et al., 2018]. Laboratory work allows for the modification of parameters and the repetition and comparison of results. The Reynolds number achievable in the laboratory are low, so caution must be applied when interpreting the results against field observations where momentum effects dominate over viscous effects [Zulberti, 2021]. However, field observations present a near-infinite arrangement of the important parameters that govern wave generation and dissipation, making the generalisation of such results difficult. Field-scale numerical models do not resolve the turbulent spatial and temporal scales necessary to reproduce the processes driving sediment transport at the seabed. 2D Reynolds-averaged models with parameterised turbulence can resolve large-scale features of wave shoaling and breaking and comparisons to resuspension observations have shown qualitative agreement [Bourgault et al., 2014; Masunaga et al., 2017], but are still missing important 3D effects [Aghsaee et al., 2012].

Previous field investigations of NLIW resuspension vary in their approach depending on the aim of the study and type of NLIW being studied. In this thesis we have focused on two general categories; resuspension by shoaling NLIW of depression, and resuspension by NLIW of elevation (with internal bore features). Early studies of NLIW of depression observed increased suspended sediment concentration (by proxy) coincident with low bed stress [Bogucki et al., 1997] or horizontal current reversals [Johnson et al., 2001]. The authors attributed resuspension to global instabilities or "shocks" in the lee of the wave due to an adverse pressure gradient. Soon after, numerical and laboratory studies demonstrated this process was possible at low Reynolds numbers [Boegman and Ivey, 2009; Diamessis and Redekopp, 2006]. Later studies made use of the development of the acoustic Doppler current profiler (ADCP) to examine the three-dimensional current structure above the bed. Quaresma et al. [2007] observed strong horizontal velocities near the bed and oscillations of the vertical current as a NLIW of depression passed the moorings, but no global instability was observed in the lee of the waves.

Zulberti et al. [2020] also observed a NLIW of depression propagating into the tidal current but did not observe any global instabilities and they hypothesised that energetic turbulence was able to destroy coherent structures before they could grow.

NLIW of elevation are the result of mode-1 or -2 waves moving into shallow water up the continental slope and may have some bore-like features. Henyey [1997] coined the term solibore to describe when wave-like and bore-like features were present together. Contrary to waves of depression, near-bed currents in waves of elevation are directed onshore and have been shown to transport fluid, energy, and material onshore [Cheriton et al., 2014; Jones et al., 2020; Moum et al., 2007]. In this case, a global instability may occur immediately ahead of the wave with the potential to resuspend sediment. Strong jets of positive vertical velocity have been repeatedly observed as these waves pass moorings [Bonnin et al., 2006; Hosegood et al., 2004; Masunaga et al., 2015; Richards et al., 2013]. Hosegood et al. [2004] and Bonnin et al. [2006] showed this type of event was correlated with high sediment trap results. Richards et al. [2013] and Masunaga et al. [2015] captured detailed observations of these solibores, which had a wave core with high acoustic echo intensity with strong positive vertical velocities on the leading side of the core and strong negative velocities observed on the trailing side of the core. Richards et al. [2013] showed that turbulence production and dissipation were elevated within the wave core, a likely mechanism for the maintenance of high SSC.

The two field experiments used in this work were conducted in areas with a high proportion of silt and clay-sized particles (i.e., mud), based on Smith McIntyre grab samples taken at each site. The cohesive forces between sediment particles were expected to be important to sediment dynamics at each site and thus there are some concepts worth introducing here. The strength of the cohesion between particles is a function of at least 15 different environmental factors [Nichols, 1986]. This can make parameters (that are trivial to reliably estimate for non-cohesive sediment) difficult to estimate based on the particle size distribution alone [e.g., Valipour et al., 2017, Figure 12]. Cohesive sediment particles are generally observed in some form of aggregate (floc). These can aggregate (flocculate) into larger flocs during times of lower turbulent kinetic energy and rapidly break back into smaller flocs when turbulence increases, changing the particle settling velocity. Finally, the bed strength of cohesive sediment (i.e., the critical shear stress required to initiate erosion) may vary by several orders of magnitude during a single erosion event. Weakly bonded particles at the surface may be lifted under weak currents, exposing particles with increasingly stronger bonds, complicating the estimation and modelling of mass flux through the sediment-water interface.

The quantification of uncertainty is an additional challenge that faces NLIW experiments and sediment transport studies in general. Oceanographic measurements are sparse, unsteady, and noisy, capturing the summation of processes occurring across a wide range of length and time scales. Suspended sediment observations are also sparse and noisy, and often only capture one particle population-averaged characteristic of a complex distribution of particles. The theoretical frameworks for boundary layer flows and empirical sediment resuspension models are inherently missing physics that leads to deviations between the models and observations. In this thesis we have made effort to include and quantify these sources of uncertainty, in particular the uncertainty that arises from calibration of instruments to SSC.

The focus of this thesis is the presentation of detailed observations showing both the hydrodynamic forcing and suspended sediment response under NLIW at two contrasting sites on the Northwest Shelf

of Australia. The first experiment (KISSME) was undertaken in 2017 at 250 m depth on a wide flat section of continental shelf. The second experiment (RS) was undertaken in 2019 at 150 m depth on a moderately sloped ridge. Using the extensive data set from each of these experiments, we sought to answer the following questions:

1. What is the nature of the temporal and vertical dynamics of SSC under observed NLIW?

2. What are the in-situ fluid-induced mechanisms that govern the observed temporal and vertical dynamics?

3. What can we quantitatively infer about unobserved processes of interest using the observations we have?

4. How much uncertainty is present in our observations, or derived from our analysis techniques, and how does this limit what we can confidently infer?

The work presented herein was preceded by and extends upon research by Zulberti [2021], who examined boundary layer momentum dynamics in the 2017 experiment data. As part of their work the acoustic current data from the ADCP and two ADV were processed and analysed, and many of the questions regarding the characterisation of the BBL and the turbulence properties are answered therein. This preceding work by Zulberti [2021] allowed for a much greater level of focus on sediment resuspension in this thesis.

This thesis contains three main chapters. Chapter 2 presents observations from the 2017 field experiment and describes in detail our approach to the problem of instrument SSC calibration. The calibration of instrument native units to estimates of SSC was a critical step towards the quantitative analyses presented in the later chapters. The calibration process was conducted with uncertainty quantification using Bayesian analysis techniques, and the resulting estimate of uncertainty was propagated through to further analyses, where appropriate.

Chapter 3 presents observations from the 2019 field experiment. Having already dealt with the calibration method in Chapter 2, this chapter proceeds to use current velocities and SSC estimates to calculate the key flux divergence terms in the advection-diffusion equation. This technique is applied to two contrasting NLIW events that propagated past the site: a large-amplitude NLIW of depression; and a Solibore. This allowed for a direct visualisation of the different contributions to observed SSC during each event. The results contrasted the inference drawn by previous studies, but we note that the site is unusual and different dynamics may be observed elsewhere.

Chapter 4 presents an inverse method to infer unobserved sediment model parameters from coupled forcing and response observations. This method employs Bayesian inference and related computational techniques to tackle the inverse problem, again with uncertainty quantification. A one-dimensional (vertical) model of the advection-diffusion equation is used to account for the time- and space-dependent nature of sediment resuspension under unsteady forcing. The method demonstrated that observations of near-bed current forcing and SSC response, both measured at some height away from the bed, could be used to infer erosion model parameters and sediment settling velocity simultaneously under a range of scenarios. This method was developed using barotropic and linear baroclinic tides, but was not extended for use under NLIW.

Chapter 5 summarises the contributions of the thesis and discusses the progress made. Recommendations for future work are also discussed.

Bibliography

P. Aghsaee and L. Boegman. Experimental investigation of sediment resuspension beneath internal solitary waves of depression. *Journal of Geophysical Research: Oceans*, 132(11):5473–5489, 2015. ISSN 21699275. doi: 10.1002/2015JC010768.Received.

P. Aghsaee, L. Boegman, P. J. Diamessis, and K. G. Lamb. Boundary-layer-separation-driven vortex shedding beneath internal solitary waves of depression. *Journal of Fluid Mechanics*, 690:321–344, 2012. ISSN 00221120. doi: 10.1017/jfm.2011.432.

L. Boegman and G. N. Ivey. Flow separation and resuspension beneath shoaling nonlinear internal waves. *Journal of Geophysical Research: Oceans*, 114(2):1–15, 2009. ISSN 21699291. doi: 10.1029/2007JC004411.

L. Boegman and M. Stastna. Sediment Resuspension and Transport by Internal Solitary Waves. *Annual Review of Fluid Mechanics*, 51(1):annurev–fluid–122316–045049, 2019. doi: 10.1146/annurev-fluid-122316-045049.

D. Bogucki, T. Dickey, and L. G. Redekopp. Sediment resuspension and mixing by resonantly generated internal solitary waves. *Journal of Physical Oceanography*, 27(7):1181–1196, 1997. doi: https://doi.org/10.1175/1520-0485(1997)027⟨1181:SRAMBR⟩2.0.CO;2.

J. Bonnin, H. Van Haren, P. Hosegood, and G. J. A. Brummer. Burst resuspension of seabed material at the foot of the continental slope in the Rockall Channel. *Marine Geology*, 226(3-4):167–184, 2006. doi: 10.1016/j.margeo.2005.11.006.

D. Bourgault, M. Morsilli, C. Richards, U. Neumeier, and D. E. Kelley. Sediment resuspension and nepheloid layers induced by long internal solitary waves shoaling orthogonally on uniform slopes. *Continental Shelf Research*, 72:21–33, 2014. ISSN 02784343. doi: 10.1016/j.csr.2013.10.019.

B. Butman, P. S. Alexander, A. Scotti, R. C. Beardsley, and S. P. Anderson. Large internal waves in Massachusetts Bay transport sediments offshore. *Continental Shelf Research*, 26(17-18):2029–2049, 2006. doi: 10.1016/j.csr.2006.07.022.

D. A. Cacchione, L. F. Pratson, A. S. Ogston, L. F. Pratson, and A. S. Ogston. The shaping of continental slope by internal tides. *Science*, 296(April):p. 724, 2002. doi: 10.1126/science.1069803.

O. M. Cheriton, E. E. McPhee-Shaw, W. J. Shaw, T. P. Stanton, J. G. Bellingham, and C. D. Storlazzi. Suspended particulate layers and internal waves over the southern Monterey Bay continental

shelf: An important control on shelf mud belts? *Journal of Geophysical Research: Oceans*, 119(1): 428–444, 2014. doi: 10.1002/2013JC009360.

P. J. Diamessis and L. G. Redekopp. Numerical Investigation of Solitary Internal Wave-Induced Global Instability in Shallow Water Benthic Boundary Layers. *Journal of Physical Oceanography*, 36(5): 784–812, 2006. ISSN 0022-3670. doi: 10.1175/JPO2900.1.

G. D. Egbert and R. D. Ray. Significant dissipation of tidal energy in the deep ocean inferred from satellite altimeter data. *Nature*, 405(6788):775–778, jun 2000. ISSN 0028-0836. doi: 10.1038/35015531.

T. Fukushima, A. Tsune, and H. Sugishima. *Comprehensive Understanding of Seafloor Disturbance and Environmental Impact Scenarios*, pages 313–337. Springer International Publishing, Cham, 2022. ISBN 978-3-030-87982-2. doi: 10.1007/978-3-030-87982-2_12.

A. Ghassemi, S. Zahedi, and L. Boegman. Bolus formation from fission of nonlinear internal waves over a mild slope. *Journal of Fluid Mechanics*, 932, 2022. ISSN 0022-1120. doi: 10.1017/jfm.2021.1033.

T. Griffiths, D. J. White, S. Draper, A. Leighton, L. Cheng, H. An, and A. Fogliani. Lateral resistance of "rigid" pipelines and cables on rocky seabeds. *Canadian Geotechnical Journal*, 56(6):823–839, 2019. ISSN 12086010. doi: 10.1139/cgj-2018-0208.

F. S. Henyey. Energetics of borelike internal waves. *Journal of Geophysical Research: Oceans*, 102(C2): 3323–3330, 1997. ISSN 01480227. doi: 10.1029/96JC03558.

P. Hosegood, J. Bonnin, and H. van Haren. Solibore-induced sediment resuspension in the Faeroe-Shetland channel. *Geophysical Research Letters*, 31(9):2–5, 2004. ISSN 00948276. doi: 10.1029/2004GL019544.

C. Jackson. Internal wave detection using the Moderate Resolution Imaging Spectroradiometer (MODIS). *Journal of Geophysical Research*, 112(C11):C11012, nov 2007. ISSN 0148-0227. doi: 10.1029/2007JC004220.

D. R. Johnson, A. Weidemann, and W. S. Pegau. Internal tidal bores and bottom nepheloid layers. *Continental Shelf Research*, 21(13-14):1473–1484, 2001. ISSN 02784343. doi: 10.1016/S0278-4343(00)00109-6.

N. L. Jones, G. N. Ivey, M. D. Rayson, and S. M. Kelly. Mixing Driven by Breaking Nonlinear Internal Waves. *Geophysical Research Letters*, 47(19), 2020. ISSN 19448007. doi: 10.1029/2020GL089591.

S. H. Leckie, S. Draper, D. J. White, L. Cheng, and A. Fogliani. Lifelong embedment and spanning of a pipeline on a mobile seabed. *Coastal Engineering*, 95:130–146, 2015. ISSN 03783839. doi: 10.1016/j.coastaleng.2014.10.003.

S. H. Leckie, H. Mohr, S. Draper, D. L. McLean, D. J. White, and L. Cheng. Sedimentation-induced burial of subsea pipelines: Observations from field data and laboratory experiments. *Coastal Engineering*, 114:137–158, 2016. ISSN 03783839. doi: 10.1016/j.coastaleng.2016.04.017.

E. Masunaga, H. Homma, H. Yamazaki, O. B. Fringer, T. Nagai, Y. Kitade, and A. Okayasu. Mixing and sediment resuspension associated with internal bores in a shallow bay. *Continental Shelf Research*, 110:85–99, 2015. ISSN 18736955. doi: 10.1016/j.csr.2015.09.022.

E. Masunaga, R. S. Arthur, O. B. Fringer, and H. Yamazaki. Sediment resuspension and the generation of intermediate nepheloid layers by shoaling internal bores. *Journal of Marine Systems*, 170:31–41, 2017. ISSN 09247963. doi: 10.1016/j.jmarsys.2017.01.017.

E. E. McPhee-Shaw, R. W. Sternberg, B. Mullenbach, and A. S. Ogston. Observations of intermediate nepheloid layers on the northern California continental margin. *Continental Shelf Research*, 24(6): 693–720, 2004. ISSN 02784343. doi: 10.1016/j.csr.2004.01.004.

J. N. Moum, J. M. Klymak, J. D. Nash, A. Perlin, and W. D. Smyth. Energy transport by nonlinear internal waves. *Journal of Physical Oceanography*, 37(7):1968–1988, 2007. ISSN 00223670. doi: 10.1175/JPO3094.1.

M. M. Nichols. Effects of fine sediment resuspension in estuaries. *Estuarine Cohesive Sediment Dynamics: Proceedings of a Workshop on Cohesive Sediment Dynamics with Special Reference to Physical Processes in Estuaries, Tampa, Florida, November 12–14, 1984*, pages 5–42, 1986. doi: 10.1007/978-1-4612-4936-8.

D. Pinder. Offshore oil and gas: Global resource knowledge and technological change. *Ocean and Coastal Management*, 44(9-10):579–600, 2001. ISSN 09645691. doi: 10.1016/S0964-5691(01)00070-9.

L. Pomar, M. Morsilli, P. Hallock, and B. Bádenas. Internal waves, an under-explored source of turbulence events in the sedimentary record. *Earth-Science Reviews*, 111(1-2):56–81, 2012. ISSN 00128252. doi: 10.1016/j.earscirev.2011.12.005.

L. S. Quaresma, V. J., Oliveira A., S. J., J. Vitorino, A. Oliveira, and J. da Silva. Evidence of sediment resuspension by nonlinear internal waves on the western Portuguese mid-shelf. *Marine Geology*, 246(2-4):21, 2007. ISSN 00253227. doi: 10.1016/j.margeo.2007.04.019.

M. D. Rayson, G. N. Ivey, N. L. Jones, and O. B. Fringer. Resolving high-frequency internal waves generated at an isolated coral atoll using an unstructured grid ocean model. *Ocean Modelling*, 122: 67–84, feb 2018. ISSN 1463-5003. doi: 10.1016/J.OCEMOD.2017.12.007.

D. B. Reeder, B. B. Ma, and Y. J. Yang. Very large subaqueous sand dunes on the upper continental slope in the South China Sea generated by episodic, shoaling deep-water internal solitary waves. *Marine Geology*, 279(1-4):12–18, 2011. ISSN 00253227. doi: 10.1016/j.margeo.2010.10.009.

C. Richards, D. Bourgault, P. S. Galbraith, A. Hay, and D. E. Kelley. Measurements of shoaling internal waves and turbulence in an estuary. *Journal of Geophysical Research: Oceans*, 118(1): 273–286, 2013. ISSN 21699291. doi: 10.1029/2012JC008154.

H. Sandstrom and J. A. Elliott. Internal Tide and Solitons on the Scotian Shelf: a Nutrient Pump At Work. *Journal of Geophysical Research*, 89(C4):6415–6426, 1984. ISSN 01480227. doi: 10.1029/JC089iC04p06415.

R. Sharma. *Approach Towards Deep-Sea Mining: Current Status and Future Prospects*, pages 13–51. Springer International Publishing, Cham, 2022. ISBN 978-3-030-87982-2. doi: 10.1007/978-3-030-87982-2_2.

P. Tavner. *Offshore Wind Power: Reliability, availability and maintenance: Reliability, availability and maintenance.* The Institution of Engineering and Technology, Stevenage, 2021. ISBN 1839533331.

Z. Tian, Y. Jia, S. Zhang, X. Zhang, Y. Li, and X. Guo. Bottom and Intermediate Nepheloid Layer Induced by Shoaling Internal Solitary Waves: Impacts of the Angle of the Wave Group Velocity Vector and Slope Gradients. *Journal of Geophysical Research: Oceans*, 124(8):5686–5699, 2019. ISSN 21699291. doi: 10.1029/2018JC014721.

R. Valipour, L. Boegman, D. Bouffard, and Y. R. Rao. Sediment resuspension mechanisms and their contributions to high-turbidity events in a large lake. *Limnology and Oceanography*, 62(3):1045–1065, 2017. ISSN 19395590. doi: 10.1002/lno.10485.

T. Worzyk. *Applications of Submarine Power Cables*, pages 1–8. Springer Berlin Heidelberg, Berlin, Heidelberg, 2009. ISBN 978-3-642-01270-9. doi: 10.1007/978-3-642-01270-9_1.

J. Xu, J. Xia, L. Wang, H. Zhu, and E. J. Avital. Direct numerical simulation on local scour around the cylinder induced by internal solitary waves propagating over a slope. *Ocean engineering*, 247, 2022. ISSN 0029-8018.

S. Zahedi, P. Aghsaee, and L. Boegman. Internal solitary wave bottom boundary layer dissipation. *Physical Review Fluids*, 6(7):1–16, 2021. ISSN 2469990X. doi: 10.1103/PhysRevFluids.6.074802.

A. Zulberti. *The turbulent bottom boundary-layer beneath nonlinear internal waves in the ocean.* PhD thesis, The University of Western Australia, 2021.

A. Zulberti, N. L. Jones, and G. N. Ivey. Observations of Enhanced Sediment Transport by Nonlinear Internal Waves. *Geophysical Research Letters*, 47(19):1–11, 2020. ISSN 19448007. doi: 10.1029/2020GL088499.

Chapter 2

Calibrated suspended sediment observations beneath large amplitude non-linear internal waves

ABSTRACT

While it has been recognized for some time that large amplitude non-linear internal waves (NLIW) can mobilise and transport sediment, quantitative observations of this process are rare. Rarer still are accompanying estimates of suspended sediment mass concentration (SSC) during the passage of NLIW. Here we present high resolution observations of NLIW and the SSC response within the bottom boundary layer. The observations were made in 250 m of water in a mildly sloping region of the Browse Basin on Australia's Northwest Shelf. We compare two independent but direct calibration methods, and employ Bayesian methods to estimate the uncertainty in SSC. During a large NLIW event, the peak mean SSC estimate at 0.49 m above the sea bed was 161 mg L^{-1}, with a maximum time-rate-of-change of 0.14 mg L^{-1} s^{-1}. The unsteady boundary layer forcing under NLIW resulted in a variable time-height dependent relationship between bed stress and SSC with increasing height above the sea bed. Suspended sediment was restricted to the bottom mixing layer, with sharp vertical gradients of up to 40 mg L^{-1} m^{-1} observed at the edge of the layer. The observations presented here are intended to offer guidance to numerical sediment modellers about likely SSC under strong NLIW.

2.1 Introduction

Sediment mobilisation and transport on continental slopes and shelves are under-observed phenomena that have important consequences for nutrient and pollutant redistribution [Green et al., 2019; Wang et al., 2007], cross-shelf particle fate [Butman et al., 2006], and sea bed infrastructure design, construction, and maintenance [Leckie et al., 2015, 2016]. While it has long been known that energetic internal waves exist throughout the world's oceans, only in the last 30 years have researchers begun to capture with sufficient temporal resolution the sporadic resuspension events driven by internal waves [e.g., Churchill et al., 1988; Gardner, 1989]. Recent observations and theory suggest that in the shelf

environment internal waves may be a key contributor to both instantaneous sediment resuspension [Bonnin et al., 2006; Masunaga et al., 2015] and to the long-term geomorphology [Cacchione et al., 2002; Zhang et al., 2021].

Tidally-generated internal waves transport energy throughout the ocean away from their source regions [Zaron, 2019]. Depending on the stratification, background shear, and internal wave amplitude, as they propagate these waves can steepen to form large amplitude non-linear internal waves (herein NLIW), examples of which have been observed at our site in around 250 m of water on the continental North West Shelf (NWS) of Australia (see Rayson et al. [2019] for more details). When the waves encounter shallower water they steepen and break, resulting in intensified currents and turbulence near the sea bed [Jones et al., 2020; Zulberti et al., 2020]. This process has been shown to resuspend and transport sediment [Cheriton et al., 2014; Hosegood et al., 2004; Noble and Xu, 2003; Valipour et al., 2017], and even lead to the creation of sediment layers fully detached from the near-bed region [McPhee-Shaw et al., 2004; Moum et al., 2002]. See the review by Boegman and Stastna [2019] for a thorough description.

Observations of mixing and sediment resuspension by NLIW have led to hypotheses on how this may influence chemical and biological processes in shelf seas, lakes, and estuaries [Cacchione and Drake, 1986; Klymak and Moum, 2003; Valipour et al., 2017]. Based on observed dissipation levels, Sandstrom and Elliott [1984] proposed that several internal waves per tidal cycle may be sufficient to mix sediment in suspension up from the near-bed region and into the surface euphotic zone, thus supplying sediment-based nutrients to this zone. Churchill et al. [1988] investigated the hypothesis that internal waves sorted shelf sediments by size and resulted in a fine sediment sink on the slope, although conclusive evidence for this process was not observed. Concern over the ability of fine sediments to redistribute pollutants from the bed into the water column and other areas of the ocean has also motivated studies [e.g., Bogucki et al., 1997; Gardner, 1989]. On the NWS in particular, the expansion of offshore infrastructure has also raised questions related to sea bed infrastructure stability under NLIW [Leckie et al., 2015, 2016].

Bourgault et al. [2014]; Cheriton et al. [2014]; Hosegood et al. [2004]; Masunaga et al. [2015] and others have observed bottom and intermediate depth sediment layers (nepheloid layers) that formed due to NLIW interacting with a sloped shelf. This process has been demonstrated in laboratory studies [e.g., Tian et al., 2019] and qualitatively replicated in a 2D transect field-scale numerical model [Masunaga et al., 2017]. The mechanisms for NLIW-induced sediment resuspension on flat bottoms and mild slopes remains speculative, with a recent review by Boegman and Stastna [2019] identifying the need for more process-oriented research in these areas. Near-bed global instability is thought to be a key mechanism where sediment is suspended through near-bed pressure fluctuations, not high bed shear stress [Diamessis and Redekopp, 2006]. This process has been replicated in laboratory and numerical studies [e.g., Aghsaee et al., 2012; Carr et al., 2008], however, recent observations from Zulberti et al. [2020] suggest that high levels of turbulence destroys potential coherent structures before they can develop into a global instability.

A detailed examination of the process of NLIW-induced sediment resuspension requires near-bed observations with high temporal and vertical resolution. In the bottom boundary layer (BBL) of shelf seas it is difficult to directly measure suspended sediment mass concentration (SSC) using filtered water

samples with high resolution (herein direct measurement of SSC refers to filtered water samples). To overcome this challenge, we collected indirect measurements from a range of instrumentation (acoustics, optical, and laser diffraction) that each measured some characteristic of sediment mass in suspension, with the expectation of proportionality to SSC. In general, a research challenge is to convert the indirect measurements supplied by a deployed instrument into estimates of SSC using direct measurements, i.e., calibration [e.g., Fugate and Friedrichs, 2002; Puig et al., 2001]. More often the practice has been to simply present the observations using the raw parameter, such as acoustic backscatter, for example. Although presentation of the raw data may avoid the addition of potential calibration model errors or biases, it can lead to a discrepancy or divergence between observations and modelling that, in turn, limits quantitative comparison and modelling of the dynamics. The indirect measurement and calibration techniques employed in this study are described in more detail in Section 2.2.

Calibration is challenging as it requires concurrent measurements (in both time and space) of both direct (true) SSC and the indirect estimate of SSC. In this study, we examined two popular calibration methods: *in-situ* field calibration achieved by vertical profiling a package with both an instrument and Niskin water bottles; and *laboratory* calibration occurring post-deployment using sediment collected from the sea floor. Both approaches introduce uncertainty, through the calibration model itself and through the limitations of the method employed.

Sediment resuspension is parameterized in sediment transport models, but uncertainty of the actual parameters should be quantified. Many of the parameters used to model sediment transport are better represented by probabilistic objects rather than deterministic single values. Adequate representation of the resulting cumulative uncertainty in sediment transport models is a key research challenge. Uncertainty can arise from physical variability, sampling strategy, measurement error, and model selection [Schmelter et al., 2011]. For this work we have employed Bayesian inference, a technique for statistical parameter estimation that computes the posterior distribution of the model parameters that is then used to quantify uncertainty [Gelman et al., 2013].

Calibration of indirect measurements of SSC with an estimate of uncertainty is a key first step towards understanding sediment transport and creating reliable models. In addition, the techniques used here explicitly incorporate estimates of the noise levels of different instruments and sampling strategies. Data fitting approaches typically fail to meaningfully quantify uncertainty, with implications for subsequent analysis, such as when calculating an SSC gradient (in time or space) or the position of SSC isopleths (analogous to an isotherm). By using Bayesian inference to estimate calibration parameters as fully probabilistic objects, we will create a reliable framework to propagate uncertainty through models in order to accurately compute the probability distribution of a single quantity of interest.

2.1.1 Objectives and outline

The primary aim of this paper is to present high resolution observations of SSC within the bottom boundary layer under tidal and NLIW forcing and to use these results to demonstrate the fundamental time and space-dependence of SSC. We achieve this through the calibration approach: first, by presentation and evaluation of two calibration methods (*in-situ* and *laboratory*); second, by use of a coherent framework to connect our many indirect measurements of SSC with a relatively small sample

of direct measurements of SSC.

The methodology described herein is able to connect many indirect observations of SSC together by using each calibrated instrument, in turn, as the "truth" for a new calibration. These chained calibrations were achieved using concurrent measurements (in height and time) from instruments deployed on a bottom-lander mooring. This approach allows us to connect sparse (and difficult to obtain) direct measurements of SSC with relatively large indirect observational data sets. We use Bayesian methods to keep track of uncertainty.

We start with a brief review of the relevant concepts on indirect SSC measurement (Section 2.2) and summarise some key Bayesian concepts (Section 2.3). We then describe the field experiment (Section 2.4), and the calibration process (Section 2.5). High resolution observations of large amplitude NLIW and estimates of near-bed SSC with uncertainty are then presented and discussed (Section 2.6). Here we use multiple instruments to analyse the sediment dynamics under NLIW forcing and examine the connection to bed shear stress.

2.2 Measuring suspended sediment concentration

2.2.1 Optical backscatter

Optical backscatter instruments (OBS) function by projecting a beam of light into the water and measuring the amount of light reflected back to a sensor. The sensor effectively measures the total cross-sectional area of all particles within the measurement volume, which Fugate and Friedrichs [2002] show is proportional to the volume concentration and inversely proportional to the particle diameter. It has been well demonstrated that, at relatively low concentrations, when the particle size distribution (PSD) in suspension remains constant, a linear relation exists between the OBS output and SSC [Green and Boon, 1993].

In practice, the observed PSD in suspension is rarely constant and changes in time will thus influence the output. Ludwig and Hanes [1990] found that the OBS response increased by approximately one order of magnitude going from sand to mud, and Gibbs and Wolanski [1992] found that, when observing fine sediment, increasing mean flow speed increased OBS response by about a factor of two owing to dynamic floc breakup (and vice versa). Thus an OBS calibration may give poor estimates of SSC if the observed PSD varies in time.

2.2.2 Laser scattering

Laser scattering provides a measurement of PSD by recording the angular intensity of laser beam light as it is scattered by particles suspended within the beam path. The LISST 200-X (Sequoia Scientific, Inc.) is a laser scattering instrument designed to measure PSD in-situ at high temporal resolution (up to 1 Hz). The LISST supplies a volume concentration, Cv, over 36 particle size bins ranging from 1–500 µm.

The LISST is able to measure the particle size and concentration of both individual particles and sediment flocs in suspension, but it cannot distinguish between them because it characterizes each floc as a single particle [Mikkelsen et al., 2005]. A collection of fine cohesive particles that has aggregated into a floc will thus be seen as a single large particle with a volume many times greater than the sum

of its parts. Hence, observations of dynamic aggregation and breakup driven by varying background flow can exert significant influence over the measured volume concentration, Cv.

Mikkelsen and Pejrup [2001] show that, when observing flocs, SSC and Cv are approximately related by the effective density, $\Delta\rho$:

$$\rho_{floc} - \rho_{water} \approx \Delta\rho \approx \frac{SSC}{Cv}. \tag{2.1}$$

When both flocs and single particles are present, SSC/Cv is the weighted average of the single particle density and $\Delta\rho$, and thus Equation 2.1 is no longer valid. Thus, a linear relationship between SSC and Cv should perform well when $\Delta\rho$ is relatively constant, and poorly when it is not. Additional limitations exist for this type of instrument, as summarised by Fugate and Friedrichs [2002].

2.2.3   Acoustic backscatter

Acoustic instruments, such as acoustic Doppler velocimeters (ADV) and acoustic Doppler current profilers (ADCP), observe particles in suspension in a manner analogous to OBS instruments. Particles in the measurement volume scatter an acoustic signal emitted from the instrument, a portion of which is reflected back to a receiver. For a given particle, acoustic scattering is controlled by the particle form function and particle scattering cross-section, where the form function itself is a complex function primarily of particle size and density, but also other variables such as shape and elasticity [Thorne and Hurther, 2014].

There is a significant body of literature examining the use of acoustic signals for SSC estimation using the sonar equation [summarised by Thorne and Hurther, 2014; Venditti et al., 2016]. In general, the reverberation level measured by the instrument (herein Echo Intensity, EI) must be converted to backscatter before it is usable. This involves correction of the EI to account for two-way transmission loss by beam spreading and attenuation by water, transmit power, an instrument constant, a near field correction, and if necessary also sediment attenuation (see Deines [1999] for the original method, Gartner [2004] for the near-field correction, and Gostiaux and van Haren [2010] for a correction to the method).

In many cases the full correction to backscatter presented by Deines [1999] is unnecessary and only the relative backscatter (RBS) is required for an empirical calibration [Gartner, 2004]. In addition, when sediment concentration is relatively low (less than 0.1 g L^{-1}), and particle size is between 10-100 µm, attenuation due to sediment particles may be ignored [Ha et al., 2011]. When the particle population remains constant, the ensemble averaged form function is also constant, and an empirical relationship between backscatter strength and the base 10 logarithm of SSC can be found across a wide range of environmental conditions [e.g., Fugate and Friedrichs, 2002; Gartner, 2004; Ha et al., 2009; Kim and Voulgaris, 2003]. At relatively low concentrations this relationship is

$$log_{10}(SSC) = mRBS + b, \tag{2.2}$$

where again, RBS is the relative backscatter. The acoustic log_{10} decibel scale introduces complications for uncertainty estimation that are examined in the results section. The EI corrections outlined here are generally not necessary for the single point measurement ADV and therefore EI can be used directly

in place of RBS in Equation 2.2.

The assumption that the particle size distribution is constant, both in time and along the length of the acoustic beam, is a limitation of this method. As with the OBS and LISST instruments, changes to both the observed primary PSD and flocculation processes can influence an acoustic instrument's response. For example, MacDonald et al. [2013] showed through controlled laboratory experiments that the flocculation process significantly alters the acoustic scattering properties of cohesive sediment.

2.3 Bayesian inference

2.3.1 Bayes theorem

Bayesian inference is a statistical modelling approach that accommodates probabilistic objects and is well suited to environmental data analysis [e.g., Manderson et al., 2019; Schmelter et al., 2011]. It does this by drawing conclusions about model parameters given some set of observed data and prior knowledge of parameters, using Bayes' rule.

Measurement of a probabilistic process produces a set of observations, x and y; for example, OBS data and SSC from filtered water samples. The y data are conditioned on both x and the model parameters, represented by the vector θ. This is called the *likelihood function*, $p(y|x, \theta)$, which describes the probability of the y data having a particular value given θ and some observations x. In the Bayesian paradigm, θ is unknown and not fixed. The probability of θ, $p(\theta)$, is called the *prior* distribution and represents any initial knowledge about θ (and can be vague, non-informative, or include expert knowledge, for example). Bayes' theorem states that the *posterior* distribution, $p(\theta|x, y)$, depends upon both the prior distribution and the likelihood function [Gelman et al., 2013],

$$p(\theta|x, y) = \frac{p(\theta)p(y|x, \theta)}{p(y)},$$

(2.3)

where $p(y)$ is a normalising constant that is the sum over all possible values of θ.

Model uncertainty can be extracted from the posterior distribution, making it trivial to derive an unambiguous, quantitative definition of uncertainty - the credible intervals (CI). A common presentation of uncertainty is the 95% CI, e.g., intervals (a,b) that indicate $p(a < \theta < b|x, y) = 0.95$, or the 95% highest probability density of the posterior distribution [e.g., Manderson et al., 2019].

2.3.2 Linear calibration model

In the Bayesian paradigm, for the case of a two parameter linear model $y = mx + b$ (such as our OBS and SSC observations), θ contains all model parameters: the slope, m; the intercept, b; and the residual variance parameter, σ. The parameter σ represents the range of possible values the y residuals could be, given the distribution of possible slope and intercept values. The observed data are represented by the vector x (OBS) and the vector y (SSC), so the model takes the vector form,

$$y|m, b, \sigma, x \sim \mathcal{N}(mx + b, \sigma^2).$$

(2.4)
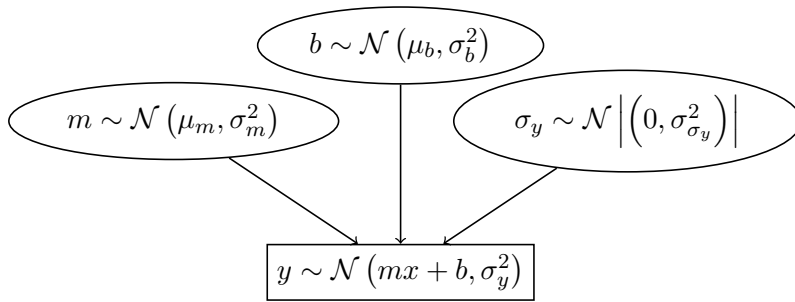
Figure 2.1: Directed acyclic graph of a single linear model. Prior distributions (shown as ellipses) inform the linear model (rectangle).

$\mathcal{N}()$ indicates a normal distribution with a mean and variance in the brackets, so that each SSC data point (y_i) is a distribution with a mean, $mx_i + b$, and a variance, σ^2. This form of the model assumes equal uncertainty for each y value, Gaussian white noise for the y residuals with a constant variance (homoscedasticity) and zero conditional correlations. More complex models are possible but were not considered here.

2.3.3 Model setup & computation

The Python probabilistic programming library *PyMC3* [Salvatier et al., 2016] was used to calculate the posterior distribution of the calibration model parameters using a Markov Chain Monte Carlo (MCMC) sampling algorithm. First, prior distributions must be specified for each model parameter, regardless of the computational method. *PyMC3* contains a significant library of distributions that make it trivial to specify priors.

For the linear model proposed, priors for m and b were simply specified as normal distributions, and σ was specified as half-normal (the distribution of σ represents the absolute value of model error and cannot be negative). Each prior was specified with large variance so as to be effectively non-informative, in which case the posterior distribution is "weighted" by the data. A directed acyclic figure graphically represents the model setup (Figure 2.1).

Our aim is to estimate the joint posterior distribution for the model parameters, $p(m, b, \sigma | x, y)$, through a sampling algorithm. Given a data set, MCMC sampling was used to calculate the posterior distribution for the slope, intercept, and σ^2. These individual posterior distributions combine to form the joint posterior distribution used to estimate total uncertainty. More information on the MCMC sampling algorithm can be found in Salvatier et al. [2016].

2.4 Site description

2.4.1 Field experiment

The near-bed sediment observations were collected as part of the 2017 Kimberley Internal Soliton, Sediment, and Mixing Experiment (KISSME 2017) [Rayson et al., 2019; Zulberti et al., 2020]. The experiment was undertaken from 1 April to 22 May 2017 on Australia's NWS in around 250 m of water. The experiment consisted of three through-water-column moorings and a bottom lander. The region is characterised by a 200 km wide continental shelf and a large tidal range. The measurement
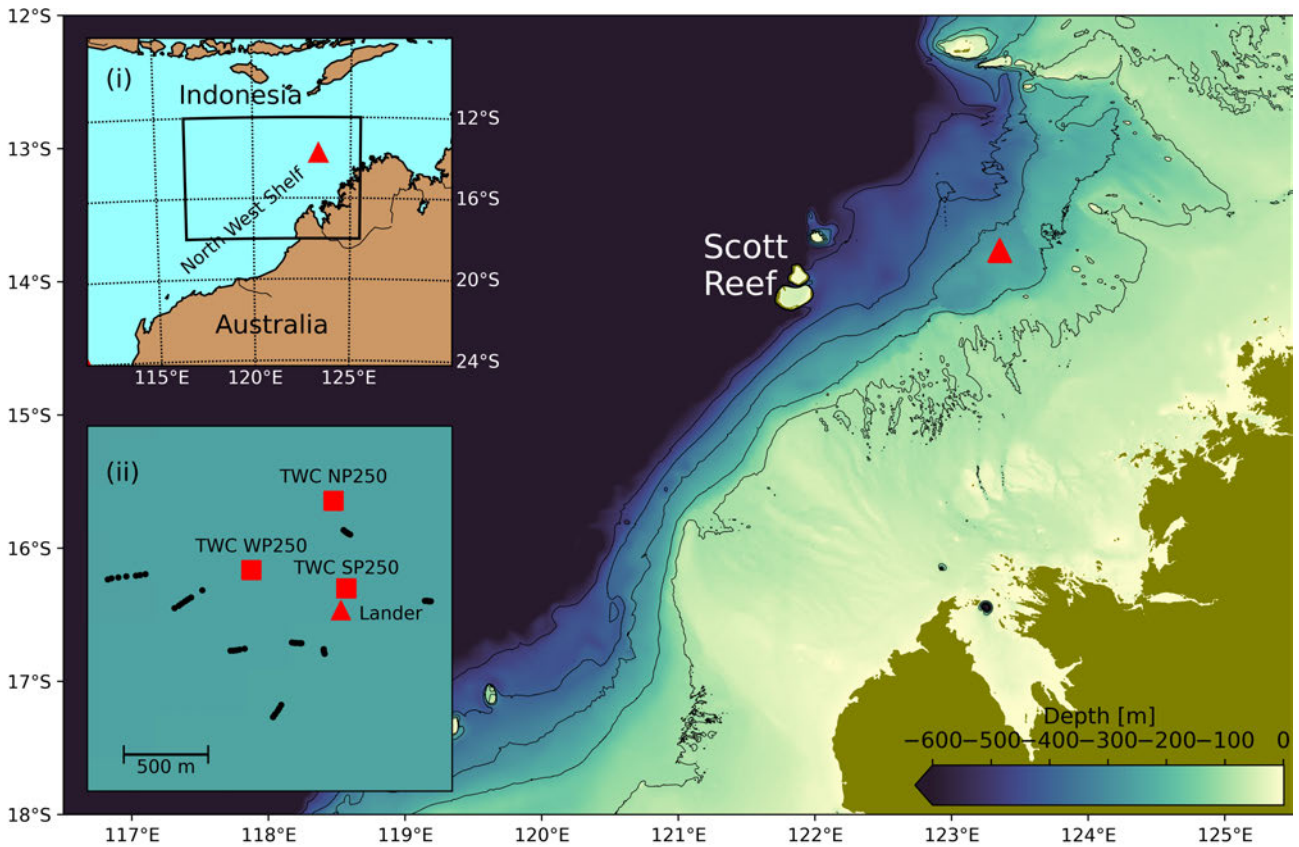
Figure 2.2: Location of the KISSME 2017 field campaign (red triangle) on the NWS of Australia.
Contours are at 100 m intervals. Inset (i) shows the regional location between mainland Australia and
the Indonesian archipelago to the north. Inset (ii) details of the mooring configuration, including the
through-water-column (TWC) moorings. The black dots show the location of all Niskin bottle samples
used for the in-situ calibration.

site was chosen for its relatively flat bathymetry, with an estimated cross-shelf slope of 0.2% for at
least 40 km in all directions (Figure 2.2). For this work we restrict our analysis to the 15 days from 2
to 16 April when all instruments had sufficient battery power and performed as expected.

The focus for this study was the data collected from the bottom-lander mooring (red triangle
in Figure 2.2), located approximately 100 m south of the nearest through-water-column mooring,
labelled TWC SP250. The lander was specifically designed to capture the BBL response to NLIW
forcing (Figure 2.3). The lander was equipped with two Nortek Vector ADV, an upward looking
Nortek Signature 1000 5-beam ADCP, a WET Labs OBS, and a Sequoia LISST 200-X (as per the
configuration in Figure 2.3). The two 6 MHz ADV were located at 0.49 and 1.41 m above sea bed
(ASB) and sampled at 64 Hz. The 1 MHz ADCP sampled over the depth range from 0.53 to 23.35 m
ASB at 0.2 m vertical resolution and at 8 Hz. The LISST was located at 0.87 m ASB and sampled
every 12 s, while the OBS was located at 1.14 m ASB and collected a three-sample burst every 90 s
(Table 2.1).

The three through-water-column moorings were deployed in a triangular arrangement about 500 m
apart (shown as red squares in Figure 2.2ii) to measure vertical and horizontal variability of internal
wave-affected ocean properties, as detailed in Rayson et al. [2019]. Through-water-column mooring

Table 2.1: KISSME 2017 instrument sampling programs

Instrument	Sampling frequency	Height (m ASB)
LISST	12 s	0.87
OBS	90 s	1.14
ADCP	8 Hz	0.53–23.33 (0.2 m spacing, 115 bins)
ADV	64 Hz	0.49 and 1.41
Thermistors	2 Hz	∼10 m spacing

SP250 captured temperature data at approximately 10 m vertical resolution from the sea bed to 230 m ASB, sampling at 2 Hz and averaged to 60 s, which was used to provide additional context to the lander observations.

In addition to the moorings, vertical profiles of physical properties of the water column were collected as close as possible to the lander mooring for two 12-hour periods using a CTD-Rosette. The two periods were chosen to represent spring and neap tide conditions. Profiles were undertaken at hourly intervals (currents permitting), but some profiles were obtained at distances of up to 1,400 m from the lander mooring because of strong currents and mooring interference concerns. Attached to the profiling frame were 12 Niskin bottles, a CTD, transmissometer, and a LISST 200-X that auto-logged to the ships computer. Bottle samples were collected during both profiling periods and vacuum-filtered on-board (location of samples shown as black dots in Figure 2.2ii inset). A bottom sediment sample was collected from the sea bed surface using a Smith McIntyre grab, which indicated a mean diameter of 21 μm. Further details regarding collection, processing, and PSD analysis are summarised separately (Appendix A).

The observation data from all instruments was processed by averaging over 5-minute blocks at 1-minute intervals (i.e., 5-minute boxcar-filtering centred on a 1-minute time step, giving an 80% overlap). This was done to reduce the influence of spatial variation between each instrument and to average over several of the longest turbulent fluctuations expected, whilst limiting the inclusion of internal wave fluctuations [Zulberti et al., 2020]. The acoustic calibration data was produced by taking every fifth point from the observation data, removing the overlap. The flagging process for each instrument, described next, was the same for both the observation and acoustic calibration data sets.

The LISST was processed using the manufacturer supplied software and instructions. Warning flags were included in the data set, but bad flags were not, and only blocks with at least 80% good data return were included for subsequent analysis. The LISST data was also used to identify periods of flocculation (described next).

Raw voltage data from the OBS was converted to units of NTU using the latest manufacturer calibration parameters and the median value from each burst was selected. Note that the conversion from voltage to NTU was not necessary for calibration and does not change the information contained in the data set (the measure of the reflective cross-section of all particles within the measurement volume). This was only done to enable comparison with other data presented in units NTU (shown in Figure 2.4). Data points where the instrument reached its upper limit were flagged and removed. Additional spikes from the OBS instrument that occurred towards the end of the deployment were visually removed, and only 5-minute blocks with at least two (out of three) data points were included.

Echo intensity (EI) from each ADV was left as counts for simplicity, under the assumption that
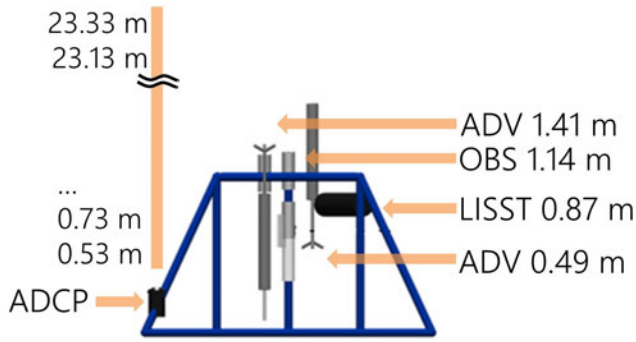
Figure 2.3: Schematic of the KISSME 2017 bottom lander setup showing the measurement volume height above the sea bed for each instrument. Note that the vertically-oriented fifth beam of the ADCP was used for backscatter (no slant angle).

changes in water and particle attenuation were insignificant for a point measurement. Only one beam from each ADV was used and no flags were applied. The final EI time series from each ADV was inspected visually and some suspect spikes from the upper ADV data set were flagged and removed.

The ADCP used for this study has a fifth beam that is oriented vertically away from the instrument with zero slant angle, which was used for backscatter analysis. ADCP EI was automatically converted to uncorrected backscatter (in dB) during processing with the manufacturer software. Uncorrected backscatter from beam 5 (vertical) was corrected to relative backscatter using the method described by Gartner [2004] (based on the method presented by Deines [1999]), including the near-field correction. This method adjusts the backscatter by accounting for variable two-way transmission losses as the acoustic signal travels through the water towards back-scattering particles within the measurement volume and then back to the instrument. Two-way transmission losses are due to attenuation by water (dependent on density) and beam spreading (attenuation by particles in suspension was ignored). Through-water-column temperature data was used to calculate variable water attenuation vertically and temporally (with constant salinity and pressure).

The correction to the backscatter estimation method by Gostiaux and van Haren [2010] for low signal-to-noise data was not used for this work as uncorrected backscatter was always much higher than instrument noise levels in the near-bed region. This may result in errors in corrected backscatter at the end of the measurement profile where noise levels were often comparable to measured levels, but we were less interested in regions further from the bed.

The ADCP receivers saturated at elevated levels, resulting in a non-linear echo response when compared to other instruments. This is a known limitation of these instrument (pers. comm. with Nortek Instruments). We removed saturated data from the analysis by applying an ADCP backscatter threshold value (82.5 dB pre-correction) determined by visual inspection. Saturation occurred most often in the lowest measurement cell and decreased with distance from the sea bed. Unfiltered data with flags applied (except ADCP saturation flags) are presented for an example 24-hour period (Figure 2.4).

Presentation and analysis of the raw parameters is typical in prior studies, usually opting to focus on quantitative hydrodynamic and turbulence analysis, but with only qualitative examination of sediment processes. To analyse sediment dynamics requires high resolution observations of the
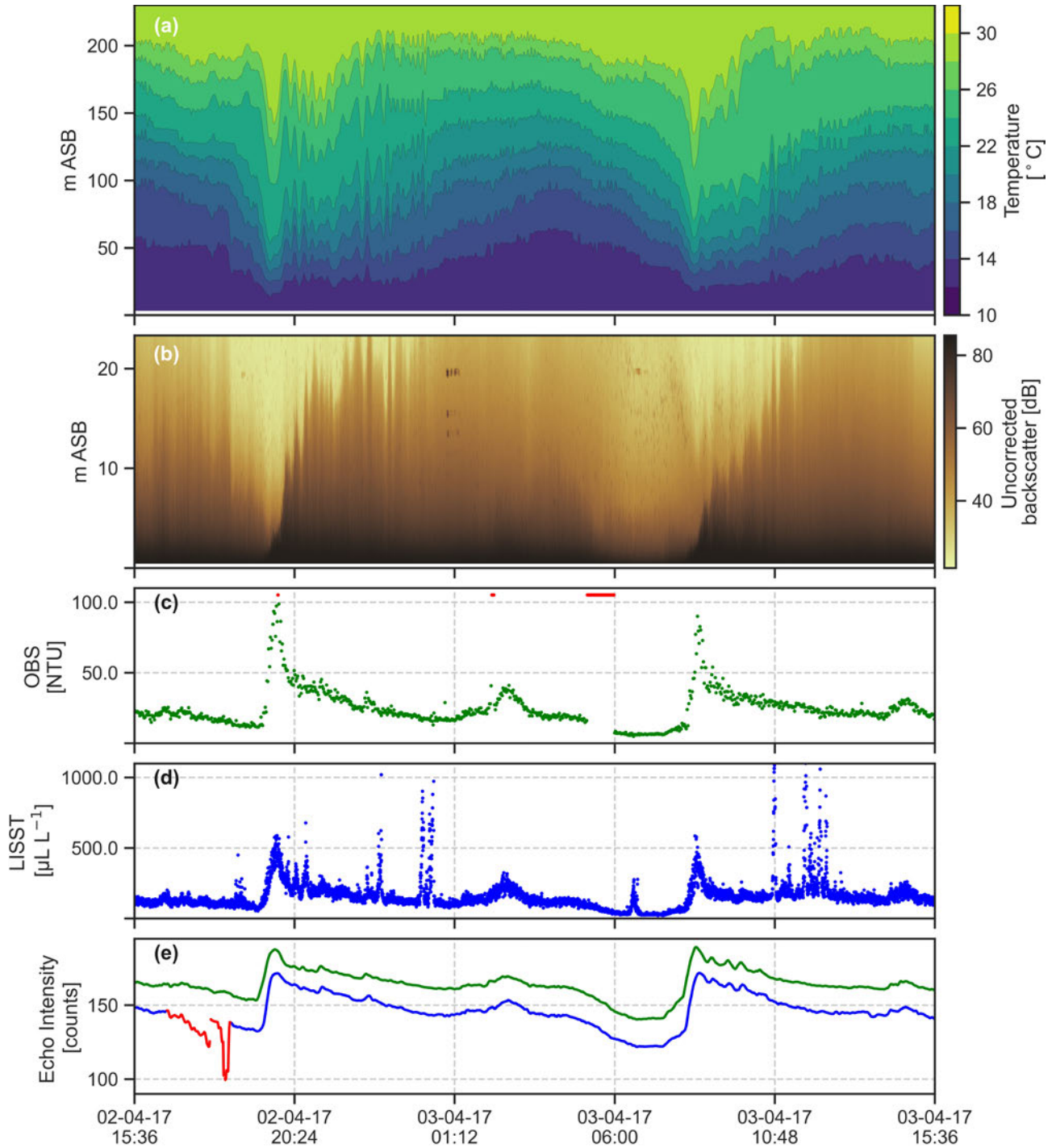
Figure 2.4: Example 24-hour period showing data from the KISSME 2017 field experiment; (a) through-water-column SP250 temperature, (b) uncorrected ADCP backscatter at 8 Hz and 0.2 m vertical resolution (saturation not flagged), (c) OBS data from 1.14 m ASB at 90 s, (d) LISST total volume concentration data from 0.87 m ASB at 12 s flagged as per manufacturer's instructions, and (e) boxcar-filtered echo intensity for the lower (green, 0.49 m ASB) and upper (blue, 1.41 m ASB) ADV. All flagged data is either red or orange. The x-axis shows the date and time in UTC.

time-rate-of-change of SSC, C_t, and relevant spatial gradients, such as the vertical gradient of SSC, C_z (here a subscript denotes a derivative along that dimension). These parameters will allow for modelling of sediment resuspension using the advection-diffusion equation, to capture the key time and space-dependent dynamics. In addition, calibration coupled with observations of current speed and direction may also allow for in-situ estimation of the sediment fluxes and their relevant contributions to C_t (i.e., the turbulent, advective, and settling fluxes).

2.4.2 Additional LISST data quality control

Further investigation of the processed LISST data revealed spikes in Cv, particle size, and attenuation that occurred during calm conditions. In addition, the spikes never registered in the acoustic or optical backscatter instruments. Comparison of Cv and mean particle diameter (d_{50}) to current speed indicated that the spikes only occurred during calm conditions, indicating they resulted from sediment flocculation (Figure 2.5a,b). This is because flocculation of sediment particles results in the formation of larger flocs with a greater proportion of water (i.e., a lower effective density), resulting in an increase in the observed volume concentration and mean particle size, without a corresponding increase in the actual mass concentration of suspended sediment. Data points where the 5-minute mean current speed was less than 0.1 m s^{-1} were flagged (4.1% of total data). Although flocculation is primarily controlled by the magnitude of turbulence dissipation [Hoitink and Hoekstra, 2005], a current speed flag proved to be a simple and effective method of identifying rapid floc growth.

Comparison of $log_{10}(Cv)$ with EI from the lower ADV showed that this flag effectively captured the deviations away from the expected linear relationship (Figure 2.5c). Whenever current speed was below the threshold, particle size would grow (regardless of prior particle size), and this process would continue until current speed increased again. In contrast, when current speed was high the mean particle size appeared to stabilise (Figure 2.5b).

Mean estimates of SSC from the lower ADV (calculated later) were used to confirm that these spikes did not represent resuspension events (Figure 2.5d). Suspected resuspension events (associated with high current speeds) could be observed across all instruments, while flocculation events were only observed by the LISST. The identified flocculation events (orange dots) result in a significant response from the LISST, but no response from the ADV (Figure 2.5c,d). Note that calibration was not necessary to identify flocculation events. Flocculation results in an increase in particle size that is readily observed by the LISST, but did not significantly alter the acoustic (or optical) aggregate backscattering properties of the particles in suspension. In addition, this comparison showed that even though observations of SSC and d_{50} were strongly positively correlated at low values (below 20 mg L^{-1}), they showed no correlation at higher values.

2.5 Sediment calibration

Here we describe and compare results from the two independent calibration methods that use direct measurements of SSC, herein referred to as the *in-situ* LISST method and the *laboratory* OBS method. We then describe how indirect observations of SSC were connected together using the vertical profile of acoustic backscatter from the ADCP and present the resulting calibration model parameters.
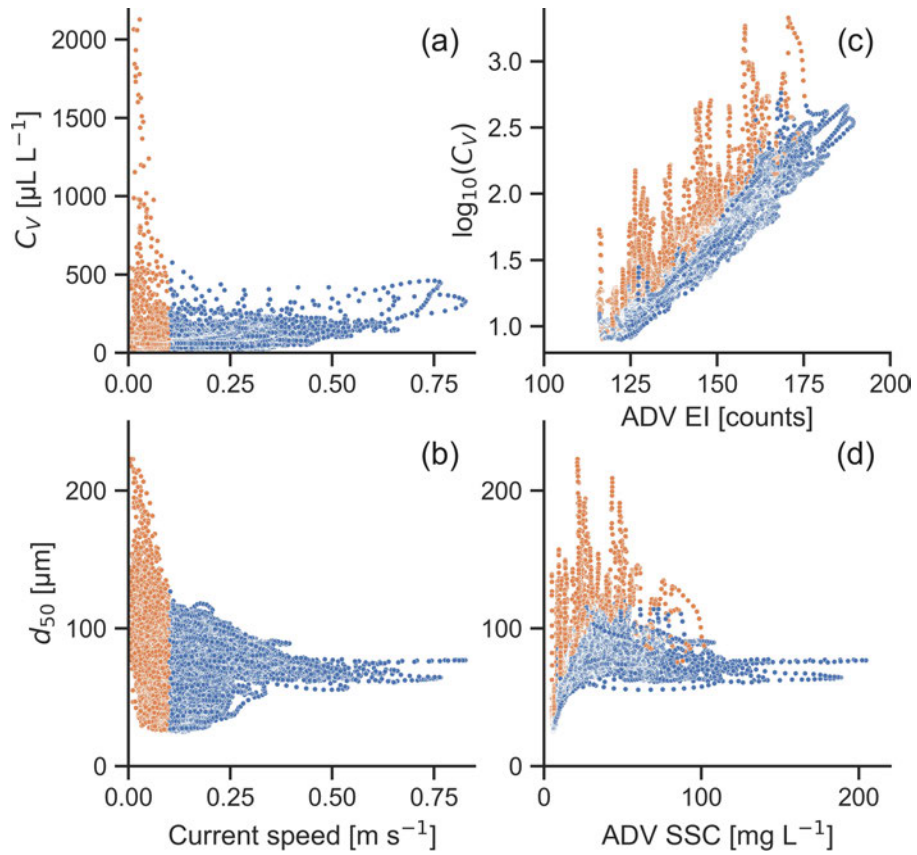
Figure 2.5: LISST data (Cv and d_{50}) with current speed (a,b), ADV echo (c) and ADV SSC estimates (d) used to identify instances of flocculation. Cv and d_{50} are total volume concentration and mean particle diameter from the LISST at 0.87 m ASB, respectively. Current speed, ADV echo and ADV SSC are all from the lower ADV deployed at 0.49 m ASB. Orange points represent times when the 5-minute mean current speed was less than 0.1 m s^{-1} as measured at the lower ADV, and blue is the rest of the data. Unlabelled axes are shared.

Figure 2.6: *In-situ* calibration results for the LISST: (a) sampling approximation to the posterior
probability distribution for the model parameters, m and b, showing the mean with 68% and 95% highest
probability density contours, (b) sampling approximation to the posterior probability distribution
for the model residual term σ_y (mean in black, each chain coloured), and (c) data (dots) and mean
outcome (line) with the 95% CI (grey shading).

Limitations of the data and the methodology are discussed in the context of the calculated uncertainty.

2.5.1 In-situ LISST method

The *in-situ* calibration method involved intensive ship-based vertical profiling near the lander mooring
location (Figure 2.2ii). A LISST was fixed to the *RV Solander's* CTD-Rosette which profiled to collect
co-located LISST measurements and Niskin water bottle samples. The samples were collected across a
range of depths from 4 to 55 m ASB. The profiling frame did not collect bottle samples closer than
about 4 m ASB to prevent damage. This calibration approach has been used previously for continental
shelf and slope studies [e.g., Gardner et al., 1985; Puig et al., 2001].

We vacuum filtered water samples using 0.4 µm pre-weighed filter paper to determine SSC. Filtered
samples were washed with deionised water and dried before weighing. A total of 47 bottle samples
were collected within 1,400 m of the lander that ranged from 0.12–15.68 mg L^{-1} with a median and
mean of 0.35 and 2.16 mg L^{-1}, respectively.

We used MCMC sampling (4 chains for 5,000 iterations with 2,000 tuning steps) to calculate the
posterior probability distribution for the slope and intercept, m and b (Figure 2.6a), and the residual
variance parameter, σ_y (Figure 2.6b). A normal distribution with a mean of zero and a standard
deviation of 10 were used for model priors. The model results were stationary and ergodic (repeatable)
indicating that the posterior distributions were suitable for inference [Gelman et al., 2013]. Posterior
predictive samples were drawn from the model for values from 0 to 100 µL L^{-1}, which allowed for
estimation of the 95% posterior predictive CI (Figure 2.6c - grey shading).

The 95% CI were calculated for each model parameter (Table 2.2) and for estimates with a mean
SSC value of 100 mg L^{-1} (Table 2.3). The posterior distribution was approximately normal and the
95% CI remained relatively constant up to 5.0 (3.0, 7.0) mg L^{-1}. After this CI began to increase,
reaching 20.0 (17.4, 22.6) mg L^{-1}, and up to 100.0 (90.9, 108.2) mg L^{-1}. This was driven by variability
in the slope parameter owing to a lack of bottle samples at high SSC. Only 16 data points with SSC
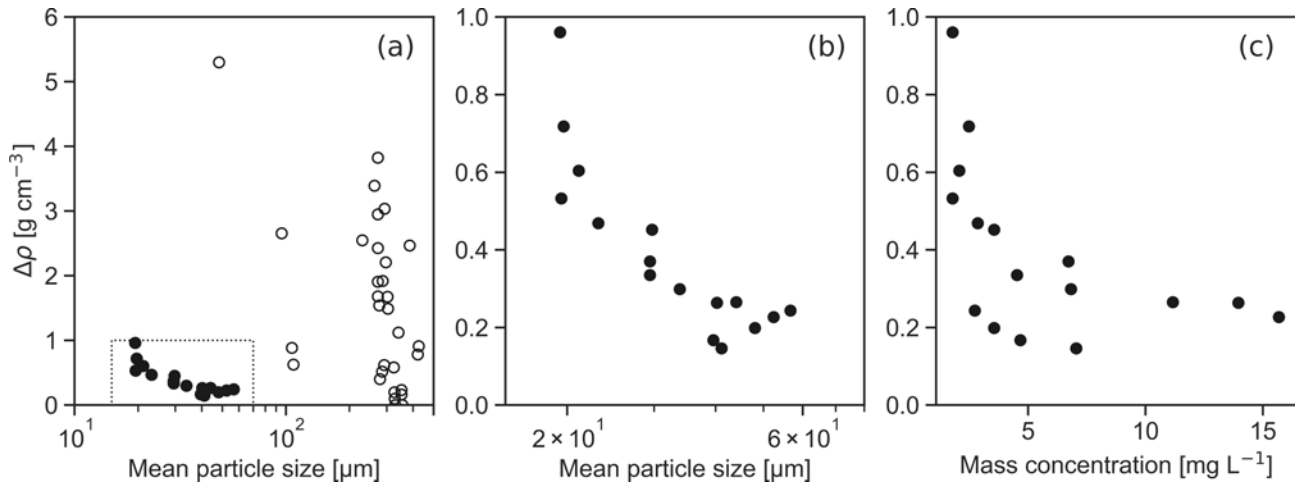
Figure 2.7: Calculated effective density, $\Delta\rho$, from in-situ data (a) for all samples (unfilled) and the 16 samples with SSC greater than 1.00 mg L^{-1} (filled), (b) inset of (a) (dashed box), and (c) against measured SSC.

greater than 1.00 mg L^{-1} were collected from the 47 bottles (Figure 2.7).

The weighted mean effective density for all samples, $\Delta\rho$, was represented by the slope, $m = 0.22$ (0.20, 0.24) (Figure 2.6c). This was similar to zero order aggregates observed by Krone [1986] and samples analysed by Mikkelsen and Pejrup [2001]. This low density (only 22% higher than water) suggested, for higher concentration bottle samples at least, that most of the observed particles were flocs, as flocs are primarily composed of water (by volume). If most of the observed particles were disaggregated primary particles then an effective density closer to 1.6 would be expected. The effective density was not constant, however, and appeared to be a function of particle size for samples over 1.00 mg L^{-1} (Figure 2.7a,b). Inclusion of mean particle size as an independent variable in the model did not have a significant effect on posterior predictive CI. It was decided not to include particle size in the model, mainly because of the low number of useful data points and uncertainty on how well the bottle samples (collected at 4 m ASB and higher) represented conditions at the deployment height.

2.5.2 Laboratory OBS method

The OBS instrument from the lander was calibrated post-deployment in the laboratory. We used the sediment grab sample collected at the lander site to assess the instrument response in a recirculating tank, and our method followed SSC laboratory calibrations described previously by Downing and Beach [1989]; Ludwig and Hanes [1990].

The key steps were:

1. water was recirculated in a 60 L tank to homogenise the sediment concentration;

2. OBS measurements (at 1 Hz) were taken in the tank, and a concurrent water sample was taken over a 30 second period, yielding 30 OBS data points per single SSC value;

3. the water sample was filtered and weighed as per the *in-situ* method;

4. more sediment was progressively added to increase SSC, and the process was repeated.

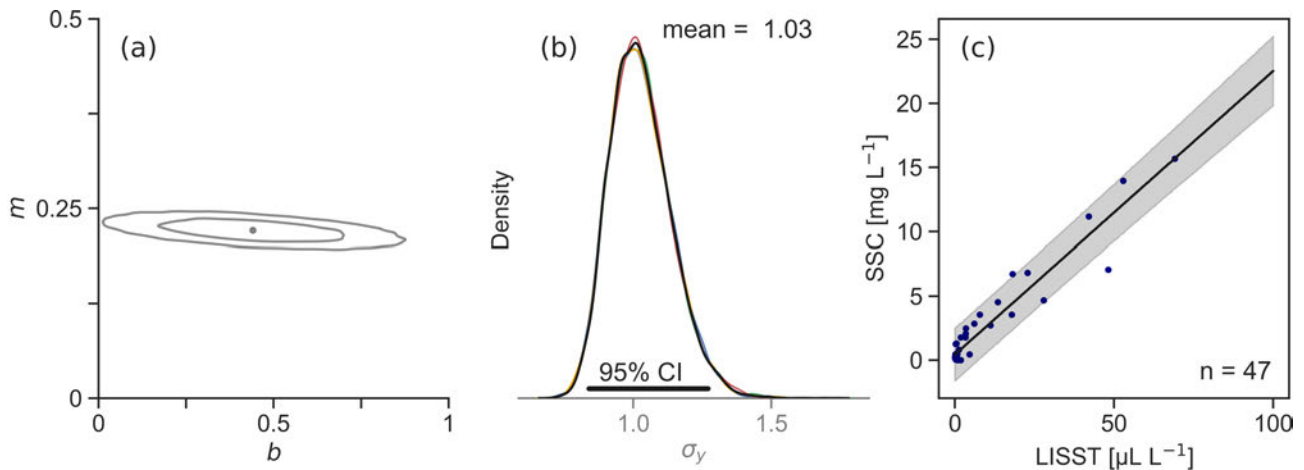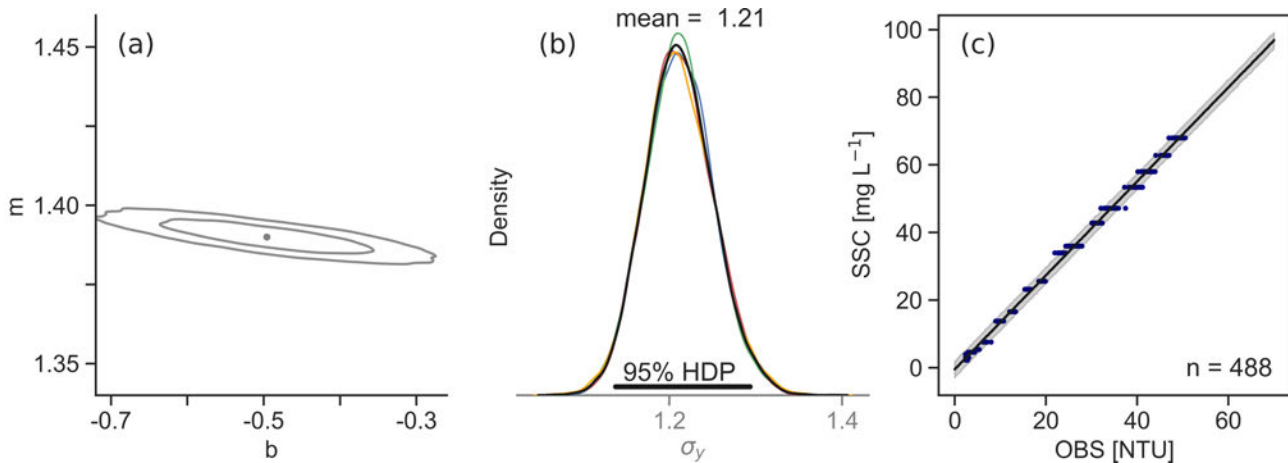**Figure 2.8:** *Laboratory* calibration results for the OBS: (a) sampling approximation to the posterior probability distribution for the model parameters, m and b, showing the mean with 68% and 95% highest probability density contours, (b) sampling approximation to the posterior probability distribution for the model residual term σ_y (mean in black, each chain coloured), and (c) data (dots) and mean outcome (line) with the 95% CI (grey shading).

Measured SSC ranged from 2.2–68.0 mg L^{-1}. OBS fluctuations in clear water (no sediment) with the pump running were less than ± 1 NTU, but grew larger as SSC increased.

We calculated the model parameters in the same manner as the *in-situ* results (Table 2.2, Figure 2.8). MCMC sampling (4 chains for 5,000 iterations with 2,000 tuning steps) was used to approximate the posterior distribution for m and b (Figure 2.8a), and σ_y (Figure 2.8b). Posterior predictive samples of OBS data were drawn with a range of 0-70 NTU, which were used to calculate the 95% CI (Figure 2.8c - grey shading).

The posterior predictive CI remained relatively constant up to 100 (97.4, 102.4) mg L^{-1}. This was owing to our ability to control SSC in the laboratory and thus evaluate the instrument response at high concentrations. This resulted in significantly reduced uncertainty for predictions at 100 mg L^{-1} compared to the *in-situ* LISST calibration, despite having similar uncertainty for mean values under 20 mg L^{-1}.

The use of freshwater and an energetic pumping process were expected to limit flocculation, potentially increasing OBS response (per unit SSC). Conversely, fine sand particles with a faster settling rate, were probably not observed during profiling, but were expected to remain suspended in the tank, potentially decreasing the OBS response (per unit SSC) (note particles in this size class were observed by the LISST during profiling, but no analysis of filtered samples was performed to determine whether these were flocs or primary particles). Attempts to measure PSD in the tank were inconclusive (likely due to bubbles introduced by the recirculation pump), so any difference between *laboratory* and *in-situ* conditions could not be determined.

2.5.3 Comparison of direct calibrations

We used field data to compare SSC estimations from the *in-situ* and *laboratory* calibrations. Note that the OBS (1.14 m ASB) was located 0.27 m above the LISST (0.87 m ASB) and therefore would be expected to measure slightly lower SSC due to an expected decrease in SSC away from the seabed.
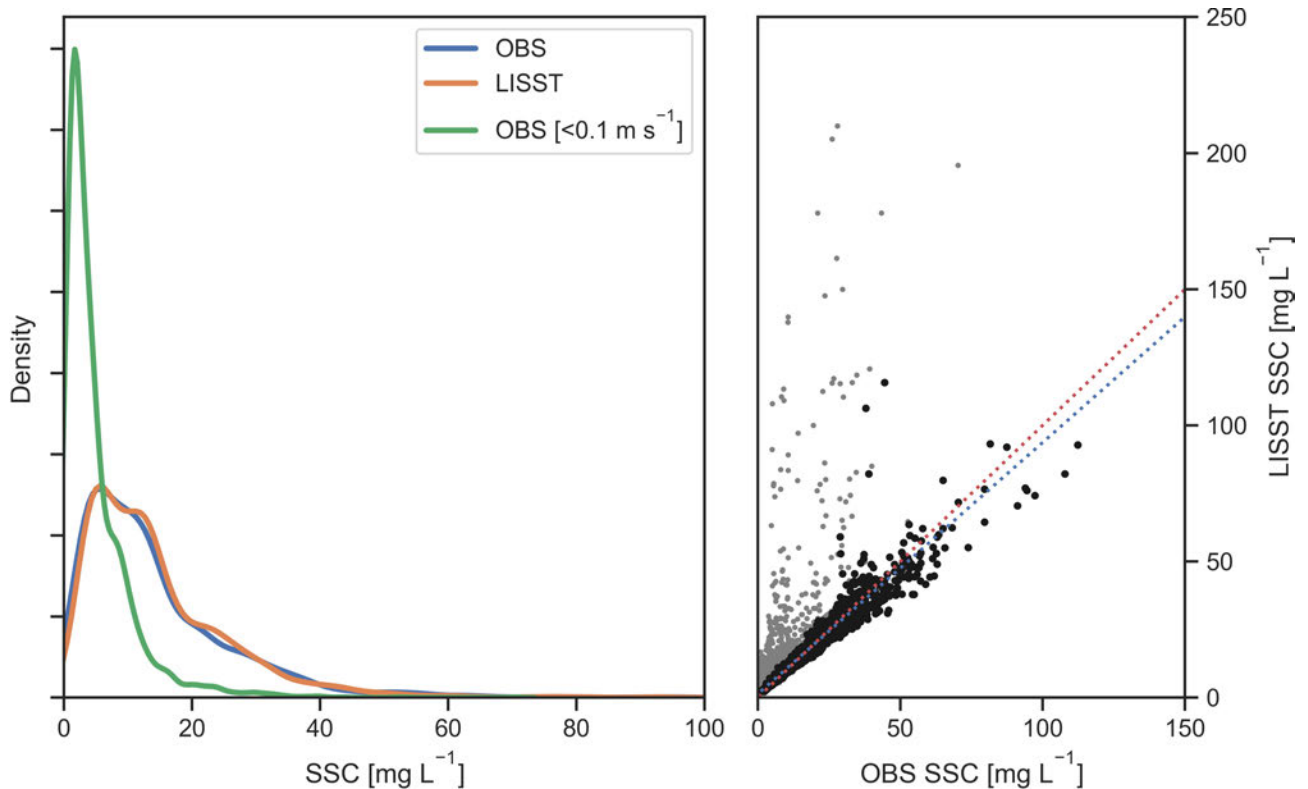
Figure 2.9: Comparison of the direct calibrations; (left) histograms of SSC estimates for the entire field deployment from the OBS and LISST calibration models; and (right) a comparison of the OBS and LISST SSC mean estimates (black dots), with data points where current speed was less than 0.1 m s^{-1} identified (light grey), and the 1:1 line (dotted red) and maximum *a posteriori* least-squares fit (dotted blue).

The 5-minute block-averaged data sets were converted to point estimates of SSC using the mean of the slope and intercept parameters from each model. Blocks where the current speed was less than 0.1 m s^{-1} were separated from the comparison as per the LISST flagging.

The calculated SSC from the OBS and LISST field data sets compared well for the bulk of the data (Figure 2.9), although scatter increased with SSC. The maximum *a posteriori* slope calculated by linear least-squares fitting of the data sets was 1.08 (Figure 2.9 - right), which indicated that the OBS generally estimated SSC slightly higher than the LISST, despite being moored 0.27 m above it.

2.5.4 Connection to acoustic instruments

In shelf seas, direct sampling adjacent to deployed instruments is usually not feasible. We overcame this difficulty by comparing data from the OBS, LISST, and each ADV to the ADCP backscatter vertical profile at the height of each instrument. The 1 MHz ADCP profile was the key to inferring SSC at different heights because it gave us concurrent observations with every other instrument on the lander (in height ASB and time, Figure 2.3). The corrected ADCP backscatter was linearly interpolated to the height of the relevant instrument. Processed data from each of the deployed instruments could then be compared, e.g., OBS to ADCP, ADCP to ADV.

Each calibration model was assumed to be a linear model, based on theory and studies discussed

2. CALIBRATED SUSPENDED SEDIMENT OBSERVATIONS BENEATH LARGE AMPLITUDE NON-LINEAR INTERNAL WAVES
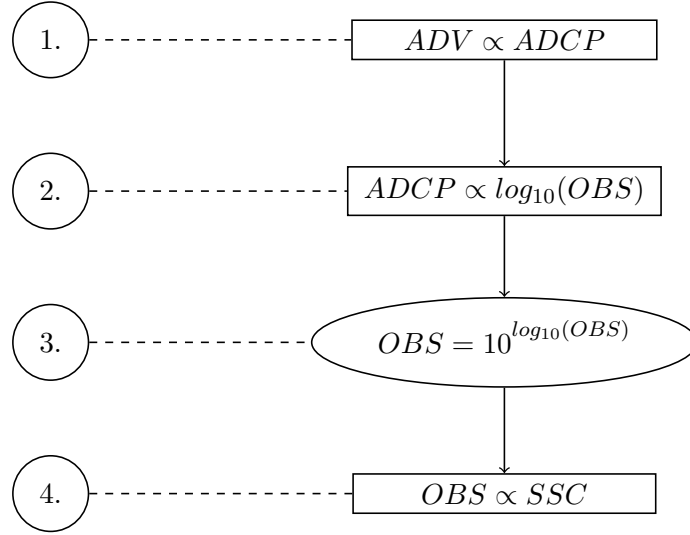
Figure 2.10: Directed acyclic graph of the connected models used to infer SSC for instruments where a direct calibration was not undertaken. The rectangular nodes in steps 1, 2, and 4 are the linear models, with the general form presented previously (Figure 2.1). The ellipse in step 3 represents the conversion from the log_{10} decibel scale. Step 4 is the *laboratory* (or *in-situ* calibration. Linear models are shown as $x \propto y$. The LISST models could also be substituted for the OBS in steps 2 to 4 to predict SSC for the ADCP or either ADV.

previously [e.g., Fugate and Friedrichs, 2002; Gartner, 2004; Ha et al., 2009; Kim and Voulgaris, 2003]. Hence, inference of SSC for each ADV required propagation of raw ADV echo measurements through three connected linear models, plus a scale conversion: 1) ADV to ADCP 2) ADCP to log_{10}OBS (or log_{10}LISST) 3) conversion from decibel scale and 4) OBS (or LISST) to SSC (Figure 2.10). Once each calibration model was established individually, a single value from either ADV could be sampled n times through the chain of models to give n estimates of SSC, the distribution of which contained the estimate of total uncertainty from the entire process.

The four calibration models utilizing the ADCP backscatter measurements were labelled as: ADCP-OBS, ADCP-LISST, ADV141-ADCP, and ADV049-ADCP (the latter two are the ADV at 1.41 m and 0.49 m ASB). Blocks where the average current speed was less than 0.1 m s^{-1} were not used in any model. The models were computed in the same manner as the in-situ and laboratory models (results in Figure 2.11 and Table 2.2). The standard deviation of the prior for the intercept was increased to 50 for the ADV models. Full data return for the period 2 to 16 April would be $n = 6624$, but this was significantly reduced by ADCP saturation (which was worse closer to the sea bed) and the current speed flag (data return shown in Figure 2.11).

The influence of particle size on each of the four models was assessed by comparison against multivariate linear models that employed LISST d_{50} information as an additional variable (i.e., with the form $y = mx + cd_{50} + b$, where c is a new free parameter). There was a slight reduction in the ADV141-ADCP model 95% CI for this model specification (not shown), but no improvement for the other models (note a reduction in the 95% CI would indicate an improvement in model capability). Final estimates of SSC from the multivariate models were virtually the same for both ADV, but increased significantly for ADCP estimates towards the upper end of the acoustic profile, far from where d_{50} was measured.
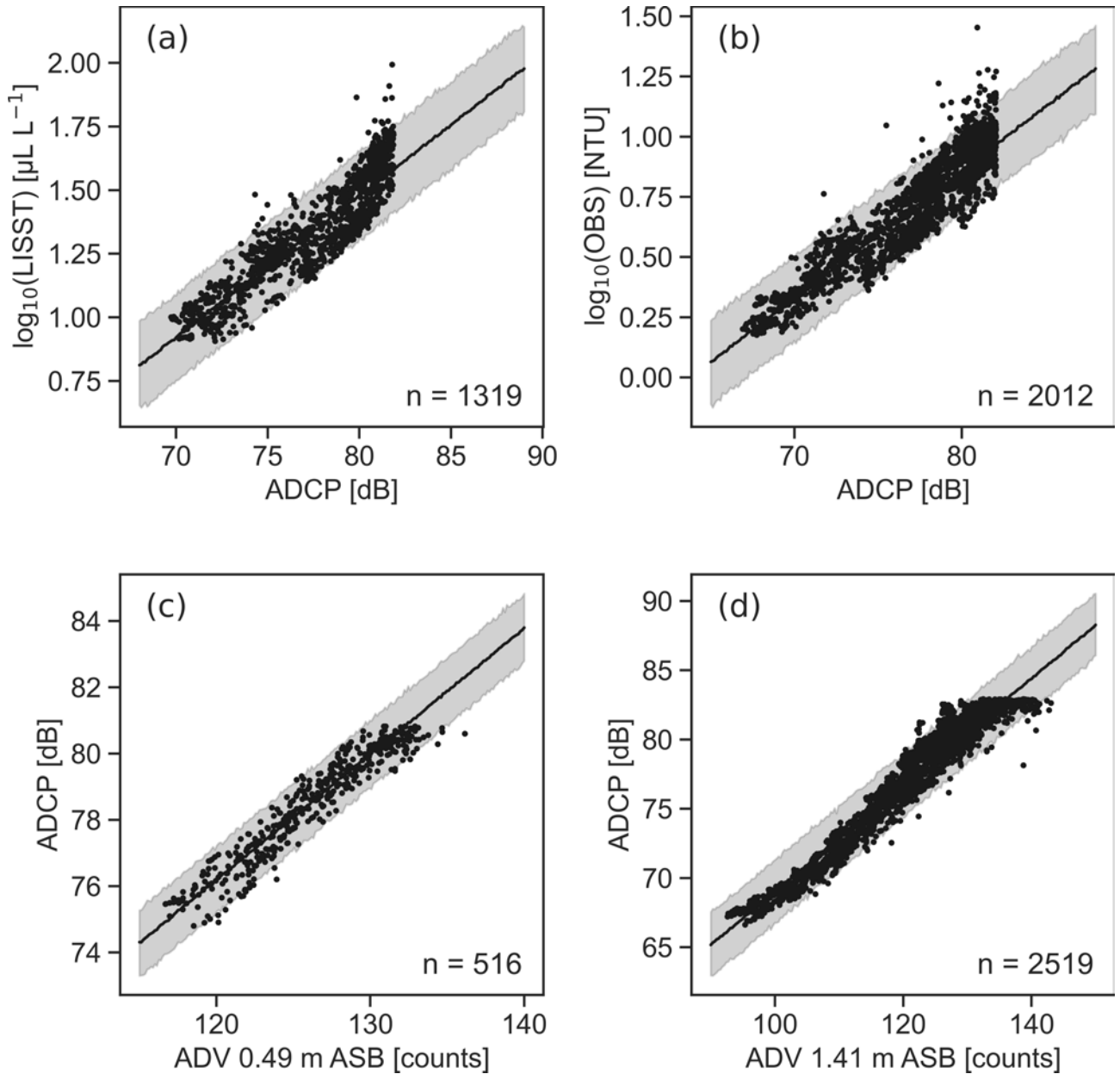
Figure 2.11: Data (dots) and mean regression outcome (line) with the 95% CI posterior predictive intervals (grey shading) from model sampling for the ADCP linear model with (a) the LISST, (b) the OBS, (c) the lower ADV, and (d) the upper ADV. The number of good data points used for each model, n, is shown in each subplot.

Table 2.2: Bayesian linear model mean parameter estimates with the 95% CI shown in brackets

Model	b	m	σ_y
OBS - SSC (*laboratory*)	-0.497 (-0.669, -0.326)	1.39 (1.38, 1.40)	1.21 (1.140, 1.29)
LISST - SSC (*in-situ*)	0.438 (0.105, 0.772)	0.221 (0.201, 0.240)	1.03 (0.837, 1.27)
ADCP - OBS	-3.73 (-3.79, -3.67)	0.0559 (0.0551, 0.0567)	0.0916 (0.0885, 0.0948)
ADCP - LISST	-3.18 (-3.27, -3.08)	0.0622 (0.0609, 0.0634)	0.0882 (0.0849, 0.0916)
ADV 0.49 m - ADCP	30.6 (29.4, 31.9)	0.380 (0.369, 0.390)	0.521 (0.489, 0.555)
ADV 1.41 m - ADCP	30.8 (30.3, 31.3)	0.383 (0.379, 0.387)	1.18 (1.15, 1.21)

2. CALIBRATED SUSPENDED SEDIMENT OBSERVATIONS BENEATH LARGE AMPLITUDE NON-LINEAR INTERNAL WAVES

Table 2.3: Upper and lower 95% credible interval SSC estimates for each instrument and pathway (where applicable), based on predictions at a mean value of 100 mg L^{-1}.

Model	SSC 95% CI (mean of 100 mg L^{-1})
OBS	97.4, 102.4
LISST	90.9, 108.2
ADCP (via OBS)	58.3, 160.5
ADCP (via LISST)	52.6, 173.8
ADV 0.49 m (via OBS)	56.2, 165.0
ADV 0.49 m (via LISST)	50.8, 176.4
ADV 1.41 m (via OBS)	54.0, 167.3
ADV 1.41 m (via LISST)	50.9, 177.8

It is noteworthy that all three variables, x, y, and d_{50}, were highly correlated for the range of values (the low end) used in these models (as shown in Figure 2.5d). This is because the ADCP saturation removed high concentration data points where acoustic, OBS, and LISST Cv data became uncorrelated with d_{50}. This restricted data set appeared to overestimate the contribution of d_{50} in the models. Given the similarity in SSC predictions for the ADV, the poor SSC predictions for the ADCP, and the minimal improvement in total uncertainty, we decided to not to use the multivariate models for SSC estimation. We note, however, that improvements can be made with better ADCP data return. Information at more points along the ADCP profile would also allow for a more sophisticated calibration model [e.g., Sassi et al., 2012].

Estimation of SSC from ADCP and ADV measurements using the connected models was possible via either the LISST or OBS direct calibrations (Figure 2.10). Note that Step 4 is the direct calibration model described previously (either the *laboratory* or *in-situ* method can be used here). Each time predictions are drawn from a model there is growth in uncertainty. When connecting together multiple models the propagation and growth of this uncertainty can become a significant consideration. Growth of the 95% CI was estimated for a single ADV echo value utilising the LISST model pathway (Figure 2.12). The width of the 95% CI (about the mean) increased to 7.8% at step 1, to 17.5% at step 2, to 109% at step 3, and to 116% at step 4 (these steps align with Figure 2.10).

The 95% CI from sampling any individual model was less than ±10% of the mean prediction. Transformation from log_{10} space, whilst not adding any additional uncertainty itself, nevertheless increased the variance (about the distribution mean) and skewed the sample distribution (Figure 2.12 - step 3). This step was necessary, however, as the acoustic instruments native measurements were on a decibel scale. The final 95% CI width for an ADV measurement propagated through the chain was almost 125% (Figure 2.12 - step 4).

The SSC 95% CI were estimated for all instruments (using both the LISST and OBS pathways where possible) at a mean SSC of 100 mg L^{-1} (Table 2.3). There was a marked difference between the final CI for the different instruments and model pathways. Using the OBS pathway rather than the LISST pathway, only reduced the final CI width by about 4% for the acoustic instruments. Given the LISST was sensitive to flocculation, all estimates of SSC from the acoustic instruments presented hereafter therefore used the OBS calibration pathway, unless stated otherwise.
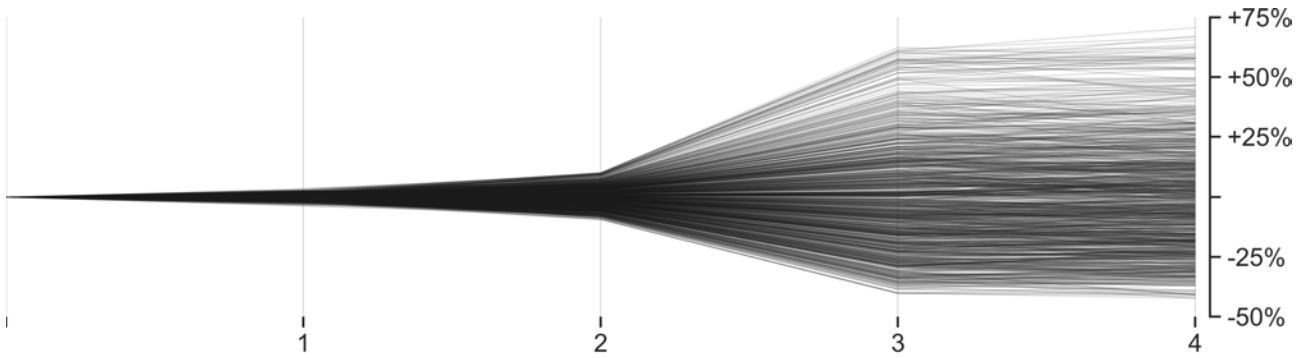
Figure 2.12: Propagation of a single backscatter value from ADV 1.41 m ASB sampled 1,000 times through the four transformations shown in Figure 2.10 using the LISST models. Lines represent the 95% highest probability results of the 1,000 samples.

2.6   Sediment dynamics influenced by NLIW passage

2.6.1   Hydrodynamics

Baroclinic dynamics and boundary layer turbulence at this site have already been examined in two previous studies [Rayson et al., 2019; Zulberti et al., 2020]. Relevant observations from their work are summarised here and the reader is directed to these previous studies for more information.

Baroclinic motion in the form of an internal tide was observed in the through-water-column temperature record throughout the period 2 to 16 April 2017 (Figure 2.13a), with increased amplitude during spring tides [Rayson et al., 2019]. Mode-1 NLIW of depression with amplitudes up to 70 m propagated past the moorings in the first few days of the deployment, just after the peak barotropic spring tide, generating strong near-bed currents and elevated SSC (e.g., at 0.87 m ASB). These waves propagated southeast towards the coast, approximately cross-shelf, with near-bed currents directed offshore and near-surface currents directed onshore. Regular mode-2 NLIW with amplitudes up to 50 m were also observed later in the record, but here we focus on the strongest mode-1 events early in the record.

Peak barotropic tidal velocity was approximately 0.4 m s^{-1} and tidal range was about 4 m. The maximum near-bed current speed driven by baroclinic motions was estimated at 0.6 m s^{-1} during the two largest NLIW events [Zulberti et al., 2020]. Both these events occurred when the tide was directed offshore at around 0.2 m s^{-1}, hence the maximum combined (measured) current for the deployment was around 0.8 m s^{-1} at 0.49 m ASB (Figure 2.13b). Baroclinic amplitude reduced significantly during the following neap tide and began to increase again as the barotropic tidal range increased. During the second spring tide, however, baroclinic motion was more linear and peak amplitudes and near-bed baroclinic induced currents were significantly smaller than during the first spring period.

Zulberti et al. [2020] demonstrated that the height of the log-layer was generally on the order of 1 m thick. Zulberti et al. [2020] also examined the development and height of the mixing layer, i.e., the bottom boundary layer characterised as a low stratification region attached to the bed and capped by a thin zone of high stratification (the mixing layer pycnocline, herein mixing layer height). They found the mixing layer height was generally on the order of 10 m ASB, and varied over time due to boundary layer growth and shedding during each tidal cycle and modulation by baroclinic motion. They also

showed that ADCP backscatter was elevated within the mixing layer and decreased significantly at the mixing layer height.

2.6.2 Sediment dynamics over a spring-neap tidal cycle

Using the calibration models it was straightforward to convert time series of raw data (such as ADV echo intensity) to estimates of SSC with uncertainty. A time series of 20,000 SSC sample estimates was generated using the boxcar-filtered data for each instrument. From these samples the mean outcome and CI were then calculated, and several other quantities were also able to be derived.

Estimates of mean SSC were calculated for the ADCP, OBS, and each ADV for the period 2 to 16 April (Figure 2.13c,d). Estimates of uncertainty are shown in later figures as they were difficult to observe at this time scale. Temperature data from the nearest through-water-column mooring and mean horizontal current speed at the ADV 0.49 m ASB give context to the observations (Figure 2.13a,b). Current speed measurements were converted to bed shear stress estimates, τ_{bed}, using the quadratic drag law with $C_d = 0.00185$ [Zulberti et al., 2018].

Near-bed SSC peaks were positively correlated with bed stress in both time and magnitude. SSC at the lower ADV repeatedly increased to around 100 mg L^{-1} when τ_{bed} reached 0.69 N m^{-2}, and always showed some response when τ_{bed} exceeded 0.08 N m^{-2} for a 5-minute block (roughly 0.2 m s^{-1}). SSC from the ADCP showed intermittent bursts of elevated SSC (over 5 mg L^{-1}), occasionally reaching more than 20 m above the bed throughout both spring tidal cycles (Figure 2.13c). Interference from reflections off instruments on the lander T-string were also observed in the ADCP record (small dark brown patches in Figure 2.13c).

Current speed and mean SSC from the lower ADV (0.49 m ASB) were used to estimate the horizontal sediment flux at this elevation. Each NLIW (near the start of the deployment) generated strong near-bed currents in the off-shelf direction that drove a significant short-term asymmetric SSC flux (not shown). This flux time series was used to calculate the wavelet power spectrum (Figure 2.13e), demonstrating the ability the short-period NLIW to drive enhanced horizontal sediment fluxes, which subsequently enhanced the transport ability of longer time-scale motions (around half the M2 tidal frequency). In general, mean SSC was about twice as high during the first spring tidal cycle when the NLIW were the largest and, as a result, the flux at tidal timescales was significantly greater (Figure 2.13d,e).

2.6.3 Sediment resuspension under non-linear internal waves

The two largest NLIW were around 12 hours apart and occurred near the beginning of the deployment (Figure 2.14a), denoted Wave 1 and Wave 2. Both waves were composed of a well-defined leading wave of depression with isotherm displacement amplitudes of about 60 and 70 m, respectively. The well-defined leading wave was followed by a series of smaller oscillations. The NLIW-induced currents measured at 0.49 m ASB were superimposed on the background barotropic and linear baroclinic motions (Figure 2.14b). We used the high resolution 8 Hz ADCP backscatter to estimate SSC over the bottom 23 m using the mean of the calibration parameters only (Figure 2.14c).

Mixing layer dynamics were analysed in detail by Zulberti et al. [2020], who demonstrated that the sharp drop in ADCP backscatter was a suitable proxy for the mixing layer height. We find that
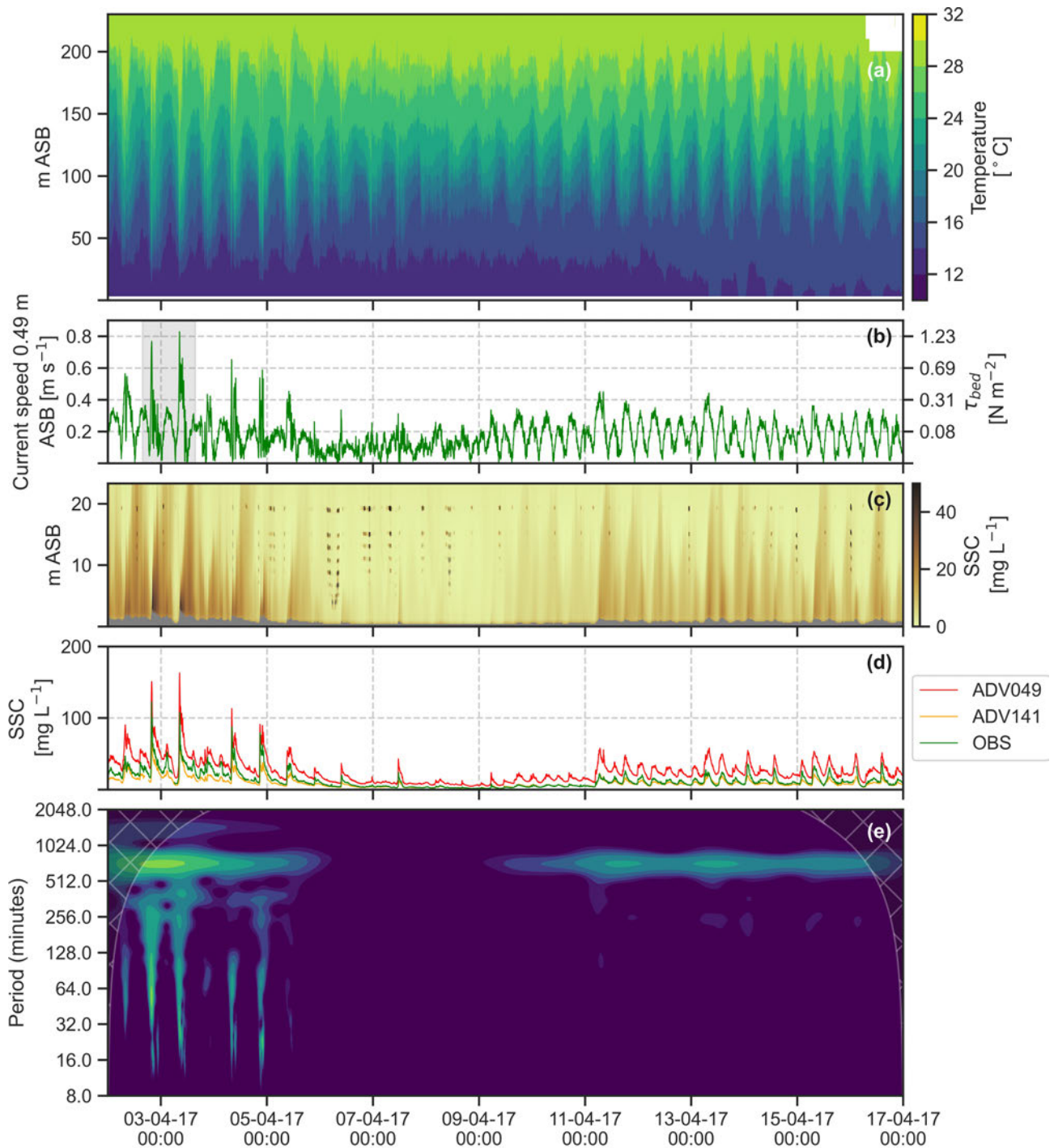
Figure 2.13: KISSME 2017 deployment data; (a) through-water-column temperature from SP250, (b) boxcar-filtered current speed measured at 0.49 m ASB (with conversion to bed stress on the right y-axis), (c) calibrated ADCP backscatter with grey areas indicating receiver saturation, (d) mean estimates of SSC, and (e) the wavelet power spectrum of cross-shelf sediment flux at 0.49 m ASB using the ADV current speed and mean SSC estimate. The grey shading in (b) indicates the bounds of Figure 2.14. The x-axis shows the date and time in UTC.

this sharp drop in backscatter is the location of a strong vertical gradient in estimated SSC (Figure 2.14c, 2.15c, 2.16c). During the two NLIW events presented here, the estimated SSC decreased from up to 40 mg L^{-1} to background levels close to 0 mg L^{-1} over a 1 m change in height at the edge of the mixing layer. This suggests that the mixing layer pycnocline plays an important role in restricting the vertical extent of sediment resuspension, likely via a sharp decline in eddy diffusivity across the stratified boundary.

Uncertainty in the SSC estimates from the ADCP, and hence uncertainty in the mixing layer height, was investigated by calculating the location of an arbitrary SSC isopleth at 10 mg L^{-1}. The box-car filtered backscatter was converted to 1,000 estimates of SSC and then 1,000 estimates of the 10 mg L^{-1} contour line. The mean and 95% CI of these contours (Figure 2.15c and 2.16c) provides a proxy estimate of the SSC gradient at the edge of the mixing layer, with narrow CI indicating a steeper vertical gradient and wide CI suggesting the mixing layer pycnocline is more diffuse. The narrow CI also indicate greater confidence in the mixing layer height estimate. This type of analysis could also be used to estimate the penetration characteristics of light in shallow areas or some cut-off of engineering operational importance (e.g., a zone beyond which visibility is likely to be too low to perform maintenance operations).

Mean and 95% CI of SSC were calculated for each ADV, the OBS, and the LISST (Figure 2.14d). As discussed above, SSC estimates from the LISST were highly sensitive to flocculation and thus showed significant deviations from the other instruments when the current speed was less than 0.1 m s^{-1}. These deviations were always accompanied by significant spikes in mean particle size (Figure 2.14e) and beam attenuation (not shown). The size of these spikes was weakly positively correlated with both the length of time the currents remained low and the SSC prior to each quiescent period. This resulted in LISST volume concentration and beam attenuation spikes that were not correlated with current speed (or bed stress). This process of rapid floc growth during calm periods may be another cause of uncorrelated beam attenuation spikes worth considering in fine-grained marine environments, in addition to previously suggested causes, such as vertical velocities resulting from global instabilities [Bogucki et al., 1997]; and trawling activities [Churchill et al., 1988; Martín et al., 2014; Ribó et al., 2015].

Despite near-bed SSC falling by almost a half within about 20-30 minutes of each peak, elevated SSC was maintained for up to 9 hours after the wave passage. This was likely because of slow settling flocs that continued to be advected horizontally and vertically by the internal tide. After Wave 1, particles appeared to be vertically advected up to 50 m ASB by baroclinic motion, as observed by LISST and bottle sample measurements during a profile at approximately 03:00 on 3 April, 2017 (not shown).

More detail in SSC and its uncertainty is evident when we focus on the NLIW events (Figure 2.15 and Figure 2.16). During Wave 1, the bed stress peaked at approximately 1.2 N m^{-2} under the wave trough. Cross-correlation of phase-lagged current speed and SSC signals suggested that sediment concentration lagged current speed by approximately 6 and 13 minutes at 0.49 and 1.41 m ASB, respectively, although the peak values only lagged by 0 and 5 minutes, respectively.

The peak estimate of SSC during Wave 1 was 150 (93.7, 233) mg L^{-1} at the lower ADV, 78.8 (47.1, 125) mg L^{-1} at the upper ADV, and 102 (93.2, 112) mg L^{-1} for the LISST. There was incomplete data

return for the OBS during Wave 1 when turbidity exceeded the instrument upper limit. Maximum C_t at the lower ADV peaked at 0.14 (0.09, 0.21) mg L^{-1} s^{-1} (Figure 2.15g). Elevated SSC was confined close to the bed until the initial wave trough passed and an upward vertical velocity (not shown) was measured by the ADCP (Figure 2.15c). We also observed good agreement between the vertical displacement of isotherms and SSC from the ADCP, especially during Wave 1 (Figure 2.15a,c). This is in contrast to observations from Quaresma et al. [2007], who showed backscatter opposing isotherm movement.

Wave 2 exhibited similar peak magnitudes of current speed and SSC, although the average current speed was higher than during Wave 1 (Figure 2.16). SSC estimates peaked at 161 (101, 246) mg L^{-1} at the lower ADV, 79.0 (46.9, 129) mg L^{-1} at the upper ADV, 108 (106, 110) mg L^{-1} for the OBS, and 82.4 (75.0, 90.0) mg L^{-1} for the LISST. For the lower ADV, the maximum C_t peaked at 0.14 (0.09, 0.21) mg L^{-1} s^{-1} (Figure 2.16g), equal to the maximum C_t estimate under Wave 1. In general C_t was more uncertain when it was large (positive or negative), and showed reduced uncertainty when it was closer zero. For Wave 2, the wave form was less coherent and vertical resuspension was confined to a region closer to the bed. The SSC signal lagged current speed by approximately 4 and 9 minutes at 0.49 and 1.41 m ASB,respectively, and the peak values lagged by 3 and 7 minutes, respectively.

For both waves, there was a large and persistent positive vertical sediment gradient, C_z, between the ADV at 0.49 m ASB and the ADV at 1.41 m ASB (Figure 2.15f and 2.16f). The maximum C_z between the ADV was 94 (17, 187) mg L^{-1} m^{-1} for Wave 1 and 119 (42, 216) mg L^{-1} m^{-1} for Wave 2. C_z exhibited large uncertainty, with a maximum CI spread of around 170 mg L^{-1} m^{-1} for both waves. Uncertainty was large enough that some estimates of C_z were negative. The mean vertical gradient appears to be physically reasonable and will likely provide a useful comparison for numerical modelling. Utilising the full distribution of C_z, however, will have consequences for the estimation of the vertical turbulent flux, which uses eddy diffusivity and C_z, and may provide results with unsatisfactory levels of uncertainty. This is the subject of future research.

These estimates of a strong near-bed gradient may suggest the presence of larger primary particles with a higher density and settling velocity than the flocs (such as the fine sand component of the sediment distribution), that were generally only located close to the bed [e.g., Agrawal and Hanes, 2015]. This observation is supported by differences in the PSD between LISST data from the vertical profile measurements (at 4 m ASB and higher) and the lander observations (at 0.87 m ASB) (not shown). If these high density primary particles are abundant near the bed then SSC in this region may be underestimated. The *in-situ* direct calibration was not able to collect water samples between 0 and 4 m ASB, a limitation of the method.

We were able to observe the effect of PSD changes on SSC estimates from the LISST during Wave 1 (Figure 2.15d,e). Whilst not as significant as the spikes observed during calm periods, measurements from the LISST showed a negative correlation with current speed between 0.1 and 0.4 m s^{-1}. This resulted in an oscillation of the particle size and estimated SSC from the LISST after the leading wave. This process of floc aggregation and breakup appeared to respond almost instantly to changes in current speed. During Wave 2 (and the peak of Wave 1), when current speed was consistently greater than 0.4 m s^{-1}, the observed PSD was relatively constant. This is in agreement with observations from the LISST flagging process (Figure 2.5), that showed a de-correlation between SSC and PSD at

higher SSC values. Given the sensitivity of the LISST to particle size it is surprising that the inclusion of d_50 in the ADCP-LISST calibration model did not result in noticeable improvement. This may have been another limitation of the poor data return due to ADCP saturation.

2.6.4 Relationship between bed stress and SSC rates of change

We investigated the connection between instantaneous bed stress, τ_{bed}, and estimates of C_t at three different heights above the bed. We focused on the period spanning the large initial depression during Wave 1 from 19:08 to 20:08 on 2 April, 2017 (Figure 2.17). We observed vastly different connections between the two variables at different heights. At each height the timing of the onset of positive C_t values, the magnitude and shape of the positive C_t component, and the magnitude and shape of the negative C_t component varied significantly.

For observations nearest the bed, at 0.49 m ASB, C_t began to increase when $\tau_{bed} \approx 0.10$ N m^{-2}. This thus provides a reasonable upper bound on the critical shear stress for erosion, τ_{cr}. Using log-layer theory ($\kappa u_* z$) the estimated transport lag from the bed to 0.49 m ASB when τ_{bed}=0.10 N m^{-2} was approximately 600 s, which suggests the true τ_{cr} occurred earlier and is thus much lower. At 1.41 m ASB, C_t did not start to increase until τ_{bed} exceeded 0.25 N m^{-2}, while at 4.53 m ASB C_t was 180 degrees out of phase with τ_{bed} and only increased once τ_{bed} began to decrease.

The relationship between C_t and τ_{bed} at 0.49 m ASB appeared to be approximately linear from the time C_t started to increase, at $\tau_{bed} \approx 0.10$ N m^{-2}, up to its peak at 0.14 (0.09, 0.21) mg L^{-1} s^{-1} (when τ_{bed} was approximately 0.8 N m^{-2}). After this point C_t declined, well before τ_{bed} reaches its peak. The connection between C_t and τ_{bed} at 1.41 m ASB was similar, with maximum C_t when τ_{bed} was 1.00 N m^{-2}, slightly later than 0.49 m ASB, but still before the maximum τ_{bed}. The positive slope of C_t with increasing τ_{bed} was much greater at 0.49 m ASB than it was at 1.41 m ASB. The increase in C_t at 4.53 m ASB was coincident with falling τ_{bed} and also upward vertical velocities (measured with the ADCP). This is due to the variable hysteresis relationship between C_t and τ_{bed} with distance from the bed, showing the fundamental importance of considering time-and-space dependency.

Observations only a few metres above the bed can provide C_t estimates that appear completely uncoupled with physical forcing at the bed. Even observations within 2 m of the bed show significant variation in key characteristics related to erosion, which suggests that use of this data to directly estimate unobserved parameters such as τ_{cr} and the erosion rate may be fraught with error. The propagation of NLIW and resulting boundary layer forcing is a complex and unsteady process and accurate estimation of unobserved parameters would require modelling of the (time-and-space dependent) advection-diffusion equation.

The peak and subsequent decline in C_t at 0.49 and 1.41 m ASB prior to maximum τ_{bed} is noteworthy, with C_t being close to zero at both locations when τ_{bed} peaked. This could be due to net vertical advection, suppression of vertical mixing under the wave trough, depth-limited erosion (i.e., an increase in τ_{cr} with erosion depth), horizontal advection, or any combination of these. Horizontal advection is an important consideration when estimating erosion due to the propagation time-lag of the wave itself. Sediment upstream of the wave propagation direction experiences a delay in the onset of erosion as the wave reaches these upstream locations later, creating a spatial gradient in SSC that can then be advected back towards our mooring (for the near-bed region that experiences net offshore current).
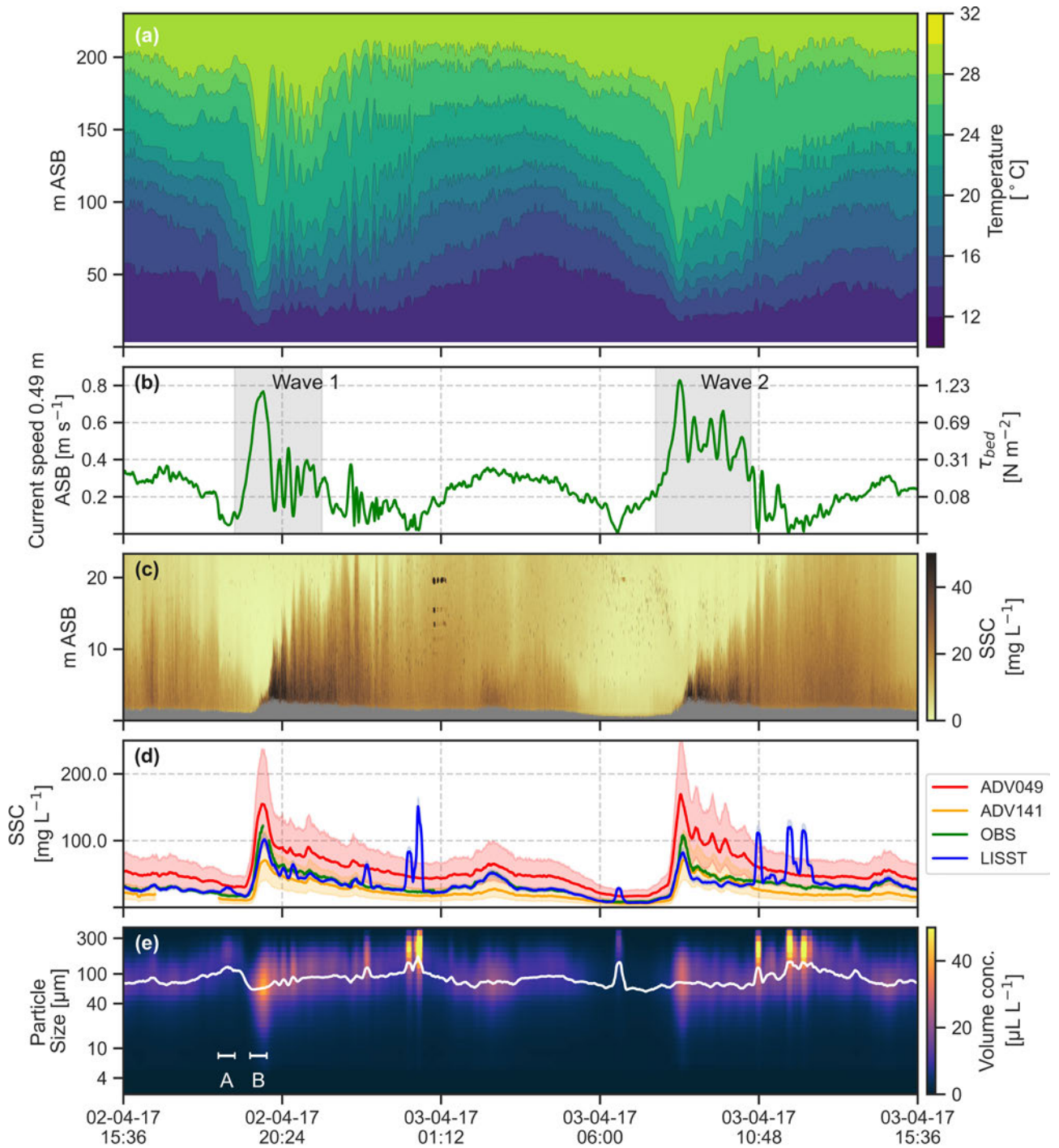
Figure 2.14: A 24-hour period (extent indicated in 2.13) showing (a) through-water-column temperature from SP250, (b) boxcar-filtered current speed measured at 0.49 m ASB (with conversion to bed stress on the right y-axis), (c) calibrated ADCP backscatter with grey areas indicating receiver saturation, (d) mean estimates of SSC including the LISST and all 95% CI, shown as coloured shading, with data points where current speed is less than 0.1 m s^{-1} included to show the effect on LISST measurements, (e) the boxcar-filtered (5-minute mean) LISST binned volume concentration data with the mean diameter (white line). Grey shading on (c) indicates the bounds of Figure 2.15 (Wave 1) and Figure 2.16 (Wave 2), respectively. The labels A and B on (e) indicate the averaging period for the PSD shown in Appendix A. The x-axis shows the date and time in UTC.
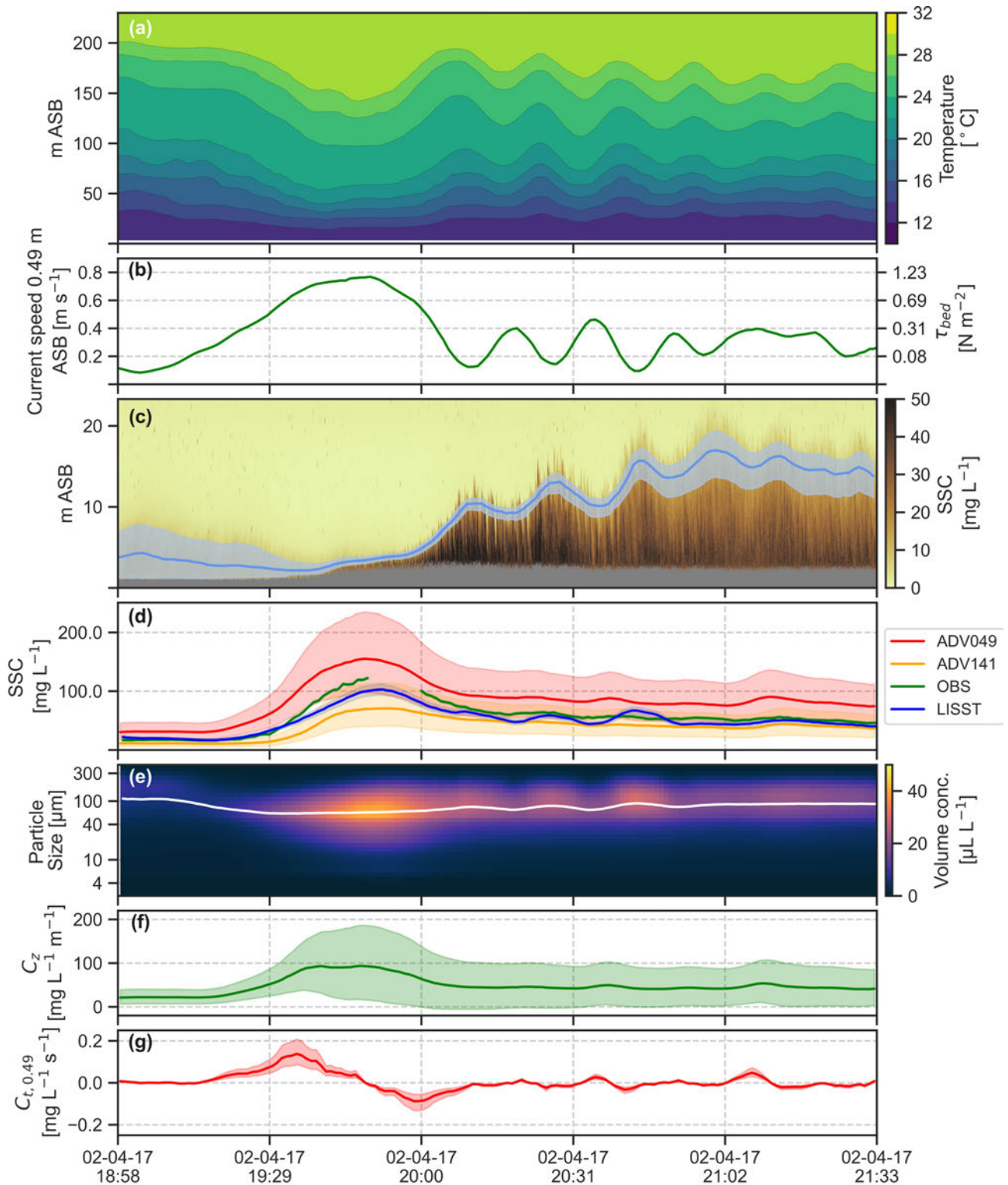
Figure 2.15: Wave 1 showing (a) through-water-column temperature from mooring SP250; (b) boxcar-filtered current speed measured at 0.49 m ASB (with conversion to bed stress on the right y-axis); (c) the 10 mg L^{-1} SSC isopleth mean (blue line) and 95% CI (blue shading) calculated using 1,000 samples of the boxcar-filtered ADCP data and shown over the high resolution (8 Hz) ADCP SSC mean estimate with grey areas indicating receiver saturation; (d) mean estimates of SSC with 95% CI shown as coloured shading, (e) LISST binned volume concentration data with mean diameter (white line), (f) the vertical gradient of SSC between the two ADV at 0.49 m and at 1.41 m ASB with 95% CI; and (g) the time-rate-of-change at the lower ADV with 95% CI. The x-axis shows the date and time in UTC.

Figure 2.16: Wave 2 showing (a) through-water-column temperature from mooring SP250; (b) boxcar-filtered current speed measured at 0.49 m ASB (with conversion to bed stress on the right y-axis); (c) the 10 mg L^{-1} SSC isopleth mean (blue line) and 95% CI (blue shading) calculated using 1,000 samples of the boxcar-filtered ADCP data and shown over the high resolution (8 Hz) ADCP SSC mean estimate with grey areas indicating receiver saturation; (d) mean estimates of SSC with 95% CI shown as coloured shading, (e) LISST binned volume concentration data with mean diameter (white line), (f) the vertical gradient of SSC between the two ADV at 0.49 m and at 1.41 m ASB with 95% CI; and (g) the time-rate-of-change at the lower ADV with 95% CI. The x-axis shows the date and time in UTC.

Figure 2.17: Comparison of estimated bed stress and the time-rate-of-change of SSC, C_t, at three different heights above sea bed during the first depression of Wave 1 (Figure 2.15) and covering the period 19:08 to 20:08. The arrows indicate the direc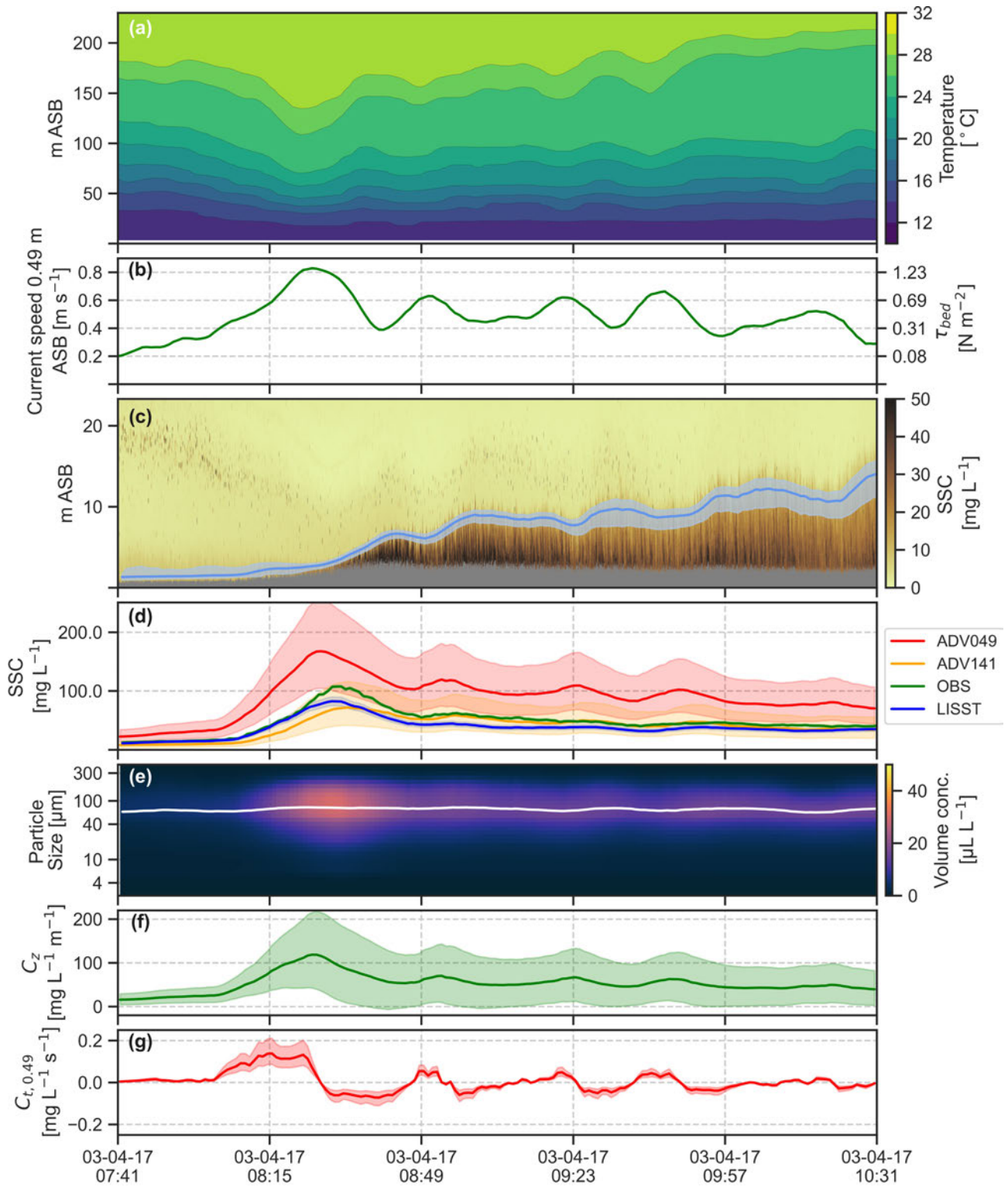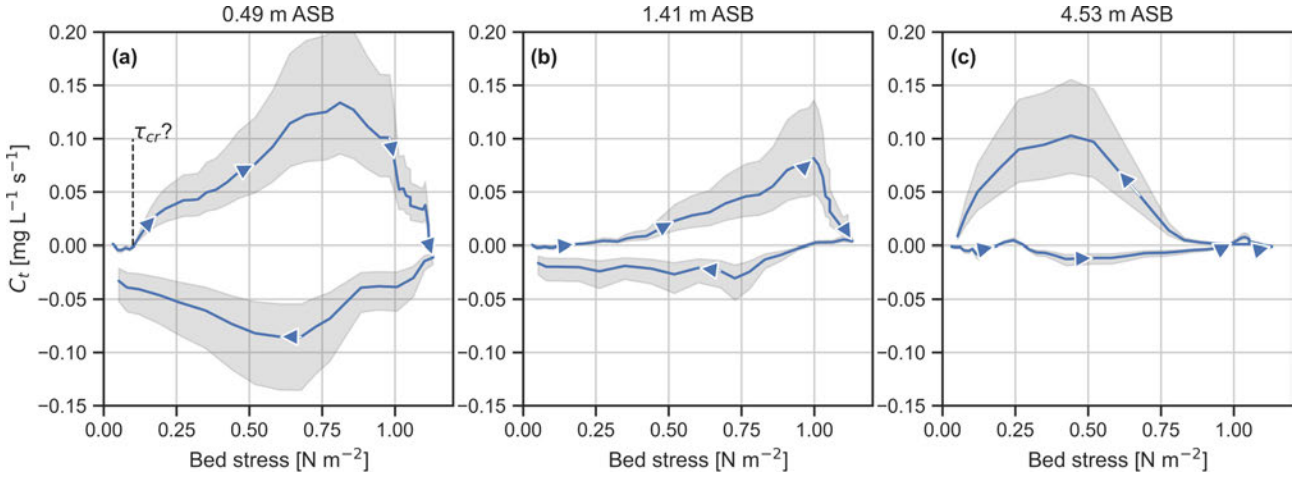tion of evolution and are spaced every ten minutes. The blue line represents the mean estimate of C_t and the shading represents the 95% CI. Estimates of C_t in subplots (a) and (b) are from each ADV and from the ADCP in subplot (c).

Not accounting for these processes would make any analysis of the erosion rate or τ_{cr} erroneous. Disentangling the contributions of these processes will require further analysis.

2.7   Conclusions and recommendations

We have estimated SSC at multiple heights above the sea bed under forcing by large amplitude NLIW and tidal forcing. We demonstrated from these measurements that further analysis of unsteady sediment dynamics will require dynamic modelling, and that direct linear regression between SSC and seabed stress is not suitable. The connected series of calibrations allowed for all instruments moored on the lander to be utilised to estimate SSC. We used Bayesian inference to estimate the SSC and connect the models with a full description of uncertainty. Two ground-truthed calibration methods, the *in-situ* and the *laboratory* methods, were utilised and compared.

The connected series of calibration models allowed for estimation of SSC from a suite of lander-based instruments. This made it straightforward to derive meaningful statements about the uncertainty of SSC from diverse instrument observations. It also allowed for tracking of uncertainty propagation through the connected models. The calibration of instrument data to SSC with uncertainty was a necessary part of SSC estimation which will allow for further analysis of sediment dynamics.

Calibration of the lander-based instruments deployed at 250 m depth was a challenging task. The favourable comparison of the two independent calibration methods, *in-situ* and *laboratory*, provides confidence in our final results. Neither method captured or replicated the actual conditions at around 1 m ASB and the potential presence of a particle population with a higher settling velocity may have resulted in an underestimate of SSC. We also demonstrated that conversion of acoustic data from log_{10} space to SSC was associated with a transformation of the model uncertainty. While mean estimates of SSC and derived quantities appeared to be valid, the results demonstrate it is essential to be aware of the range and distribution of uncertainty associated with any estimates.

The calibration method presented here appeared to be a suitable approach to quantifying SSC with uncertainty for continental shelf experiments. Despite some limitations, we believe the method is robust and has wide applicability to any bottom-lander style study deployed at significant depths, where other methods may not be feasible (noting that the vertical arrangement of instruments would be objective and site specific). For researchers pursuing a similar strategy, we would recommend direct calibration of all relevant instruments (if feasible) using the *in-situ* method to provide multiple independent estimates of SSC. Modification of the profiling frame to allow for water sampling closer to the bed would also be beneficial. Finally, placement of instruments along the ADCP profile may improve SSC estimates further from the bed.

We observed numerous resuspension events over the period 2 to 16 April, 2017. During this time, NLIW were associated with the highest bed stress and SSC estimates. Sediment resuspension under the NLIW was restricted to the bottom mixing layer which was capped by a region of strong vertical sediment gradients of up to 40 mg L^{-1} m^{-1}. After the NLIW passed, sediment could remain in suspension for up to 9 hours and could be advected horizontally and vertically by barotropic and baroclinic motion.

The positive correlation between bed stress and near-bed SSC estimates indicated that the primary mechanism of sediment resuspension is boundary-induced bed shear stress and associated vertical mixing. The bed stress to SSC correlation decreased further from the bed, where vertical motions appeared to be an important consideration, but may only modulate the mixing-layer thickness, rather than have a significant net effect on vertical flux. The estimates of SSC presented in this work, as well as derived quantities such as the spatial and temporal gradients, are the first step towards a detailed analysis of the in-situ turbulent and advective sediment flux observations, and towards numerical modelling of C_t under NLIW.

Bibliography

P. Aghsaee, L. Boegman, P. J. Diamessis, and K. G. Lamb. Boundary-layer-separation-driven vortex shedding beneath internal solitary waves of depression. *Journal of Fluid Mechanics*, 690:321–344, 2012. ISSN 00221120. doi: 10.1017/jfm.2011.432.

Y. C. Agrawal and D. M. Hanes. The implications of laser-diffraction measurements of sediment size distributions in a river to the potential use of acoustic backscatter for sediment measurements. *Water Resources Research*, 51(11):8854–8867, 2015. doi: 10.1002/2015WR017268.

L. Boegman and M. Stastna. Sediment Resuspension and Transport by Internal Solitary Waves. *Annual Review of Fluid Mechanics*, 51(1):annurev–fluid–122316–045049, 2019. doi: 10.1146/annurev-fluid-122316-045049.

D. Bogucki, T. Dickey, and L. G. Redekopp. Sediment resuspension and mixing by resonantly generated internal solitary waves. *Journal of Physical Oceanography*, 27(7):1181–1196, 1997. doi: https://doi.org/10.1175/1520-0485(1997)027⟨1181:SRAMBR⟩2.0.CO;2.

J. Bonnin, H. Van Haren, P. Hosegood, and G. J. A. Brummer. Burst resuspension of seabed material at the foot of the continental slope in the Rockall Channel. *Marine Geology*, 226(3-4):167–184, 2006. doi: 10.1016/j.margeo.2005.11.006.

D. Bourgault, M. Morsilli, C. Richards, U. Neumeier, and D. E. Kelley. Sediment resuspension and nepheloid layers induced by long internal solitary waves shoaling orthogonally on uniform slopes. *Continental Shelf Research*, 72:21–33, 2014. ISSN 02784343. doi: 10.1016/j.csr.2013.10.019.

B. Butman, P. S. Alexander, A. Scotti, R. C. Beardsley, and S. P. Anderson. Large internal waves in Massachusetts Bay transport sediments offshore. *Continental Shelf Research*, 26(17-18):2029–2049, 2006. doi: 10.1016/j.csr.2006.07.022.

D. A. Cacchione and D. E. Drake. Nepheloid layers and internal waves over continental shelves and slopes. *Geo-Marine Letters*, 6(3):147–152, 1986. doi: 10.1007/BF02238085.

D. A. Cacchione, L. F. Pratson, A. S. Ogston, L. F. Pratson, and A. S. Ogston. The shaping of continental slope by internal tides. *Science*, 296(April):724, 2002. doi: 10.1126/science.1069803.

M. Carr, P. A. Davies, and P. Shivaram. Experimental evidence of internal solitary wave-induced global instability in shallow water benthic boundary layers. *Physics of Fluids*, 20(6), 2008. ISSN 10706631. doi: 10.1063/1.2931693.

BIBLIOGRAPHY

O. M. Cheriton, E. E. McPhee-Shaw, W. J. Shaw, T. P. Stanton, J. G. Bellingham, and C. D. Storlazzi. Suspended particulate layers and internal waves over the southern Monterey Bay continental shelf: An important control on shelf mud belts? *Journal of Geophysical Research: Oceans*, 119(1): 428–444, 2014. doi: 10.1002/2013JC009360.

J. H. Churchill, P. E. Biscaye, and F. Aikman. The character and motion of suspended particulate matter over the shelf edge and upper slope off Cape Cod. *Continental Shelf Research*, 8(5-7): 789–809, 1988. doi: 10.1016/0278-4343(88)90077-5.

K. Deines. Backscatter estimation using Broadband acoustic Doppler current profilers. *Proceedings of the IEEE Sixth Working Conference on Current Measurement (Cat. No.99CH36331)*, pages 249–253, 1999. doi: 10.1109/CCM.1999.755249.

P. J. Diamessis and L. G. Redekopp. Numerical Investigation of Solitary Internal Wave-Induced Global Instability in Shallow Water Benthic Boundary Layers. *Journal of Physical Oceanography*, 36(5): 784–812, 2006. ISSN 0022-3670. doi: 10.1175/JPO2900.1.

J. P. Downing and R. A. Beach. Laboratory apparatus for calibrating optical suspended solids sensors. *Marine Geology*, 86(2-3):243–249, 1989. ISSN 00253227. doi: 10.1016/0025-3227(89)90053-4.

D. C. Fugate and C. T. Friedrichs. Determining concentration and fall velocity of estuarine particle populations using adv, obs and lisst. *Continental Shelf Research*, 22(11-13):1867–1886, 2002. doi: 10.1016/S0278-4343(02)00043-2.

W. D. Gardner. Periodic resuspension in Baltimore Canyon by focusing of internal waves. *Journal of Geophysical Research*, 94(C12), 1989. doi: 10.1029/jc094ic12p18185.

W. D. Gardner, P. E. Biscaye, J. R. Zaneveld, and M. J. O. Richardson. Calibration and comparison of the LDGO Nephelometer and the OSU Transmissometer on the Nova Scotian Rise. *Marine Geology*, 66:323–344, 1985. doi: 10.1016/0025-3227(85)90037-4.

J. W. Gartner. Estimating suspended solids concentrations from backscatter intensity measured by acoustic Doppler current profiler in San Francisco Bay, California. *Marine Geology*, 211(3-4): 169–187, 2004. doi: 10.1016/j.margeo.2004.07.001.

A. Gelman, J. Carlin, H. Stern, D. Dunson, A. Vehtari, and D. Rubin. *Bayesian Data Analysis.* CRC Press, 3rd edition, 2013.

R. J. Gibbs and E. Wolanski. The effect of flocs on optical backscattering measurements of suspended material concentration. *Marine Geology*, 107(4):289–291, 1992. doi: 10.1016/0025-3227(92) 90078-V.

L. Gostiaux and H. van Haren. Extracting meaningful information from uncalibrated backscattered echo intensity data. *Journal of Atmospheric and Oceanic Technology*, 27(5):943–949, 2010. ISSN 07390572. doi: 10.1175/2009JTECHO704.1.

M. O. Green and J. D. Boon. The measurement of constituent concentrations in nonhomogeneous sediment suspensions using optical backscatter sensors. *Marine Geology*, 110(1-2):73–81, 1993. doi: 10.1016/0025-3227(93)90106-6.

R. H. Green, N. L. Jones, M. D. Rayson, R. J. Lowe, C. E. Bluteau, and G. N. Ivey. Nutrient fluxes into an isolated coral reef atoll by tidally driven internal bores. *Limnology and Oceanography*, 64 (2):461–473, 2019. ISSN 19395590. doi: 10.1002/lno.11051.

H. K. Ha, W.-Y. Hsu, J.-Y. Maa, Y. Shao, and C. Holland. Using ADV backscatter strength for measuring suspended cohesive sediment concentration. *Continental Shelf Research*, 29(10): 1310–1316, 2009. doi: 10.1016/J.CSR.2009.03.001.

H. K. Ha, J. P. Maa, K. Park, and Y. H. Kim. Estimation of high-resolution sediment concentration profiles in bottom boundary layer using pulse-coherent acoustic Doppler current profilers. *Marine Geology*, 279(1-4):199–209, 2011. ISSN 00253227. doi: 10.1016/j.margeo.2010.11.002.

A. Hoitink and P. Hoekstra. Observations of suspended sediment from ADCP and OBS measurements in a mud-dominated environment. *Coastal Engineering*, 52(2):103–118, 2005. doi: 10.1016/J. COASTALENG.2004.09.005.

P. Hosegood, J. Bonnin, and H. van Haren. Solibore-induced sediment resuspension in the Faeroe-Shetland channel. *Geophysical Research Letters*, 31(9):2–5, 2004. doi: 10.1029/2004GL019544.

N. L. Jones, G. N. Ivey, M. D. Rayson, and S. M. Kelly. Mixing Driven by Breaking Nonlinear Internal Waves. *Geophysical Research Letters*, 47(19), 2020. doi: 10.1029/2020GL089591.

Y. Kim and G. Voulgaris. Estimation of supsended sediment concentration in estuarine environmetns using Acoustic Backscatter from an ADCP. *Proceedings of the Coastal Sediment 03*, pages 1–10, 2003.

J. M. Klymak and J. N. Moum. Internal solitary waves of elevation advancing on a shoaling shelf. *Geophysical Research Letters*, 30(20), 2003. doi: 10.1029/2003GL017706.

R. B. Krone. The significance of aggregate properties to the transport process. *Estuarine Cohesive Sediment Dynamics: Proceedings of a Workshop on Cohesive Sediment Dynamics with Special Reference to Physical Processes in Estuaries, Tampa, Florida, November 12–14, 1984*, pages 66–84, 1986. doi: 10.1007/978-1-4612-4936-8.

S. H. Leckie, S. Draper, D. J. White, L. Cheng, and A. Fogliani. Lifelong embedment and spanning of a pipeline on a mobile seabed. *Coastal Engineering*, 95:130–146, 2015. ISSN 03783839. doi: 10.1016/j.coastaleng.2014.10.003.

S. H. Leckie, H. Mohr, S. Draper, D. L. McLean, D. J. White, and L. Cheng. Sedimentation-induced burial of subsea pipelines: Observations from field data and laboratory experiments. *Coastal Engineering*, 114:137–158, 2016. ISSN 03783839. doi: 10.1016/j.coastaleng.2016.04.017.

K. A. Ludwig and D. M. Hanes. A laboratory evaluation of optical backscatterance suspended solids sensors exposed to sand-mud mixtures. *Marine Geology*, 94(1-2):173–179, 1990. doi: 10.1016/0025-3227(90)90111-V.

I. T. MacDonald, C. E. Vincent, P. D. Thorne, and B. D. Moate. Acoustic scattering from a suspension of flocculated sediments. *Journal of Geophysical Research: Oceans*, 118(5):2581–2594, 2013. doi: 10.1002/jgrc.20197.

A. Manderson, M. D. Rayson, E. Cripps, M. Girolami, J. P. Gosling, M. Hodkiewicz, G. N. Ivey, and N. L. Jones. Uncertainty quantification of density and stratification estimates with implications for predicting ocean dynamics. *Journal of Atmospheric and Oceanic Technology*, 36(8):1313–1330, 2019. doi: 10.1175/JTECH-D-18-0200.1.

J. Martín, P. Puig, A. Palanques, and M. Ribó. Trawling-induced daily sediment resuspension in the flank of a Mediterranean submarine canyon. *Deep-Sea Research Part II: Topical Studies in Oceanography*, 104:174–183, 2014. ISSN 09670645. doi: 10.1016/j.dsr2.2013.05.036.

E. Masunaga, H. Homma, H. Yamazaki, O. B. Fringer, T. Nagai, Y. Kitade, and A. Okayasu. Mixing and sediment resuspension associated with internal bores in a shallow bay. *Continental Shelf Research*, 110:85–99, 2015. ISSN 18736955. doi: 10.1016/j.csr.2015.09.022.

E. Masunaga, R. S. Arthur, O. B. Fringer, and H. Yamazaki. Sediment resuspension and the generation of intermediate nepheloid layers by shoaling internal bores. *Journal of Marine Systems*, 170:31–41, 2017. ISSN 09247963. doi: 10.1016/j.jmarsys.2017.01.017.

E. E. McPhee-Shaw, R. W. Sternberg, B. Mullenbach, and A. S. Ogston. Observations of intermediate nepheloid layers on the northern California continental margin. *Continental Shelf Research*, 24(6): 693–720, 2004. doi: 10.1016/j.csr.2004.01.004.

O. A. Mikkelsen and M. Pejrup. The use of a LISST-100 laser particle sizer for in-situ estimates of floc size, density and settling velocity. *Geo-Marine Letters*, 20(4):187–195, 2001. doi: 10.1007/s003670100064.

O. A. Mikkelsen, P. S. Hill, T. G. Milligan, and R. J. Chant. In situ particle size distributions and volume concentrations from a LISST-100 laser particle sizer and a digital floc camera. *Continental Shelf Research*, 25(16):1959–1978, 2005. doi: 10.1016/J.CSR.2005.07.001.

J. N. Moum, D. R. Caldwell, J. D. Nash, and G. D. Gunderson. Observations of Boundary Mixing over the Continental Slope. *Journal of Physical Oceanography*, 32(7):2113–2130, 2002. doi: 10.1175/1520-0485(2002)032⟨2113:OOBMOT⟩2.0.CO;2.

M. A. Noble and J. P. Xu. Observations of large-amplitude cross-shore internal bores near the shelf break, Santa Monica Bay, CA. *Marine Environmental Research*, 56(1-2):127–149, 2003. doi: 10.1016/S0141-1136(02)00328-8.

P. Puig, A. Palanques, and J. Guillén. Near-bottom suspended sediment variability caused by storms and near-inertial internal waves on the Ebro mid continental shelf (NW Mediterranean). *Marine Geology*, 178(1-4):81–93, 2001. doi: 10.1016/S0025-3227(01)00186-4.

L. S. Quaresma, V. J., Oliveira A., S. J., J. Vitorino, A. Oliveira, and J. da Silva. Evidence of sediment resuspension by nonlinear internal waves on the western Portuguese mid-shelf. *Marine Geology*, 246(2-4):21, 2007. doi: 10.1016/j.margeo.2007.04.019.

M. D. Rayson, N. L. Jones, and G. N. Ivey. Observations of Large-Amplitude Mode-2 Nonlinear Internal Waves on the Australian North West Shelf. *Journal of Physical Oceanography*, 49(January 2019):309–329, 2019. doi: 10.1175/JPO-D-18-0097.1.

M. Ribó, P. Puig, and H. van Haren. Hydrodynamics over the Gulf of Valencia continental slope and their role in sediment transport. *Deep-Sea Research Part I: Oceanographic Research Papers*, 95: 54–66, 2015. ISSN 09670637. doi: 10.1016/j.dsr.2014.10.004.

J. Salvatier, T. V. Wiecki, and C. Fonnesbeck. Probabilistic programming in Python using PyMC3. *PeerJ Computer Science*, 2016(4):1–24, 2016. doi: 10.7717/peerj-cs.55.

H. Sandstrom and J. A. Elliott. Internal Tide and Solitons on the Scotian Shelf: a Nutrient Pump At Work. *Journal of Geophysical Research*, 89(C4):6415–6426, 1984. doi: 10.1029/JC089iC04p06415.

M. G. Sassi, A. J. Hoitink, and B. Vermeulen. Impact of sound attenuation by suspended sediment on ADCP backscatter calibrations. *Water Resources Research*, 48(9):1–14, 2012. ISSN 00431397. doi: 10.1029/2012WR012008.

M. L. Schmelter, M. B. Hooten, and D. K. Stevens. Bayesian sediment transport model for unisize bed load. *Water Resources Research*, 47(11):1–15, 2011. doi: 10.1029/2011WR010754.

P. D. Thorne and D. Hurther. An overview on the use of backscattered sound for measuring suspended particle size and concentration profiles in non-cohesive inorganic sediment transport studies. *Continental Shelf Research*, 73:97–118, 2014. doi: 10.1016/j.csr.2013.10.017.

Z. Tian, Y. Jia, S. Zhang, X. Zhang, Y. Li, and X. Guo. Bottom and Intermediate Nepheloid Layer Induced by Shoaling Internal Solitary Waves: Impacts of the Angle of the Wave Group Velocity Vector and Slope Gradients. *Journal of Geophysical Research: Oceans*, 124(8):5686–5699, 2019. ISSN 21699291. doi: 10.1029/2018JC014721.

R. Valipour, L. Boegman, D. Bouffard, and Y. R. Rao. Sediment resuspension mechanisms and their contributions to high-turbidity events in a large lake. *Limnology and Oceanography*, 62(3): 1045–1065, 2017. doi: 10.1002/lno.10485.

J. G. Venditti, M. Church, M. E. Attard, and D. Haught. Use of ADCPs for suspended sediment transport monitoring: An empirical approach. *Water Resources Research*, 52(4):2715–2736, 2016. doi: 10.1002/2015WR017348.Received.

Y. H. Wang, C. F. Dai, and Y. Y. Chen. Physical and ecological processes of internal waves on an isolated reef ecosystem in the South China Sea. *Geophysical Research Letters*, 34(18):1–7, 2007. ISSN 00948276. doi: 10.1029/2007GL030658.

E. D. Zaron. Baroclinic tidal sea level from exact-repeat mission altimetry. *Journal of Physical Oceanography*, 49(1):193–210, 2019. doi: 10.1175/JPO-D-18-0127.1.

W. G. Zhang, Z. Cheng, and A. D. Ashton. Exploring the Potential for Internal Tides to Reshape the Continental Shelf Edge Seafloor. *Progress in Oceanography*, 195(April):102575, 2021. ISSN 00796611. doi: 10.1016/j.pocean.2021.102575.

A. Zulberti, G. N. Ivey, and N. L. Jones. Observations of Near-bed Stress beneath Nonlinear Internal Wave Trains in the Ocean. *21st Australasian Fluid Mechanics Conference*, (December):13–16, 2018.

A. Zulberti, N. L. Jones, and G. N. Ivey. Observations of Enhanced Sediment Transport by Nonlinear Internal Waves. *Geophysical Research Letters*, 47(19):1–11, 2020. doi: 10.1029/2020GL088499.

Chapter 3

Characterisation of suspended sediment dynamics under nonlinear internal waves

ABSTRACT

The mechanisms driving suspended sediment dynamics during the propagation of nonlinear internal waves remain speculative. While internal waves are continuously generated and dissipated on oceanic continental shelves, there are few studies that capture their role in driving sediment resuspension above the seabed. Here we present observations of suspended sediment dynamics during the propagation of large-amplitude nonlinear internal waves over a shelf and estimate the contribution of key terms in the advection-diffusion equation. This analysis was performed for two events; a large amplitude nonlinear internal wave of depression, and a solibore (an internal bore with wave-like oscillations). The wave of depression had an estimated speed of 0.6 m s^{-1}, an amplitude of 50 m, and a leading horizontal length of 850 m. The solibore had an estimated speed of 0.52 m s^{-1}, an amplitude of 40 m, and a leading turbid trapped core with a length of approximately 80 m. During both events, near-bed suspended sediment concentration (0.35 m above bed) reached a maximum of around 100 g m^{-3} and the Reynolds flux and vertical advection terms reached ± 0.2 g m^{-3} s^{-1} (between 2 and 8 m above bed). During the wave of depression, the horizontal advection term reached ± 0.07 g m^{-3} s^{-1} and during the solibore it reached ± 2.2 g m^{-3} s^{-1} (between 2 and 8 m above bed). The sum of the estimated terms were in good agreement with the observed time-rate-of-change of suspended sediment concentration.

3.1 Introduction

Energetic nonlinear internal waves (NLIW aka. solitons) have been known for decades to resuspend and transport sediment from the seafloor [Churchill et al., 1988; Gardner, 1989]. The detailed mechanisms underlying this resuspension by internal waves are, however, still the subject of ongoing research. In a recent review of the topic, Boegman and Stastna [2019] stated that *'the dynamics of NLIW–sediment interaction remained speculative'*. The authors went on to state the issue was confounded by *'a paucity*

of field observations, particularly those that measure bottom stress and sediment profiles through the water column'. We address this issue here by using high resolution observations of current velocity and suspended sediment concentration, collected over the bottom 8 m, to estimate the different contributions to observed suspended sediment concentration. We perform this analysis under two diverse but representative NLIW events - a NLIW of depression and a solibore.

A robust analysis of suspended sediment dynamics under NLIW is required in order to understand and predict sedimentary processes on continental shelves. Observations collected in-situ are an essential step towards modelling and parameterising these processes for inclusion in broader scale studies. A key motivation for improving our understanding and estimation of suspended sediment concentration (herein C) on continental shelves is the increased development pressure in these areas. Assets such as submarine cables, pipelines and drilling operations, and offshore footings or anchors all require installation, monitoring, and maintenance, generally performed by remotely operated vehicles that cannot operate adequately in turbid water. In addition, better understanding of aperiodic sediment fluxes under NLIW forcing will inform long-term continental shelf evolution.

Previous research into resuspension under NLIW has been performed using three approaches: numerical, laboratory, and field observation experiments, each with its own advantages and disadvantages. Boegman and Stastna [2019] noted that NLIW of depression and internal bore-like features are usually not well resolved in field-scale numerical models. They also noted that, due to the much smaller flow Reynolds number in the laboratory (i.e., greater importance of viscous terms), laboratory experiments can potentially be controlled by processes not typically observed in the field. Finally, Boegman and Stastna [2019] recognised that sparse field observations are unable to capture the important spatial scales of what is an inherently 3D process.

Despite these challenges all three approaches have made significant contributions to understanding NLIW dynamics and their interaction with the bottom boundary. In the field, Bogucki et al. [1997] observed NLIW of depression propagating upstream (into the tidal current) and hypothesised vertical velocities, from a global instability generated near the sea bed, were important for sediment resuspension. Johnson et al. [2001] observed an increase in optical beam attenuation in the lee of a NLIW of depression propagating with the tide and suggested a similar mechanism to that of Bogucki et al. [1997] might be responsible. Diamessis and Redekopp [2006] used numerical analysis to demonstrate that such instabilities were possible under waves of depression with Reynolds wave numbers up to 10^4. Aghsaee and Boegman [2015] used laboratory experiments to show that resuspension was greatest in the lee of a NLIW of depression, coincident with bursts of fluid with positive vertical velocity.

Recently Zulberti et al. [2020] observed large amplitude NLIW of depression in the field propagating into the tidal current, but did not observe a global instability. These field observations were characterised by high Reynolds numbers ($\sim 10^8$) and the authors hypothesised that energetic turbulent stirring processes were able to destroy coherent structures before they could grow. In Chapter 2, we assessed C under the same waves and showed that when measured close to the bed C was proportional to the bed stress. However, as the observation point of C moved higher above the bed, the timing of increasing C was poorly predicted by bed stress, suggesting that measurement height is an important factor in how observations are interpreted.

Hosegood et al. [2004] observed shoaling bore-like waves moving upslope that were preceded by

a jet of positive vertical velocity. They hypothesised that this jet facilitated sediment resuspension during such events. Klymak and Moum [2003] and Moum et al. [2007] observed shoaling density fronts and wave packets of elevation advancing up the continental slope. The waves were associated with high turbidity in the boundary layer and elevated backscatter was observed for a small region within the center of the wave perturbation attached to the bed. Richards et al. [2013] observed similar high frequency wave packets from shoaling NLIW with strong vertical jets of current immediately preceding several cores with elevated backscatter. Masunaga et al. [2015] observed the same phenomena and also suggested that the leading jet was a key mechanism for resuspension during these events. Bourgault et al. [2014] and Masunaga et al. [2017] were able to qualitatively replicate the observations of Richards et al. [2013] Masunaga et al. [2015], respectively, using 2D Reynolds-averaged Navier-Stokes (RANS) numerical simulations.

Aghsaee et al. [2010], Xu and Stastna [2020], and Hartharn-Evans et al. [2022] used high resolution numerical simulations and varied key parameters to investigate the breaking and fission of a wave of depression into a train of waves of elevation. Ghassemi et al. [2022] replicated this fission process in the laboratory and in further work observed resuspension and shore-ward transport within the core of the resulting elevation wave pulses [Ghassemi, 2022]. Jones et al. [2020] showed that several different breaking mechanisms were possible, suggesting that different waves may be difficult to compare directly, despite some apparent similarities. These studies, however, did not have measurements or estimates of the suspended sediment concentration available (only proxy measurements) and thus were unable to quantify the instantaneous sediment fluxes driving changes in the concentration.

In this study we have directly assessed the in-situ contributions to observed suspended sediment concentration for two contrasting NLIW examples recorded at an energetic site on Australia's Northwest Shelf (NWS). The first wave type was a large amplitude NLIW of depression. The second wave type was what is commonly called a solibore - a wave that has both bore and wave-like features [Henyey, 1997] - which may be a late stage of mode-1 or mode-2 NLIW as they move into shallow water [Ghassemi et al., 2022]. The observations used an upward-looking acoustic Doppler current profiler (ADCP) configured to collect continuous high temporal and spatial (vertical) resolution measurements of the current velocity and acoustic backscatter over the bottom 8 meters.

We used this high resolution data set to estimate the contribution of the different terms in the advection-diffusion equation (ADE) to observed changes in C. We assume fully turbulent two-dimensional flow with x as the streamwise dimension and z the vertical direction. The ADE can thus be written

$$\frac{\partial C}{\partial t} = -W\frac{\partial C}{\partial z} - U\frac{\partial C}{\partial x} + \frac{\partial \overline{w'c'}}{\partial z}. \tag{3.1}$$

The left-hand side of the equation is the time-rate-of-change of the tracer, C. The right-hand side shows the terms estimated from observations in the analysis in this paper. The first term is the advection of the mean vertical concentration gradient, herein vertical advection, $\overline{W}.\overline{C}_z$. Note that we assume the acoustic measurements of vertical velocity already contain the effect of gravity, i.e., $\overline{W} = \overline{W}_{actual} - w_s$, where w_s is the mean settling velocity. The second term is the advection of the mean horizontal concentration gradient, herein horizontal advection, $\overline{U}.\overline{C}_x$. The third term is the vertical divergence of the vertical turbulent flux, herein Reynolds flux, $\overline{w'c'}_z$ (shown as $\langle w'c'\rangle_z$ in figures for clarity). Note that subscripts indicate a derivative of a quantity along the dimension indicated in the subscript.

In this paper we first describe the field experiment, mooring configurations, and the regional oceanographic setting. Then we describe the data processing and analysis methods used in this work. Next, we give a brief summary of the experiment site dynamics that provide context to the NLIW events. Finally, we assess the two types of wave events separately, beginning with a description of the wave and the data used, then a presentation and discussion of the results, the estimated contributions of each term in Equation 3.1.

3.2 Site and experiment description

Observations presented in this paper were captured as part of a 2019 field experiment undertaken in the Roebuck Basin on Australia's NWS around 30 km Southeast of Imperieuse Reef, the southernmost atoll of the Rowley Shoals [Figure 3.1]. Moorings were deployed for 50 days from 5 March to 24 April, 2019, however, for the analysis presented in this paper we have focused on a 15-day period from 10 to 25 March, 2019. Gong [2021] identified numerous local bathymetric features of near-critical or supercritical bottom slope in the region as potential internal wave generation sites. This included the shelf break at 500 to 600 m depth northwest of the Rowley Shoals, the pelagic ridge at 150 m depth, and the Shoals themselves, which rise abruptly from around 400 m depth to the surface. As well as these local generation sites, remotely-generated low-mode internal tides propagate with little energy loss towards the study site from Indonesia [Gong, 2021].

The tide in the region is macrotidal and semidiurnal with a tidal range greater than 4 m during spring tides. The region is also prone to intense tropical cyclones (TC) that can influence the local oceanographic conditions. *TC Veronica* passed northwest of the site, reaching within 150 km of the moorings on the 21 March, 2022. Any mean and seasonal (*Holloway*) currents are both generally expected to flow Southwest (along shelf) during the experiment months [Bahmanpour et al., 2016], although their magnitude is expected to be small in comparison to barotropic and baroclinic currents due to surface tides and internal waves, respectively.

We deployed three through-water-column (TWC) moorings in a cross-shelf array at 330 m, 200 m, and 150 m water depth (herein T_{330}, T_{200}, T_{150}) [Figure 3.1]. A bottom lander frame (herein L_{150}) was also deployed at 150 m depth, approximately 100 m Southwest (along shelf) of T_{150}. This study focused on the two moorings deployed at 150 m depth. Mooring T_{150} (119.17°E, 18.01°S) was configured with thermistors sampling at 1 Hz, with a vertical spacing of 2 m from 5 to 25 metres above sea bed (m ASB) and a spacing of 10 m from 30 to 130 m ASB. Temperature data from T_{150} was corrected for mooring knockdown using pressure sensors deployed at 30, 65, and 130 m ASB. A 150 kHz acoustic Doppler current profiler (ADCP, Teledyne RDI) was deployed on T_{150} near the sea bed looking up. This ADCP was configured to record at 2 m vertical intervals from 6.4 to 150.4 m ASB every 60 seconds. Four optical backscatter (OBS) instruments were placed on T_{150} at 3, 7, 12.6, and 25 m ASB.

We deployed the lander, L_{150}, to investigate the bottom boundary layer dynamics in detail. This mooring has been successfully deployed before, albeit with a slightly different instrument configuration (see Chapter 2 for a schematic). For this experiment, an upwards-looking 1 MHz ADCP (Nortek Signature) was configured to sample vertically from 0.43 to 8.02 m ASB at 0.03 m resolution and temporally at 4 Hz. This ADCP had a vertically oriented fifth beam (as described in Chapter 2) that provided a second estimate of vertical velocity (sampling as per the other beams). Two OBS
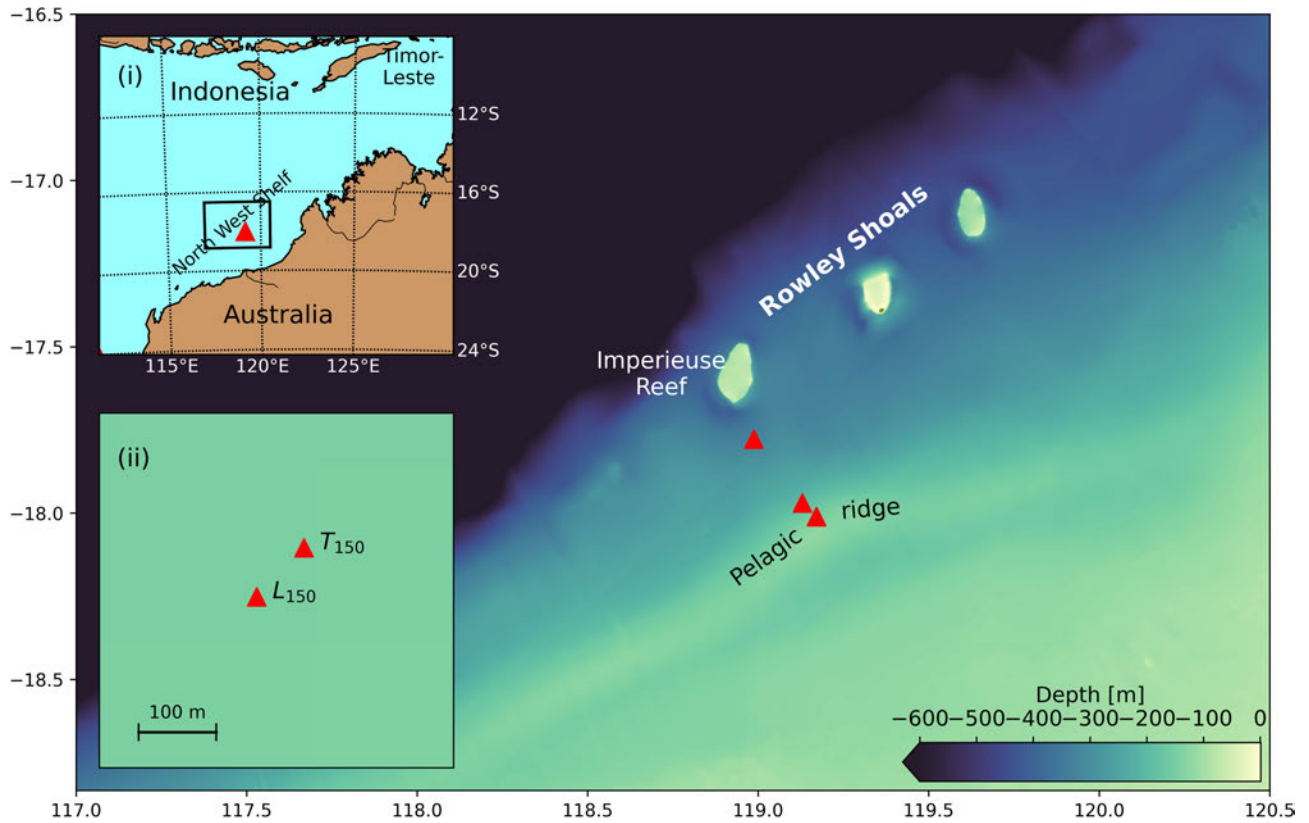
Figure 3.1: Field experiment location on the NWS of Australia with the T_{330}, T_{200}, and T_{150} moorings shown as red triangles and transect as an orange line. (i) Regional location within the Indian Ocean showing Indonesia, a potential internal wave generation zone. (ii) Configuration of the two moorings (T_{150} and L_{150}) at the 150 m isobath.

instruments were attached to L_{150} at 0.35 and 1.21 m ASB that measured turbidity at 90 s intervals. A third OBS attached to the lander recovery string at 4 m ASB returned bad data for the duration of the experiment. Several thermistors were also attached to the frame at different heights ASB, sampling at 1 Hz.

Vertical profiling using a CTD-Rosette was undertaken from the *RV Solander* during the recovery trip to perform the in-situ sediment calibration. After recovery, the OBS instruments were cleaned and attached to the profiling frame and programmed to sample at 2 Hz. Profiling was conducted repeatedly over the L_{150} location until 35 Niskin bottle samples had been collected. Bottle samples were vacuum-filtered onboard and transported back to land to be dried and weighed. A sediment sample was collected from the sea bed with a Smith McIntyre grab, which indicated a mean diameter of 33 µm, with approximately 17% of particles below 4 µm and 13% of particles above 125 µm by volume. Small shell fragments were observed in the grab sample.

3.3 Methods

3.3.1 ADCP data processing

The 1 MHz ADCP deployed on L_{150} was processed to estimate 3D current velocity data (East, North, Up) and corrected acoustic backscatter. First, current observations with low coherence between beams was flagged and removed from the data set. Spikes were then removed using the method described by Goring and Nikora [2002]. The current velocity data and uncorrected backscatter were divided into blocks (300 s blocks for the NLIW of depression, and 120 s blocks for the solibore), each block was linearly detrended, and then any spikes were removed and replaced by linear interpolation. This process was done row-by-row over all vertical bins for each event. The velocity data still contained some spikes that appeared to be correlated with both low and high echo intensity (i.e., near the instrument limits of operation). These spikes appeared to be normally distributed with a zero mean and so their inclusion in the boxcar-filtered mean data ($\overline{U}$ and $\overline{W}$) was considered acceptable.

For the turbulent vertical velocities (w') additional data processing was performed. Turbulent vertical velocities used herein were obtained from the vertically oriented fifth beam, as these single beam observations were less prone to spikes. Spikes were removed over three separate iterations using the method of Goring and Nikora [2002], with all modified data being removed after the complete data set had been processed. Missing data was then replaced using 2D interpolation.

Uncorrected ADCP backscatter from each beam was converted to relative backscatter using the method described by Gartner [2004], including the near-field correction. The conversion to relative backscatter also included the correction by Gostiaux and van Haren [2010] to remove the noise level in arithmetic space. The conversion assumed a constant volume backscattering strength and did not include any estimate of attenuation by suspended sediment. Temperature data from the thermistors on the lander mooring were used to calculate variable water attenuation both vertically and temporally (assuming a constant salinity and pressure).
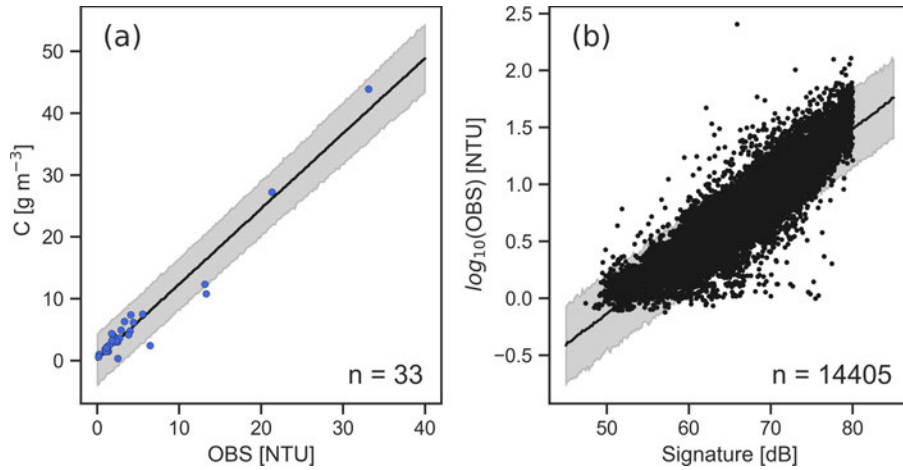
Figure 3.2: (a) In-situ calibration of one OBS instrument using suspended sediment concentration (C) measurements from 33 Niskin bottle samples (2/35 discarded). (b) Calibration of the L_{150} ADCP corrected backscatter against an OBS instrument at 1.21 m ASB.

3.3.2 Calibration

All seven OBS instruments were calibrated against suspended sediment concentration, C, using the laboratory method described in Chapter 2 (not shown). Three of the OBS instruments were attached to the *RV Solander* profiling frame and calibrated using the *in-situ* method [one example shown in Figure 3.2a] (also described in Chapter 2). Comparison of the methods showed a consistent difference in the slope parameter between the laboratory and in-situ methods for a given OBS instrument, with the in-situ slopes being consistently lower by a factor of approximately 2.33. This was likely due to the breakup of any flocs by the recirculation mechanism in the laboratory calibration tank, which has been shown to increase optical backscatter [Gibbs and Wolanski, 1992]. As a consequence, only OBS data that used the *in-situ* calibration method is presented in the results below.

Relative backscatter from the L_{150} ADCP was calibrated against C as per Chapter 2. Backscatter averaged over three vertical bins (9 cm) was extracted at the height of the lander OBS at 1.21 m ASB. Bayesian linear regression was performed on the base-10 logarithm of the OBS data against the ADCP relative backscatter [Figure 3.2b]. This calibration model was connected to the in-situ calibration model for the OBS [Figure 3.2a], providing an estimate of C for the ADCP (see Chapter 2 for more details). This calibration method included full uncertainty quantification on C which has been propagated through both calibration models. The uncertainty resulting from the calibration process has also been propagated to all quantities derived from C in results presented below.

3.3.3 Wave characterisation

NLIW of depression amplitude was estimated as the maximum downwards displacement of the mid-water isotherm over the initial depression. Wavelength was estimated from the time between peaks in the mid-water isotherm, converted to a length scale using the estimated wave speed. The NLIW of depression wave speed, c_{wave}, was calculated by modal fitting of the vertical density structure to estimate the mode-1 linear phase speed [as per Rayson et al., 2011].

Solibore wave speed, c_{wave}, and direction, θ, were estimated simultaneously using the method

described by Scotti et al. [2005]. Relative backscatter from the four angled beams on the L_{150} ADCP were converted to C using the calibration models. A three-bin boxcar filter was then taken in the vertical direction centered on the estimation height. The method takes the beam position and phase-lag (calculated by cross-correlation of each beam pair) and calculates the difference between beam pair phase-lags and theoretical transport time over a range of different speeds and directions to find parameter values with the minimum error, and hence, most likely c_{wave} and θ. This process was repeated over each bin from 5.0 to 8.0 m ASB and the final c_{wave} and θ was taken as the estimate with the minimum error.

3.3.4 Reynolds decomposition

The processed velocity and C data from the L_{150} ADCP was decomposed into mean and turbulent components over a selected segment length (i.e., boxcar filter width). Note that the segment length differed between events due to the differing timescales involved. The mean component was calculated as the arithmetic mean of each segment and the turbulent component was calculated as the difference between instantaneous and the mean, after linear detrending. Mean quantities have herein been denoted as uppercase with an overbar (e.g., $\overline{U}$) and turbulent quantities have been denoted as lowercase primes (e.g., u'), such that $U = \overline{U} + u'$. The Reynolds flux was estimated as the instantaneous product of the turbulent vertical velocity and turbulent sediment concentration, averaged over each segment and denoted as $\overline{w'c'}$. Both quantities (w' and c') were derived from the vertically-oriented fifth ADCP beam.

In general, the segment length was chosen to be short to limit the inclusion of any high frequency internal wave processes in the Reynolds flux estimate. For the NLIW of depression, the segment length (boxcar filter width) was 300 s, calculated at intervals of 60 s (80% overlap). For the solibore, the segment length was 30 s calculated at intervals of 5 s (80% overlap). We note, however, that the relevant timescales of the solibores and large turbulent fluctuations were close. For these events the decomposition may be affected by the choice of segment length, but testing indicated that this sensitivity was small over a range of relevant choices (not shown).

3.3.5 Horizontal advection estimation

Observations of the time-rate-of-change $\overline{C}_t$ at a point can be converted from time to space using $\overline{C}_t = c_{wave}\overline{C}_x$, where c_{wave} is the wave speed. Thus the horizontal advection term in Equation 3.1 can be estimated as

$$\overline{U}.\overline{C}_x = \overline{U}\frac{\overline{C}_t}{c_{wave}}. \tag{3.2}$$

Note that the sign of the wave speed is important and should be consistent with the sign of U. A key assumption of this method is that the observed velocity field and resulting C_t is due in total to the propagating wave. Due to this we analysed a NLIW of depression that arrived at approximately slack tide and a bore with a wave speed approximately equal to the observed horizontal current speed.

3.4 Site dynamics

We have focused our analysis on the 15-day record from the 10 to 25 March, 2019 [Figure 3.3]. During this period all instruments of interest functioned as expected without noticeable fouling, with the exception of one OBS instrument that failed to record any data. The period begins shortly after the peak of a spring tidal cycle and ends shortly after the following spring tidal cycle. Measured current velocities exceeded 0.7 m s^{-1} during peak spring tides. Sediment resuspension was observed throughout the record [Figure 3.3d] with values of $\overline{C}$ exceeding 30 g m^{-3} at 0.35 m ASB every calendar day.

Several resuspension events appeared to be the result of a solibore propagating past the site. Such events were identified as having an abrupt and simultaneous increase in $\overline{C}$ over the bottom 8 m ASB. This change was coincident with a sharp change in near-bed current velocity and an abrupt (although usually small) change in temperature, all measured at L_{150}. These events were identified visually using L_{150} ADCP and temperature data [arrival times indicated in Figure 3.3]. These bore-like waves were always observed during the onshore phase of barotropic tidal flow, and could roughly be grouped by tidal phase as arriving when cross-shelf tidal acceleration was zero (with some variance) [Figure 3.4].

Nine NLIW of depression that resulted in sediment resuspension were clearly identified in the temperature record [Figure 3.3]. The magnitude of sediment resuspension was small for all but the largest of these events, and generally small in comparison to tidal and solibore-induced resuspension. The wave arrivals were grouped, arriving close to the transition from offshore to onshore tidal flow, when tidal acceleration was positive [Figure 3.4]. Their grouping with respect to the tidal phase was likely due to the waves being tidally generated. During the analysis period their arrival at the observation site with respect to the tidal phase was predictable. This arrival phase is a site specific characteristic, i.e., the tidal phasing of wave arrival would shift if the observation site was moved onshore or offshore in the direction of wave propagation.

Other resuspension events appeared to fluctuate with the tidal velocity. This mode of resuspension was the cause of peak $\overline{C}$ as measured close (0.35 m ASB) to the bed. During offshore tidal flow resuspension net vertical velocities were often negative and $\overline{C}$ measured at 12.6 m from the bed could be close to zero, while at the same time that $\overline{C}$ at 0.35 m ASB was reaching a maximum. The two modes of resuspension (solibore and tidal) appeared to be connected, with the greatest tidal resuspension occurring during offshore and downslope directed currents [Figure 3.3], immediately preceding the greatest bore-like resuspension moving upslope. The most energetic of these offshore-onshore resuspension cycles occurred over the three days starting 21 March, as *TC Veronica* passed the site, and may have been exacerbated by cyclonic modulation of the upper thermocline structure [e.g., Cheriton et al., 2021]. These tidal resuspension events may have been due to supercritical flow generated in the lee of the ridge line, however, these events were not the focus of this study.

In this paper we have analysed two resuspension events in detail: a large amplitude NLIW of depression that propagated past the 150 m moorings at 12:00 on 13 March; and a solibore that propagated past the 150 m moorings at around 11:40 on 22 March [Figure 3.3]. The events identified here are far from an exhaustive description of all activity at this site. A comprehensive analysis of the cross-shelf baroclinic dynamics and mixing for this experiment is the subject of an ongoing thesis by a colleague.
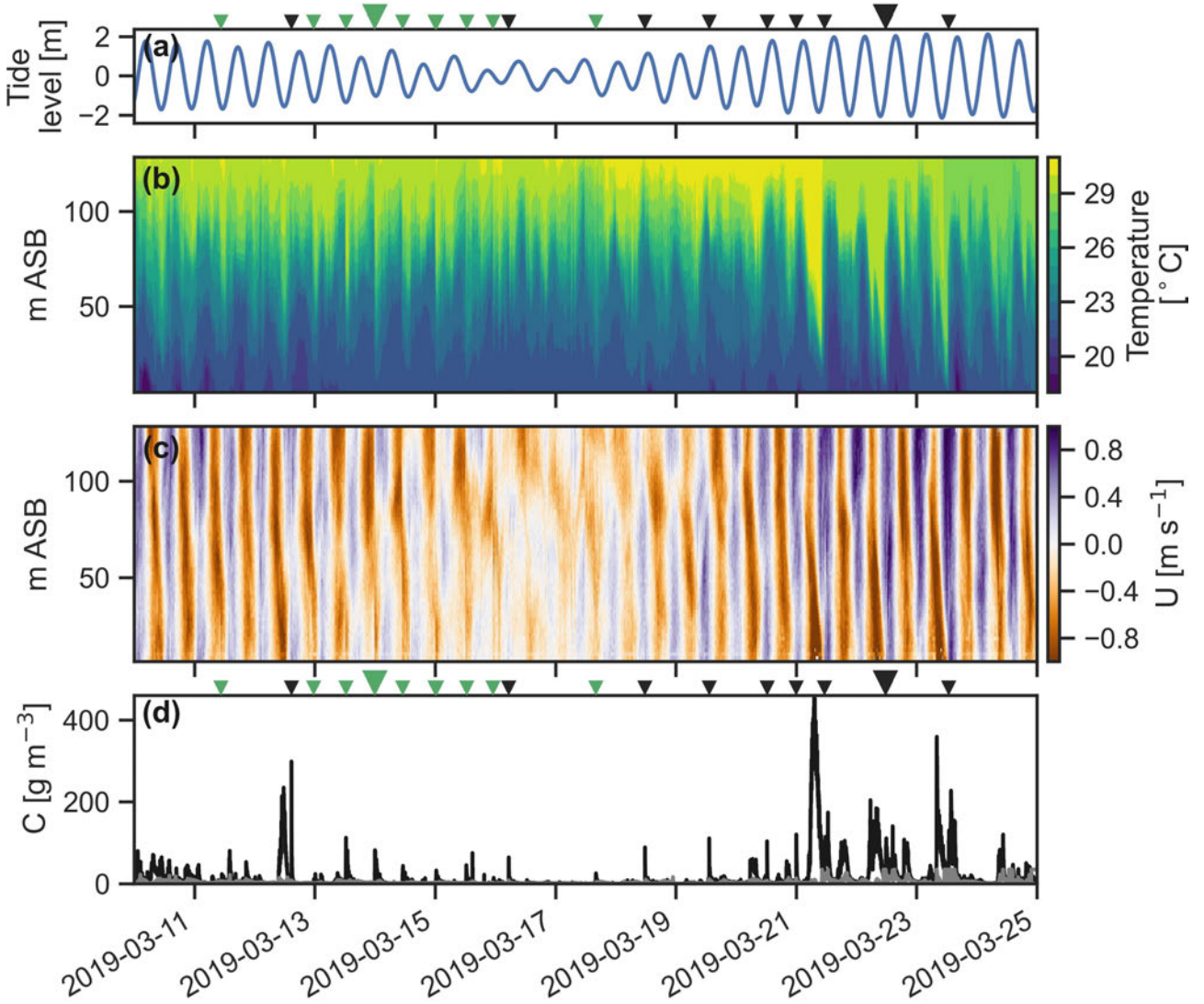
Figure 3.3: Experiment data over a 15-day period from 10 March, 2019, (a) Tide elevation predictions for the experiment site. (b) Temperature contours interpolated from T_{150} thermistor data. (c) T_{150} ADCP cross-shelf velocity, U (positive indicates onshore currents). (d) $\overline{C}$ estimates from an OBS at 0.35 m ASB (black) and an OBS at 12.6 m ASB (grey). Green and black triangles on the top and bottom plot indicate the arrival of a NLIW of depression or a solibore, respectively. The two events analysed in detail are indicated by larger triangle markers.
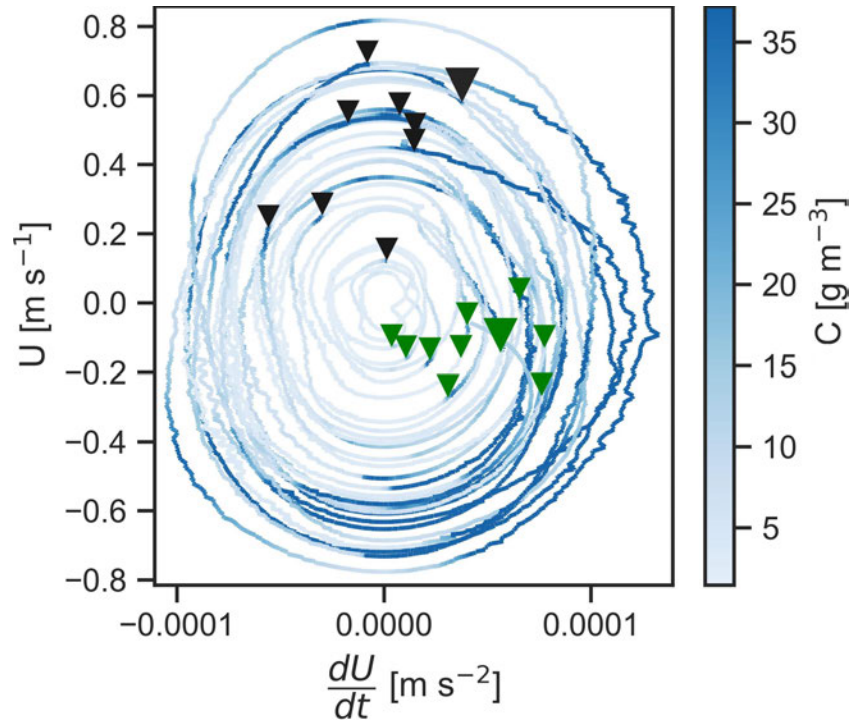
Figure 3.4: Low-pass filtered cross-shelf tidal acceleration (dU/dt) and cross-shelf tidal velocity (U) for the 15-day period from 10 March, 2019. Tides move counter-clockwise with larger tides producing larger circles. The line is coloured based on the estimated C from an OBS instrument deployed at 0.35 m ASB. Colouring is restricted to make low concentration events visible. The black and green triangles are the solibores and NLIW of depression, respectively, as shown in Figure 3.3. Downslope tidal flow (negative U, offshore) produced the greatest and longest sediment resuspension events that could continue into the upslope (onshore) tidal phase.
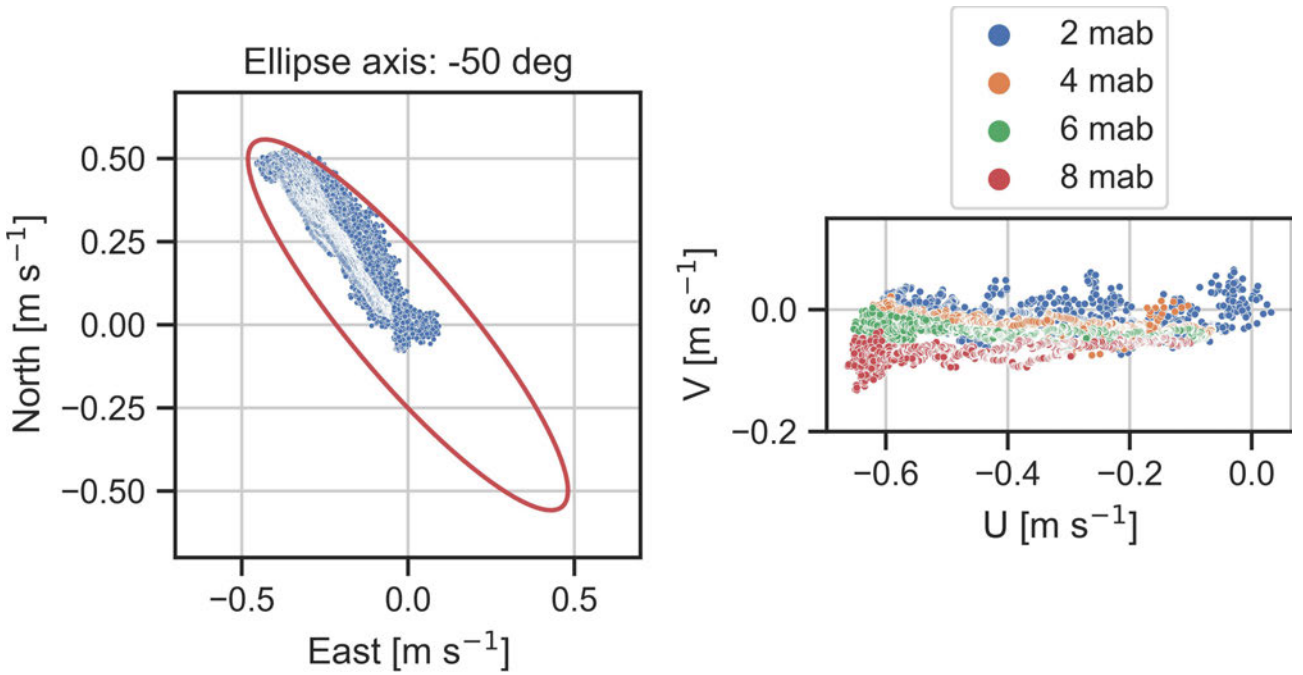
Figure 3.5: Left: Tidal ellipse (from all T_{150} ADCP data) and boxcar filtered currents under the leading depression of the NLIW. Right: Rotated currents at four different heights above the bed under the leading depression of the NLIW.

3.5 NLIW of depression

3.5.1 Wave description

A large NLIW of depression arrived at the 150 m isobath moorings at approximately 12:00 UTC on 13 March 2019. The wave was one of several identified during the 15-day analysis period. The wave had a mode-1 amplitude of ~50 m and a linear phase speed of 0.60 m s^{-1}. near-bed currents were directed offshore (Northwest) during the event [Figure 3.5]. ADCP horizontal currents were rotated to the principal (U-V) axis for the event bounds. Noticeable rotation of the horizontal currents as a function of height was observed during the leading depression [Figure 3.5].

Temperature data from T_{150} showed a wave train with a large u-shaped initial depression (approximately 850 m in length) followed by six depressions of increasing frequency. The initial wave arrived at around slack tide and the entire event lasted around 90 minutes. The initial u-shape is notable because it is reminiscent of the broader solitary waves predicted by the extended-Korteweg de Vries equation i.e., by including a cubic nonlinearity term [see e.g., Helfrich and Melville, 2006].

Mean cross-shelf current velocity measured at 5.0 m ASB reached approximately -0.5 m s^{-1} under the first three depressions, with peak $\overline{U}$ becoming smaller for each wave thereafter [Figure 3.6]. The wave arrived close to slack tide, with barotropic tidal currents increasing in the opposite direction to near-bed wave-induced currents during the event. Mean vertical velocities at 5 m ASB oscillated around ± 0.01 m s^{-1} for all waves in the train. Elevated C was observed at L_{150} by the ADCP and OBS instruments.

Below 4 m ASB, vertical velocities began to skew to be more in phase with cross-shelf velocities [Figure 3.6]. This may be the result of currents in this region straining to align with the bed, rather

than the direction of gravity, causing contamination of the gravity-aligned velocity profile. Estimation of fluxes was restricted to the region above 2 m ASB, but we note that vertical velocities may be inclined to skew negative close to 2 m ASB (i.e., the observations may over-estimate negative velocities and under-estimate positive velocities), due to the horizontal currents being directed offshore.

Reynolds decomposition for W revealed a complex turbulent environment in the second-half of the initial wave trough [Figure 3.7]. In addition, the vertical turbulent kinetic energy (TKE) was estimated as $\overline{w'w'}$ [Figure 3.7d]. It is clear that vertical TKE and C were elevated within the BBL, which was suppressed to $\mathcal{O}1\%$ of the total water column under the wave trough. As the wave trough passed, the BBL expanded and vertical TKE and C were observed to increase at the same time (when observed outside the bottom 1% of the water column). In this region both $\overline{U}$, and to a lessor extent $\overline{W}$, were leading indicators of C, as they were both out of phase with C. This is in agreement with laboratory observations of Aghsaee and Boegman [2015] who observed resuspension in the lee of the wave, coincident with bursts of positive W (i.e., w'), and field observations of Bluteau et al. [2016], who showed enhanced TKE was a better predictor of C above the log-layer. It is worth noting that in this case, with readily erodible sediment and a continuously turbulent boundary layer, the majority of the erosion is likely to occur under the accelerating flow and sediment is likely to be well-mixed through the BBL. This includes the period when the BBL is constrained close to the bed under the wave. In other words, this shouldn't be considered a transition from bed load to suspended transport as the wave passes, as may occur in laboratory experiments or environments with rapidly settling particles.

3.5.2   Flux estimates

The terms in Equation 3.1 were estimated using the L_{150} ADCP data. Reynolds flux, $\overline{w'c'}_z$, and vertical advection, $\overline{W}.\overline{C}_z$, were partitioned using Reynolds decomposition and the horizontal advection, $\overline{U}.\overline{C}_x$ was estimated as described previously. The results were compared to the observed C_t for the full event [Figure 3.8]. The instantaneous magnitudes of $\overline{W}.\overline{C}_z$ were comparable to $\overline{w'c'}_z$, and both were around three to four times larger than $\overline{U}.\overline{C}_x$, depending on the height above the bed. Instantaneous $\overline{U}.\overline{C}_x$ was always opposite to $\overline{W}.\overline{C}_z$. The magnitude of oscillations of $\overline{W}.\overline{C}_z$ was larger than C_t, but balanced by the opposing $\overline{U}.\overline{C}_x$. The sum of the three terms was generally in good agreement with the depth-integrated C_t [Figure 3.8e]. We believe that the primary reasons that the sum of the three terms occasionally drifted below the depth-integrated C_t were due to the inclusion of settling velocity in the acoustic measurements and contamination of the vertical velocities by the bottom slope, as described previously.

Under the leading wave trough the suspended sediment concentration was asymmetric and so were the estimated terms from Equation 3.1. For the rest of the waves in the train C was more symmetric over the bottom 8 m, as were the two advection terms. For this reason we divided the event into two sections, the initial wave, t_1 [up to 12:32 in Figure 3.8], and the rest of the wave train, t_2 [from 12:32 onward in Figure 3.8]. This is helpful because numerical and laboratory experiments often only simulate a single wave, which can be directly compared to the observations during t_1.

The integral of each term was calculated over time and also over both time and height for the analysis domain to provide an estimate of the net contribution to observed C_t during t_1 and t_2. During t_1 all the integrated terms were important contributors to C_t [Figure 3.9, blue lines and blue text],
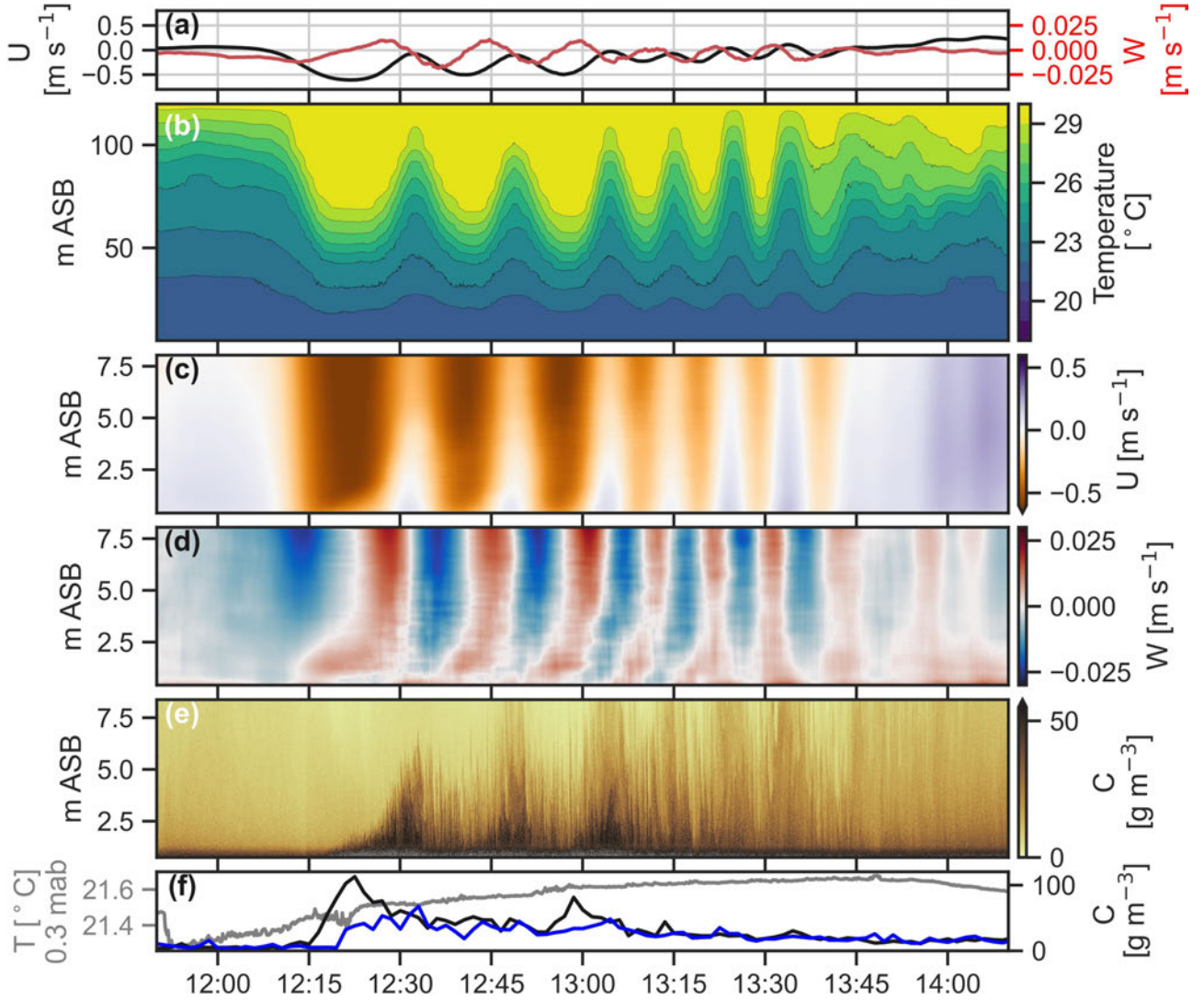
Figure 3.6: (a) Cross-shelf (left, black) and vertical (right, red) mean current velocity at 4.0 m ASB (boxcar-filtered with a 300 second window). (b) Temperature contours from the through-water-column mooring T_{150}. (c) Mean cross-shelf current velocity from the L_{150} ADCP. (d) Mean vertical current velocity from the L_{150} ADCP. (e) Estimated C from the L_{150} ADCP. (f) Temperature data (grey, left) from L_{150} measured at 0.3 m ASB, and (right) estimated C from the L_{150} OBS instruments at 0.35 m ASB (black) and 1.21 m ASB (blue).
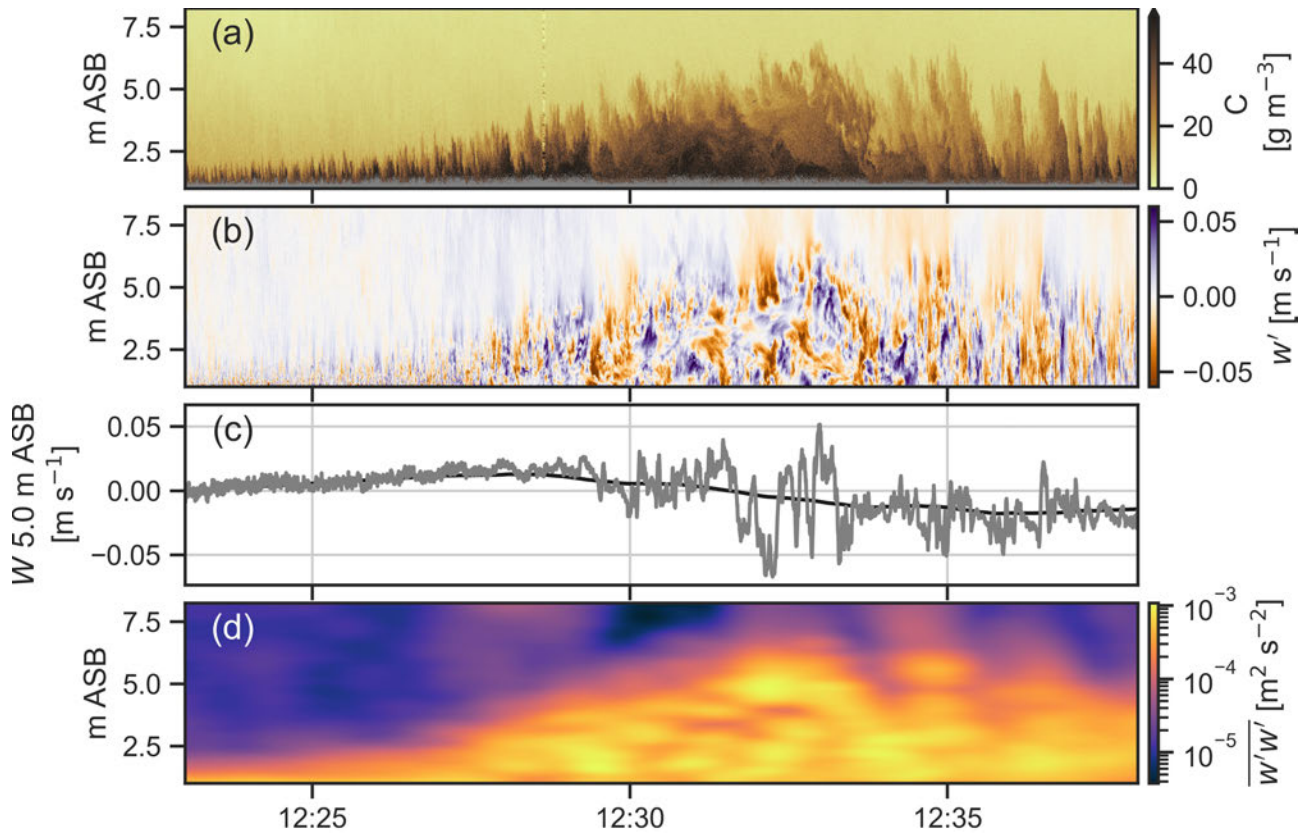
Figure 3.7: (a) Estimated C from the L_{150} ADCP. (b) Instantaneous vertical turbulent velocity after decomposition, w'. (c) As per (b), extracted at 5.0 m above the sea bed. (d) vertical turbulent kinetic energy, $\overline{w'w'}$.

with vertical advection being the dominant term. The Reynolds flux and vertical advection terms were positive, while the horizontal advection term was negative. The integrated horizontal advection term was negative over t_1 because the propagating velocity field induced by the wave set up a spatial gradient of C. The wave propagation direction was in the opposite direction to the near-bed horizontal current, so "clearer" water was advected towards the observation point.

During the t_2 period the horizontal and vertical advection terms integrated over height and time to be close to zero [Figure 3.9, orange numbers in each subplot]. Note that the vertical advection term was corrected to remove the settling flux using an estimated w_s of 1.0 mm s^{-1} (from LISST and Niskin bottle samples as per Chapter 2). The temporal integral of vertical advection during t_2 still had a non-zero profile [Figure 3.9c] suggesting it contributed to redistribution of C in the water column. Note that the sum of the three integral values [Figure 3.9b,c,d] do not add to the integral of C_t [Figure 3.9a] because the settling velocity was removed by correction of W and because small errors are cumulative over the integral.

The integrated Reynolds flux was large and positive when integrated over t_2, suggesting that turbulent mixing was the key mechanism lifting sediment over the rest of the wave train [Figure 3.9b]. This is in contrast to analyses that suggests that a global instability is the key mechanism involved in lifting sediment high into the water column after a NLIW of depression has passed [Aghsaee et al., 2012; Bogucki et al., 1997; Diamessis and Redekopp, 2006; Johnson et al., 2001; Sakai et al., 2020]. This analysis only captured the area between 2.5 and 7.5 m ASB and instabilities with time-scales shorter than the averaging period may not have been visible using this method. In addition, at high Reynolds numbers instabilities may become small and remain attached to the bed [Simoni et al., 2017] and may not be captured using this method. This wave event is in general agreement with the analysis of Zulberti et al. [2020], who did not observe any global instability. It is plausible that the successive waves in the train suppressed the growth of coherent instabilities by inducing negative vertical velocities (and accelerating horizontal currents) when the instabilities were expected to occur. This process may work in addition to the destruction of instabilities by turbulent stirring [as proposed by Zulberti et al., 2020].

3.6 Solibore

3.6.1 Wave description

The solibore that occurred at approximately 11:40 on 22 March was one of nine similar events clearly identified in the 15-day analysis period (additional sudden resuspension events also occurred that were not clearly identifiable as a solibore). near-bed currents during the event were directed onshore and upslope (Southeast) [Figure 3.10]. Wave speed and direction calculations (described previously) estimated the direction of propagation to be approximately 160° from North, 20° degrees south of the cross shelf tidal ellipse orientation. Wave speed was estimated at 0.52 m s^{-1} using backscatter correlation.

The nature of the event was consistent with the description of a solibore proposed by Henyey [1997], with upslope advection of isotherms and a train of symmetric perturbations following the initial bore [Figure 3.11]. Isotherms at the upper pycnocline were not disturbed. An initial near-bed turbid
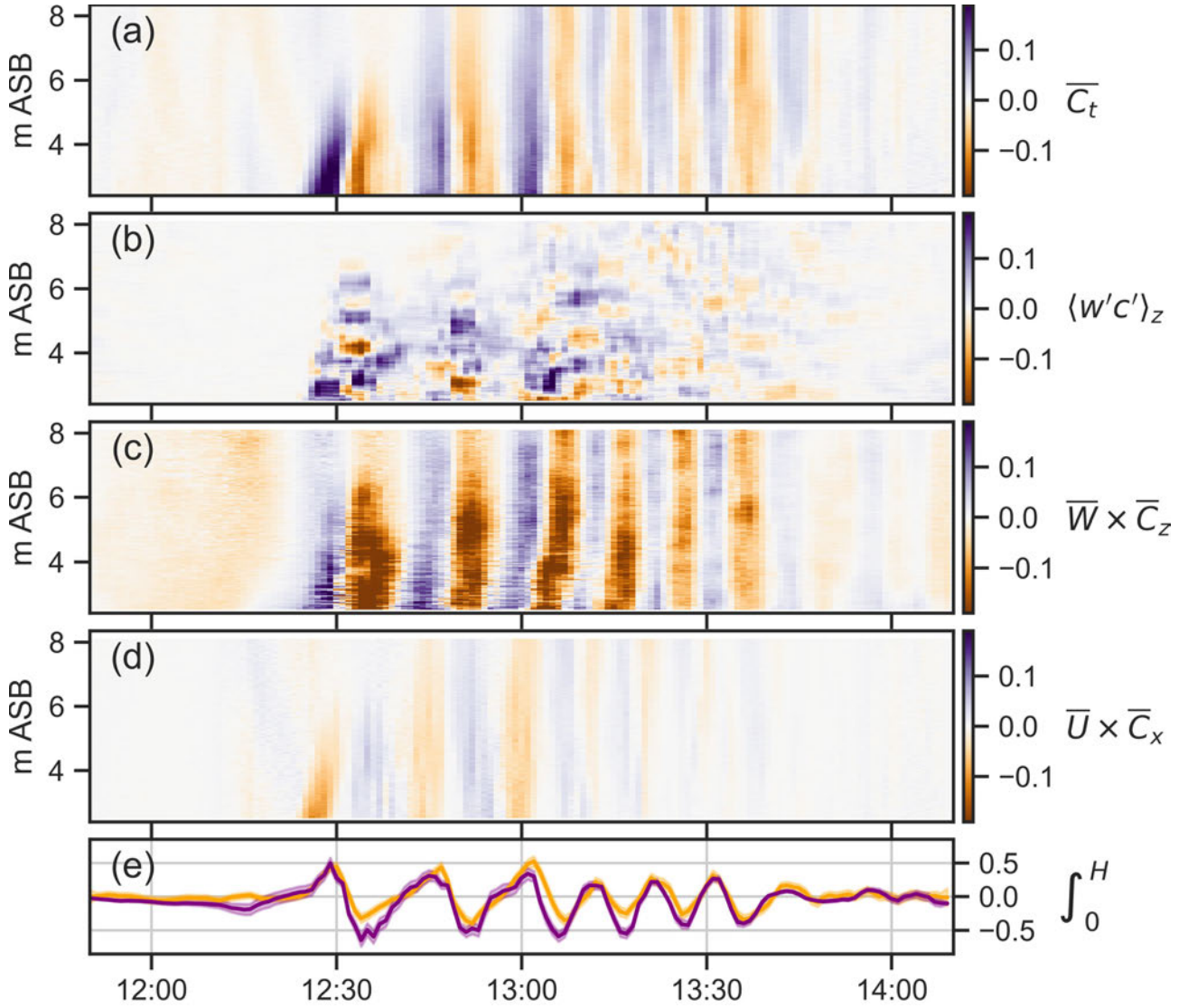
Figure 3.8: (a-d) Color plots of the four terms from Equation 3.1, as indicated by labels on the right. Colour bar limits are ± 0.19 g m^{-3} s^{-1} for all color plots. (e) The depth integrated C_t (orange) and the sum of the other terms in Equation 3.1 (purple), shown with units g m^{-2} s^{-1}. The 95% credible intervals of the vertical integral terms are shown as shading around each line in (e), but overall the uncertainty was small when integrated along this dimension.
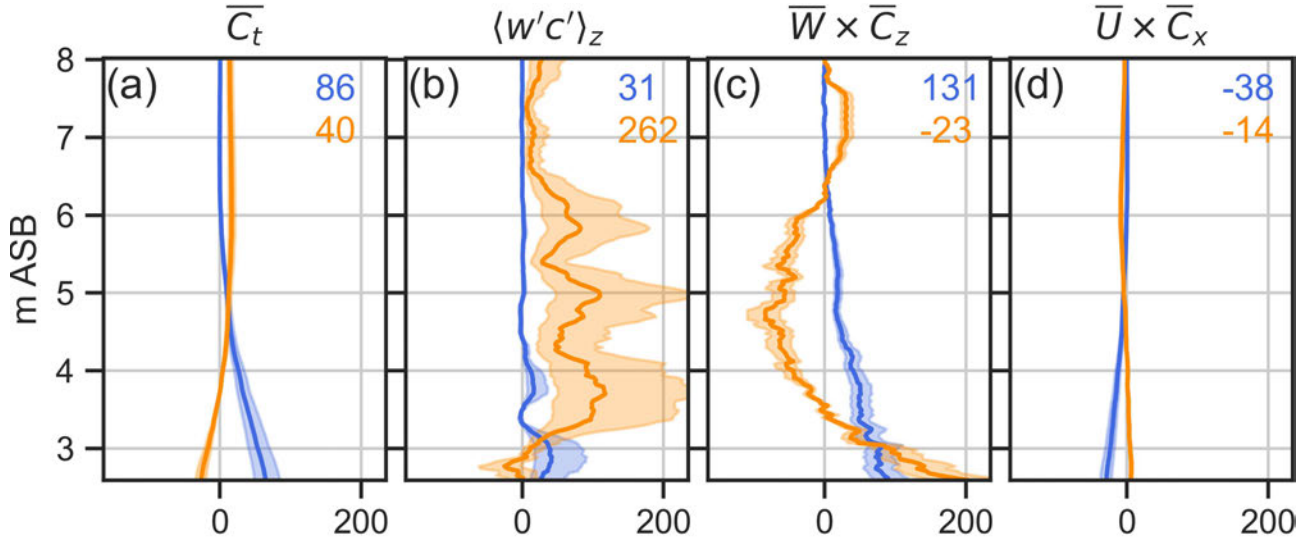
Figure 3.9: Temporal integrals of the four terms in Equation 3.1 for the period t_1 (blue) and t_2 (orange). All x-axes are in units g m^{-3}. The numbers indicate the integral of both time and height for each term (i.e., the vertical integral of the line in each subplot), with the text colour matching the line, providing a sum of the terms' contribution in units g m^{-2}.
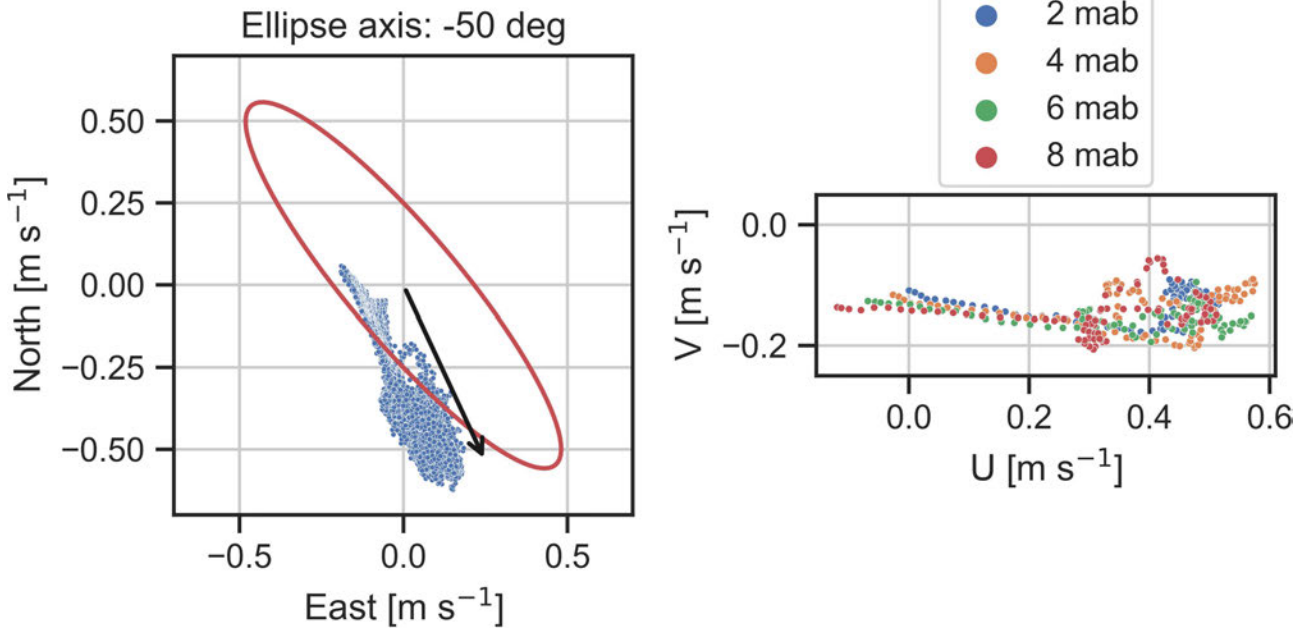

Figure 3.10: Left: Tidal ellipse (from all data) and boxcar filtered currents under the leading perturbation of the solibore. Right: Rotated mean currents at four different heights under the leading perturbation of the solibore.

wave core arrived during onshore tidal flow with a near-vertical face, followed by several more solitary wave-like features with turbid cores. After the arrival of the bore there was a prolonged period of elevated C (over the rest of the half-tidal cycle, not shown). In the 2 minute period over the initial core's arrival, the cross-shelf near-bed velocity changed direction from -0.2 to 0.6 m s^{-1}. This period was accompanied by a pulse of positive vertical velocity that exceeded 0.1 m s^{-1} within the bottom 8 m ASB. A small temperature drop of less than 0.1° C was measured at the lander, coincident with the sharp increase in C. The OBS instruments sampled too slowly to adequately capture the high frequency event.

The initial turbid wave core appeared to be tightly bound by strong positive and negative vertical velocities [Figure 3.11d,e]. Despite this close proximity of elevated C and strong W, it is not clear that these regions directly overlapped. This is similar to observations by Richards et al. [2013, Fig. 9c,e] and Masunaga et al. [2017, Fig. 10c,d], and also 3D numerical simulations by Deepwell et al. [2020, Fig. 10c,d]. In each of these cases the wave core has a high horizontal velocity and was tightly bound by strong positive vertical velocities at the front face of the core and strong negative vertical velocities at the rear face of the core. In these cases, however, it is also not clear how the advective wave core interacted with strong pulses of W, similar to our observations. Below we directly compute the vertical advection term, $\overline{W}.\overline{C}_z$, to provide insight into these observations.

The spatial structure of the initial wave core was determined using the wave speed, estimated as described previously [Figure 3.12]. The turbid core was around 70 to 80 m in width. The wave core was easily identifiable by estimating the horizontal velocity in the reference frame of the wave, i.e., U_{wave} was estimated by subtraction of c_{wave} from U [Figure 3.12b]. Small areas could be observed within the wave core where U_{wave} exceeded c_{wave}, but a coherent recirculation pattern could not be identified.

The full height of the turbid core was unknown as it extended beyond the range of the L_{150} ADCP, although OBS instruments deployed on T_{150} at 12.6 and 24.0 m ASB registered a small increase in turbidity at the time of the event (not shown). However, we can observe a vertical gradient of C within the bottom 8 m which indicates that the most turbid part of the wave core was restricted to a smaller region than the isotherm perturbation visible in the temperature contours, which move from 10 to 50 m ASB as the initial front arrives. This presence of a small highly turbid core within a larger wave may explain the short but intense periods of elevated backscatter observed by [Moum et al., 2007, Fig 5].

3.6.2 Flux estimates

For the solibore the sign of c_{wave} and $\overline{U}$ were the same, with flow in the direction of wave propagation [Figure 3.13]. The segment length for Reynolds decomposition was 30 seconds for this event, calculated on a 5 second time step. This short segment length may have resulted in imperfect partitioning of the vertical fluxes, but was necessary for the observed high frequency oscillations.

Horizontal advection dominated the event, with instantaneous magnitudes 5 to 10 times higher than the other terms [Figure 3.13]. The vertical advection and Reynolds flux are shown in more detail in Appendix B (together with the data and decomposition). Vertical advection within the wave core was generally small and negative. Vertical advection in the lee of the wave core was negative, due to the confluence of negative vertical velocities and elevated C. The strong jet of positive vertical velocity preceding the core occurred when C was low, thus producing relatively small positive vertical transport
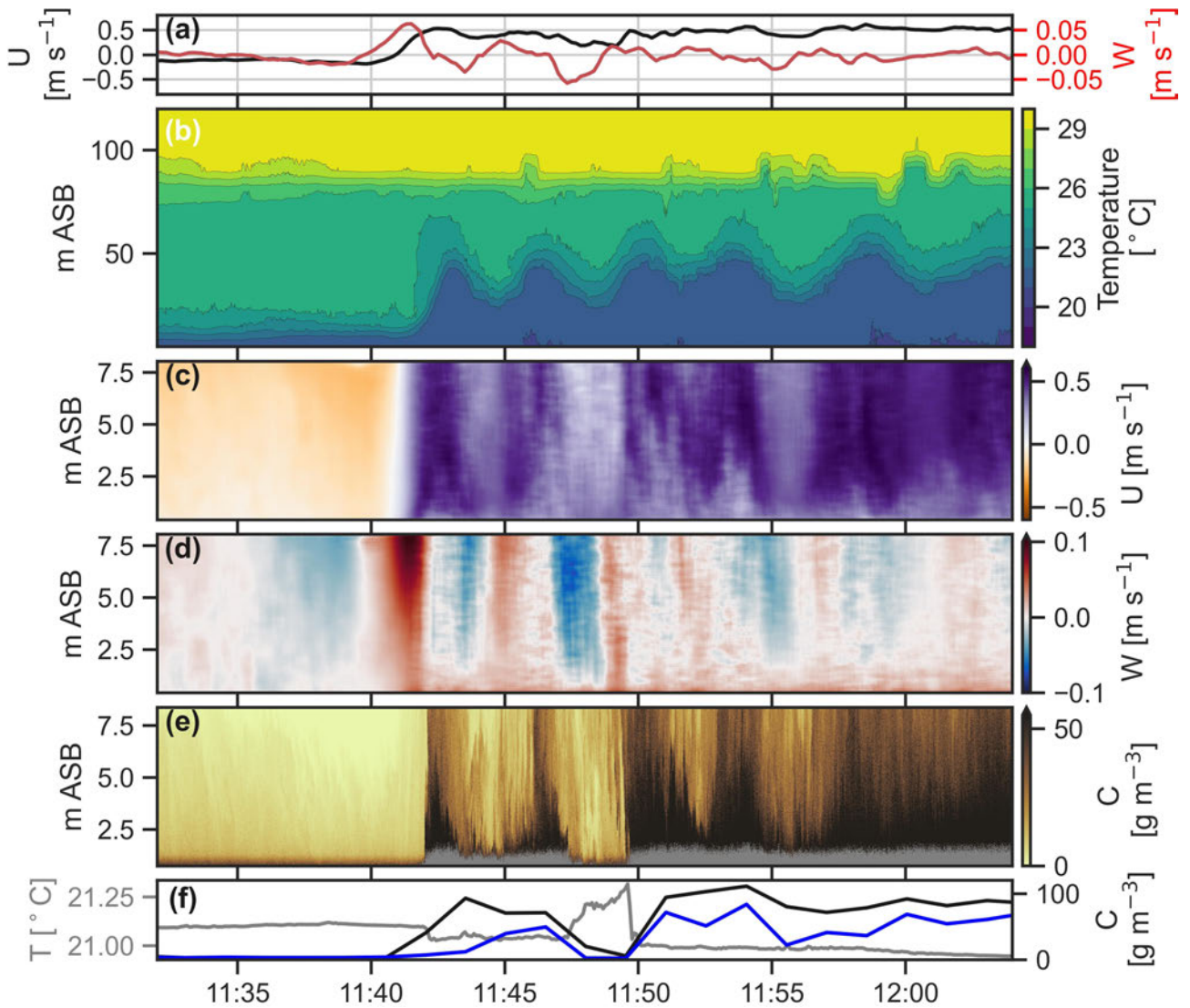
Figure 3.11: (a) Cross-shelf (left, black) and vertical (right, red) mean current velocity at 4.0 m
ASB (boxcar-filtered with a 30 second window, shown on a 4 Hz time step). (b) Temperature contours
from the through-water-column mooring T_{150}. (c) Mean cross-shelf current velocity from the L_{150}
ADCP. (d) Mean vertical current velocity from the L_{150} ADCP. (e) Estimated suspended sediment
concentration from the L_{150} ADCP. (f) Temperature data (grey, left) from L_{150} measured at 0.3 m
ASB, and (right) estimated suspended sediment concentration from the L_{150} OBS instruments at 0.35
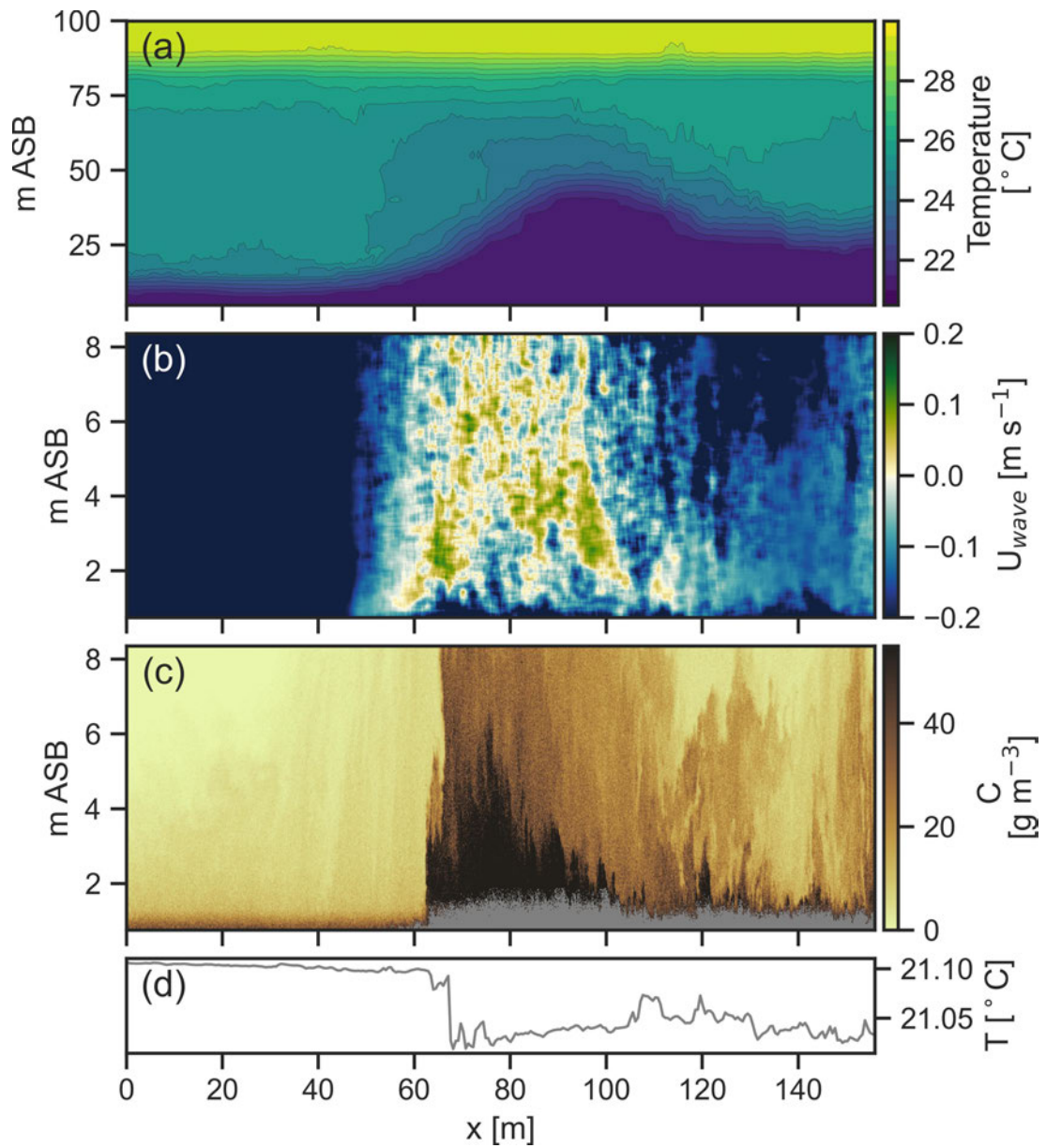m ASB (black) and 1.21 m ASB (blue).

Figure 3.12: Observations of the solibore during the initial wave perturbation. (a) Temperature contours as measured at T_{150} (note there may be some delay between moorings). (b) Horizontal velocity in the reference frame of the wave ($U_{wave} = U - c_{wave}$) as measured by the L_{150} ADCP, smoothed for visual clarity. (c) Estimated C from the L_{150} ADCP. (d) Temperature measured at L_{150} (grey).